NASA CR-134782
Creare TN-204

AERODYNAMIC AND MECHANICAL DESIGN OF AN 8:1 PRESSURE RATIO CENTRIFUGAL COMPRESSOR

by Colin Osborne, P. W. Runstadler, Jr., and
W. Dodd Stacy

CREARE INCORPORATED

prepared for

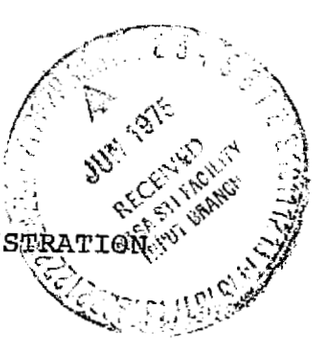

NATIONAL AERONAUTICS AND SPACE ADMINISTRATION

NASA Lewis Research Center

Contract NAS 3-17848

1. Report No.	2. Government Accession No.	3. Recipient's Catalog No.
NASA CR-134782		

4. Title and Subtitle	5. Report Date
AERODYNAMIC AND MECHANICAL DESIGN OF AN 8:1 PRESSURE RATIO CENTRIFUGAL COMPRESSOR	April 1975
	6. Performing Organization Code

7. Author(s)	8. Performing Organization Report No.
Colin Osborne Peter W. Runstadler, Jr., and W. Dodd Stacy	TN-204
	10. Work Unit No.

9. Performing Organization Name and Address	11. Contract or Grant No.
Creare Incorporated P. O. Box 71 Hanover, N. H. 03755	NAS3-17848
	13. Type of Report and Period Covered

12. Sponsoring Agency Name and Address	13. Type of Report and Period Covered
National Aeronautics and Space Administration Washington, D. C.	Contractor Report
	14. Sponsoring Agency Code

15. Supplementary Notes

Project Manager, Jerry R. Wood, Lewis Research Center and
U. S. Army Air Mobility R & D Laboratory, Cleveland, Ohio

16. Abstract

An 8:1 pressure ratio, 0.907 kg/s (2.0 lbm/s) centrifugal compressor stage has been designed and fabricated. The design proceeded subject to the specifications that (i) the stage be representative of "state-of-the-art" performance (efficiency and flow range) and (ii) the stage will be used as a "workhorse" compressor for experiments to be conducted using laser Doppler velocimeter (LDV) equipment. The final design is a 75,000 RPM, 19 blade (no splitters) impeller with an axial inducer and 30° of backward leaning at the impeller tip. An optimally matched, 17 channel, vane island diffuser was designed and built. The calculated total-to-static efficiency is 77% with a flow range of 12%, choke-to-surge, at design speed.

All of the compressor hardware has been fabricated and inspected and the stage has been checked out for mechanical integrity at design speed under a companion program.

17. Key Words (Suggested by Author(s))	18. Distribution Statement
Centrifugal Compressor High pressure ratio compressor	Unclassified - unlimited

19. Security Classif. (of this report)	20. Security Classif. (of this page)	21. No. of Pages	22. Price*
Unclassified	Unclassified	146	$3.00

* For sale by the National Technical Information Service, Springfield, Virginia 22151

TABLE OF CONTENTS

TABLE OF CONTENTS - Continued

LIST OF TABLES

LIST OF FIGURES

LIST OF FIGURES - Continued

LIST OF FIGURES - Concluded

SUMMARY

The aerodynamic and mechanical design of a high pressure ratio (pr = 8), low mass flow (m = 0.907 kg/s), centrifugal compressor, typical of designs that might be used for small aircraft and gas turbine engines, has been undertaken. The design was subject to the requirements that (i) the compressor be of "state-of-the-art" performance with respect to efficiency and range, (ii) the inducer tip operate at a relative Mach number of 1.2, and (iii) the compressor unit be used as a "workhorse" compressor together with laser Dopper velocimeter (LDV) equipment.

A Preliminary Design (one-dimensional analysis) study examined the trade-offs, for both radial and backward leaning impellers, with regard to aerodynamic performance, rotative speed and geometrical dimensions that are best suited for use with the LDV equipment and subject to the above constraints. State-of-the-art performance dictated designs with backward leaning impellers The preliminary design established (i) the rotational speed set by the 1.2 inducer tip relative Mach number requirement and (ii) designs with no splitters so as to generate large flow path dimensions relative to the LDV measurement resolution volume.

The final stage configuration designed and fabricated is a 75,000 RPM, 19 blade impeller with an axial inducer and 30° of backward leaning at the tip. The diffuser is a 17 vane, radial divergence, channel diffuser. This configuration was calculated to have a 77% total-to-static efficiency at the design point with 12% flow range from choke-to-surge (range is defined as $(1-\dot{m}_{surge}/\dot{m}_{choke}) \times 100$).

Two and/or quasi-three-dimensional aerodynamic and stress calculations were performed for the above design. Critical speed analyses were performed for the high speed rotating impeller assembly.

The inducer was designed by a method of transference from axial compressor technology. The remainder of the impeller was designed by using quasi-three-dimensional, potential flow techniques iterated with boundary layer calculations to control the blade loading distributions throughout the impeller. The channel diffuser inlet and vane-suction surface were designed using a two-dimensional, potential flow/boundary layer calculation procedure.

A complete mechanical design of the compressor configuration was undertaken since the compressor unit is to be tested on a low-speed-of-sound (LSM) compressor test facility. Stress and vibration calculations were performed for the titanium impeller. Adequate burst speed was calculated and no problems associated with the blade vibration studies were found. However, the finite element disc stress calculations indicate that the bore of the impeller will yield locally and stress relieve at 120% air design speed (90,000 RPM).

Apart from the LDV equipment, the compressor has been heavily instrumented to obtain the aerodynamic data necessary for the analysis of the stage component performance. This includes the measurement of total pressures in the diffuser and time-averaged and dynamic (unsteady) pressure measurements in the inlet, on the impeller cover and throughout the vaned, radial diffuser.

The stage design has been tested for mechanical integrity and confirmation of critical speeds up to design speed on a companion program.

INTRODUCTION

This report describes the design and fabrication of a small mass flow, high pressure ratio centrifugal compressor stage specifically configured to be used with an advanced laser Doppler velocimeter system developed under a companion program (NASA/USAAMRDL Contract NAS3-17860). The design of the stage has attempted to be representative of the "state-of-the-art" technology and performance of the high performance centrifugal used in gas turbine engines for helicopter and light aircraft use and off-the-road land vehicle applications. At the same time, the design has had to meet the practical constraints imposed by the use of this hardware with the laser Doppler velocimeter (LDV) instrument and other diagnostic tools. The ultimate purpose of the stage developed on this program is its use as a "workhorse" tool for the study of the basic fluid dynamics of the inducer, impeller and diffuser components of the high pressure ratio, centrifugal compressor.

This work is a continuation of the development of centrifugal compressors by U. S. government agency sponsored efforts over many years. These development efforts date back to the early work by the NACA which was continued in the late 1960's by the U. S. AAMRDL (formerly U. S. Army AVLABS) who sparked a surge of centrifugal compressor development for advanced helicopter engines. Higher efficiency and greater stability to flow distortions and gas turbine engine transients are the primary objectives today for continued research and development work on the high pressure ratio centrifugal. Future studies using the stage hardware designed and developed on this program, in combination with LDV equipment, will permit the analysis and improved understanding believed to be essential to the development of design tools required to achieve the ultimate performance for which the centrifugal is believed capable.

The following sections of this report describe the aerodynamic and mechanical design work performed in developing this "workhorse" centrifugal stage.

DESIGN OBJECTIVES AND SPECIFICATIONS

The overall objective of this centrifugal compressor development and fabrication program has been to provide a state-of-the-art performance (re to efficiency and range), high pressure ratio, small mass flow centrifugal compressor stage typical of designs that might be used for small aircraft and helicopter gas turbine engines.

This stage will be a "workhorse" compressor to be used, together with advanced aerodynamic instrumentation including, in particular, laser Doppler velocimeter (LDV) equipment, on future programs to unravel the complicated fluid dynamics within the compressor. The design work examined the tradeoffs with regard to aerodynamic performance, rotative speed and geometrical dimensions that are best suited for hardware to be used for these aerodynamic research purposes. These aerodynamic and physical specifications and design constraints are described below.

Aerodynamic Specifications

The aerodynamic specifications for a single stage compressor (inlet, impeller and matching diffuser and collector) have been set down by the contract as follows:

fluid	= air
inlet ambient temperature	= 288.2°K (518.7°R)
inlet ambient pressure	= 1.014×10^5 Newton/meter^2 (14.7 psia)
total pressure ratio	= 8
air mass flow	= 0.907 kg/s (2.0 lb_m/s)
inlet relative Mach number at inducer tip	= 1.2
no inlet guide vanes	= 0° prewhirl
vane island diffuser	

Both radial bladed and backswept bladed impellers were considered during the preliminary design work.

A vane island diffuser was to be optimized with the impeller design for efficiency and range performance.

Other Design Constraints

The ultimate use of the hardware as a "workhorse" compressor for aerodynamic studies guided the course of

the design. Thus the choices for the final proposed design considered the factors of rotational speed and and the physical dimensions of the flow passages as they impact the use of LDV instrumentation. A low rotational speed is desired in order to allow a sufficient time period for velocity measurements to be made at a point in the flow compared to the time for relative motion of the rotating impeller blade passages.* Large dimensions of the flow path are advantageous to permit better resolution of velocities at a point in the flow for a given size of the LDV measurement resolution volume.

The design work included the detailed mechanical design of the impeller, vane island diffuser, shroud, shaft and other parts required. The mechanical design effort included the following requirements:

1. The impeller should be designed with an overspeed margin of 120% of air design speed, to be verified by stress analysis.

2. The compressor stage mechanical design will have no critical speeds between 40% and 120% of equivalent design speed when tested in Creare's Low Speed of Sound Modeling facility.

---

*This will be primarily achieved in the LDV testing by using LSM testing which permits a rotational speed of about 0.65 to 0.70 of that required in air testing.

PRELIMINARY AERODYNAMIC DESIGN

The intent of the preliminary design was to set the overall geometric quantities and performance levels for each component of the compressor subject to the geometric and other constraints. Both radial and backward leaning impellers were analyzed using the standard Creare design methodology. Calculations were made using the English system of units.

Design Procedures

The standard Creare aerodynamic design methodology was employed in the investigations of the radial and backswept bladed preliminary designs. This design methodology is described in detail in Reference 1. Additional comments pertaining to specific aspects of the preliminary design analysis are discussed below.

Inlet analysis - An inlet flow analysis and inducer optimization study was made to define rotational speed and inducer hub to tip radio. This design was conducted under the following conditions: (All symbols are defined in Appendix A.)

α_{it} = 0 (no prewhirl, no IGV's)

p_{oo} = 1.014×10^{5} Newton/meter^2 (14.7 psia)

T_{oo} = 288.2°K (518.7°R)

m = 9.072×10^{-1} kg/s (2.0 lbm/s)

$M_{rel\ lt}$ = 1.2

The following additional specifications were used in carrying out the inducer study (these were not specified under the contract):

1) Mass flow is distributed to produce a uniform axial velocity profile with radius at the inducer inlet (unblocked flow).

2) At design speed, approximately 15% margin in mass flow between choke and surge is desired (i.e., 7.711×10^{-1} kg/s is the maximum desired surge flow rate).

3) Blade tip stagger angles of less than 60° are desirable at the inducer lead edge. Stagger angles larger than 60° make inducer designs at high relative tip Mach numbers difficult because of excessive blade blockage leading to local flow acceleration.

4) Inducer hub-to-tip ratios $0.3 \leq (r_h/r_t)_1 \leq 0.5$ were considered. For each speed N and inducer hub-to-tip ratio $(r_h/r_t)_1$ combination, the inducer inlet analysis was used over a range of axial inlet velocity C_{x1} to determine inducer tip relative Mach number $M_{rel\ 1t}$ and inducer tip lead edge relative flow angle, β_{1t}.

A general functional relation $N = f(Z_o, \beta_{1t})$ exists for the given inlet conditions described above. Figure 1 displays the relation $Z_o = (r_h/r_t)_1$ = inducer hub-to-tip ratio versus rotational speed N for constant inlet flow angle $\beta_{1t} = -65.2°$ and $-60.3°$ (for $M_{rel\ 1t} = 1.2$). Figures 2 and 3 display the values of C_{x1} corresponding to to the Z_o and N range of Figure 1.

It is clear from Figures 2 and 3 that there are in general two solutions (C_{x1} values) for which $M_{rel\ 1t} = 1.2$. For example, at N = 75,000 RPM and $Z_o = 0.5$ these correspond to 167.6 and 195.7 m/s. The high value of C_{x1} corresponds to a low value of β_{1t}. The variation of β_{1t} at design flow with inlet axial velocity C_{x1} is shown in Figure 4 for $Z_o = 0.5$ and in Figure 5 for $Z_o = 0.3$.

A second criterion was to maintain a small change in flow incidence with mass flow so as to maintain adequate inducer stall margin. The change in flow incidence Δi_m with axial velocity C_{x1} at constant inlet relative Mach number = 1.2 is shown in Figure 6 for $Z_o = 0.5$ and in Figure 7 for $Z_o = 0.3$.

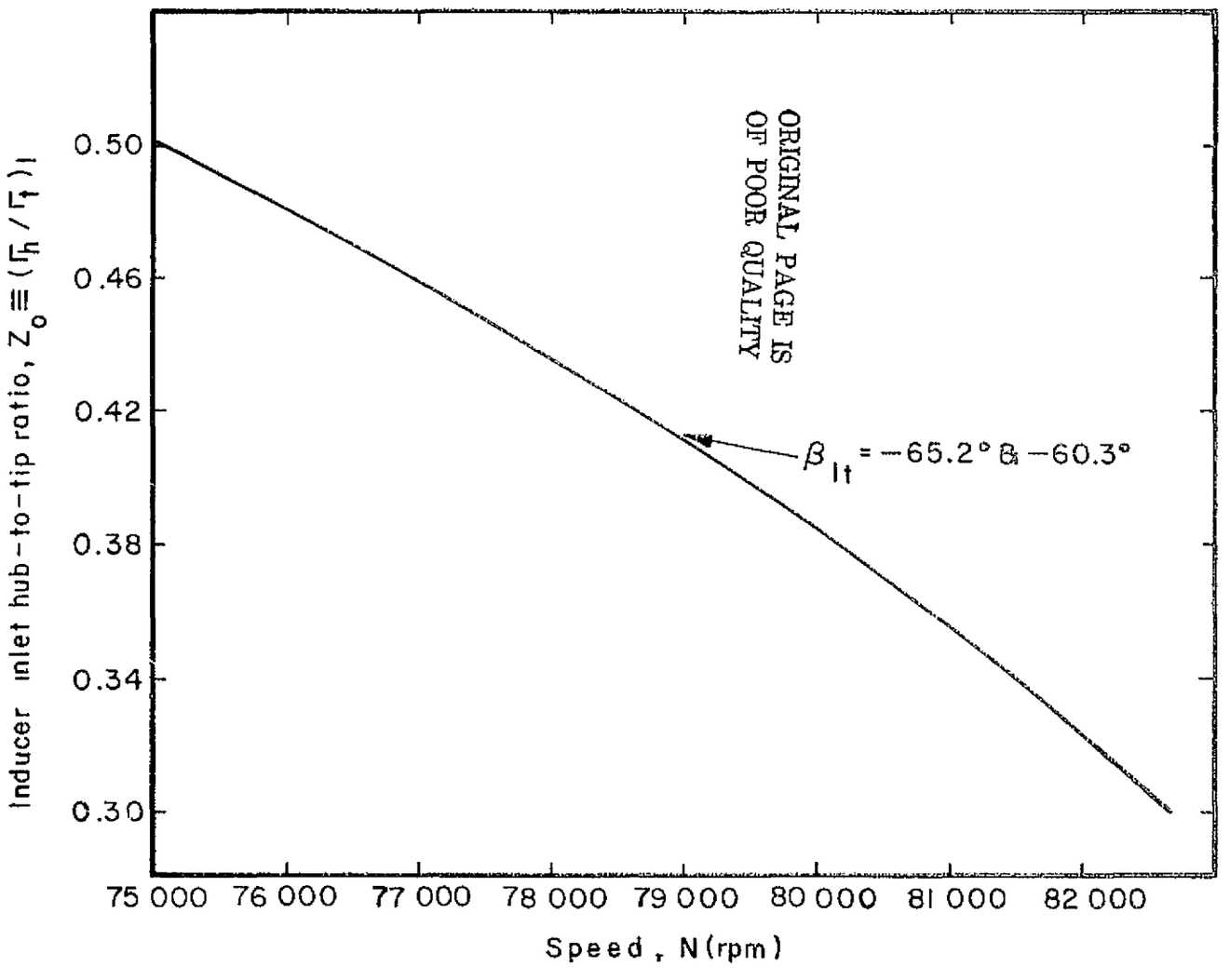

Figure 1 — Locus of Inducer Hub-to-Tip Ratio with Speed — $M_{rel\,1t} = 1.2$

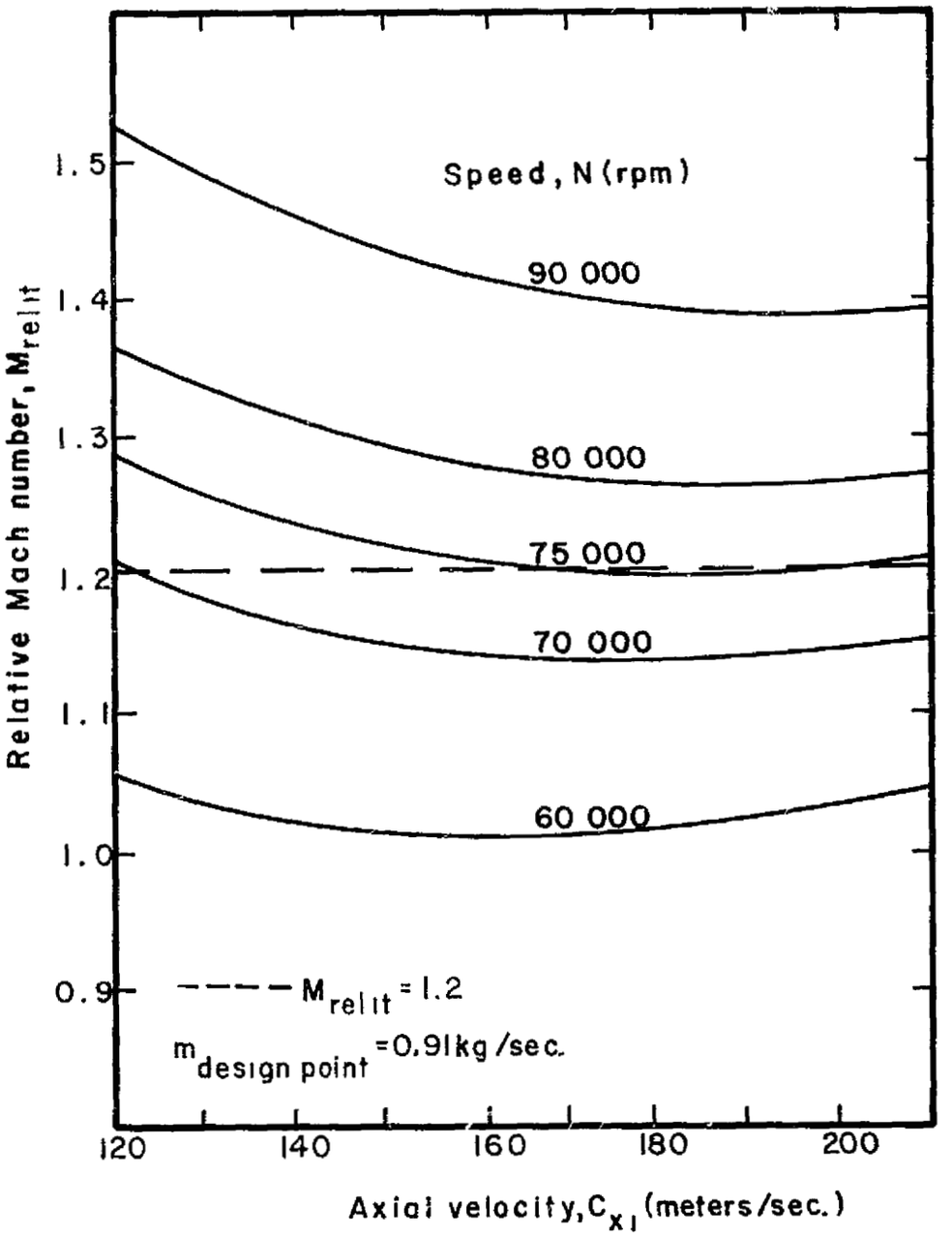

Figure 2 — Inducer Tip Relative Mach Number Variation with Axial Velocity — $Z_0 = 0.5$

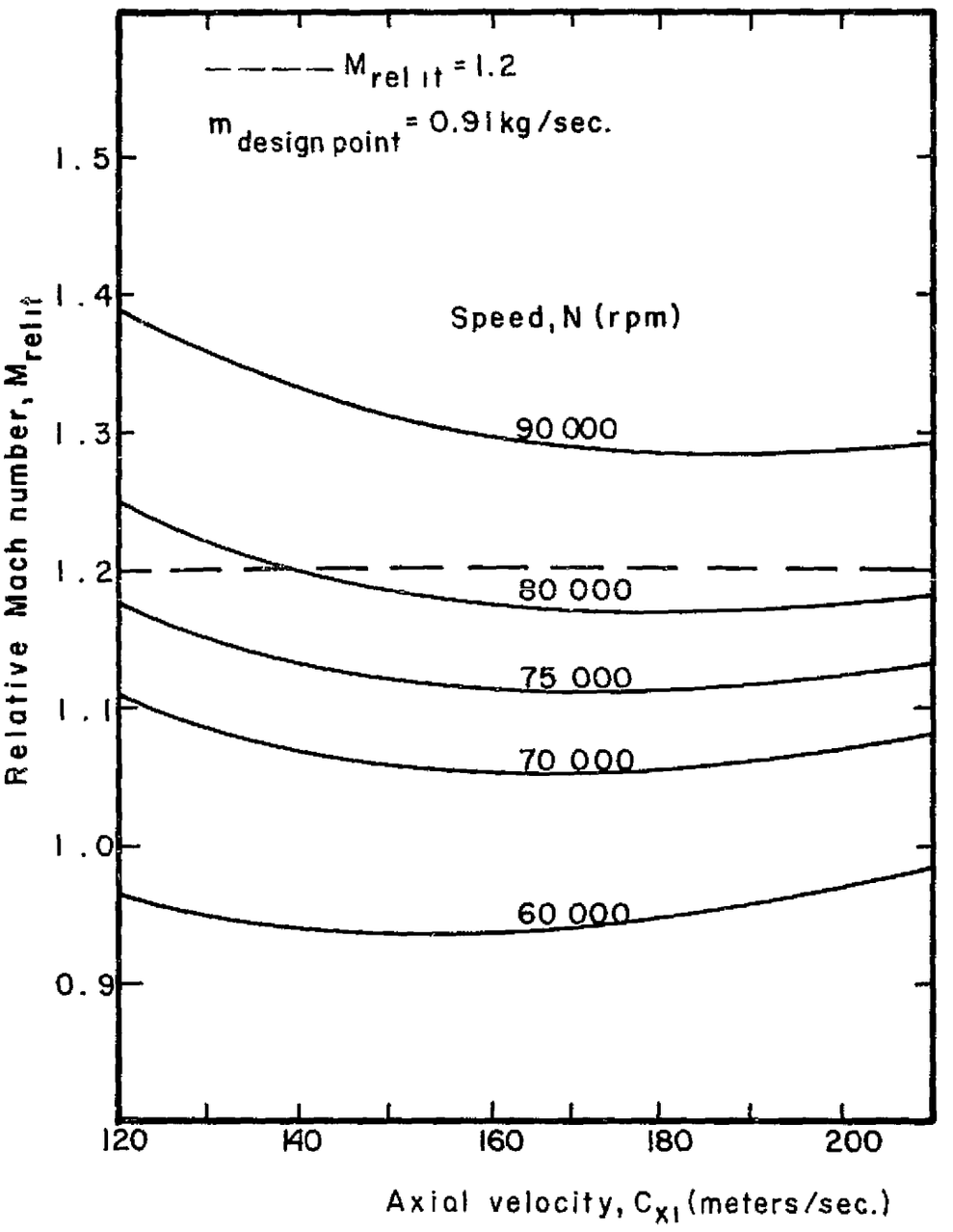

Figure 3 – Inducer Tip Relative Mach Number Variation with Axial Velocity – $Z_0 = 0.3$

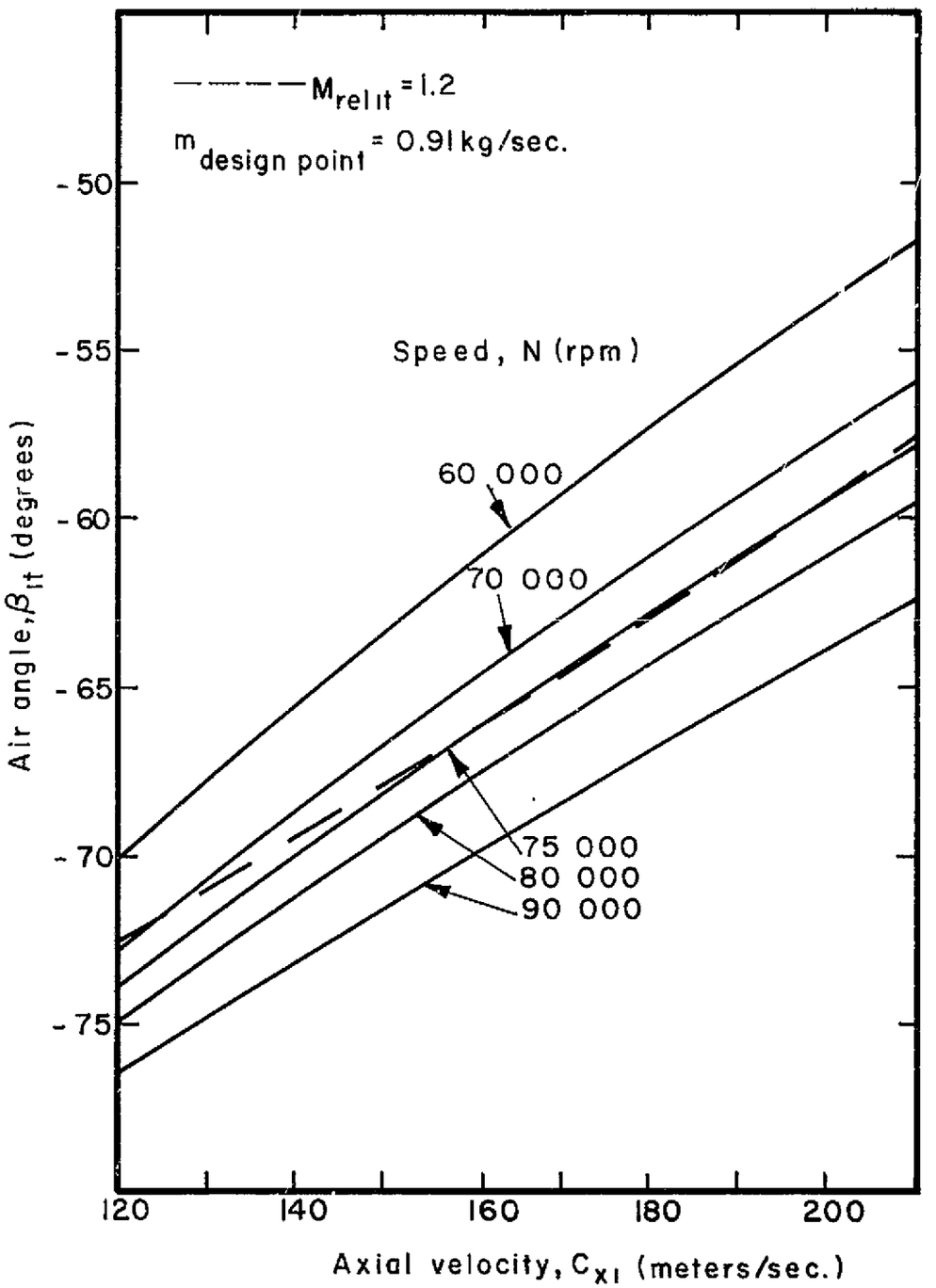

Figure 4 — Inducer Tip Relative Air Angle Variation with Axial Velocity — $Z_o = 0.5$

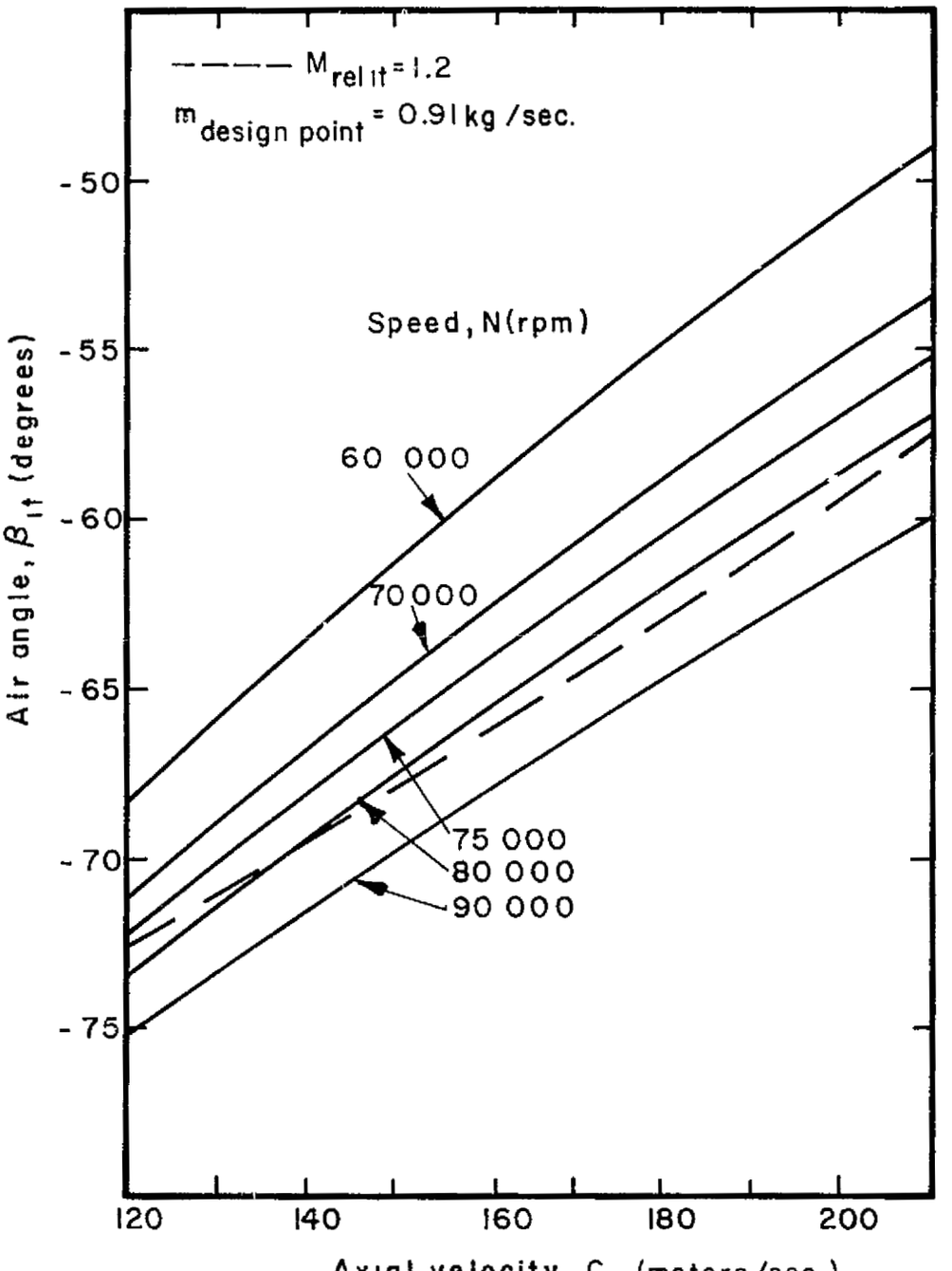

Figure 5 – Inducer Tip Relative Air Angle Variation with Axial Velocity — $Z_0 = 0.3$

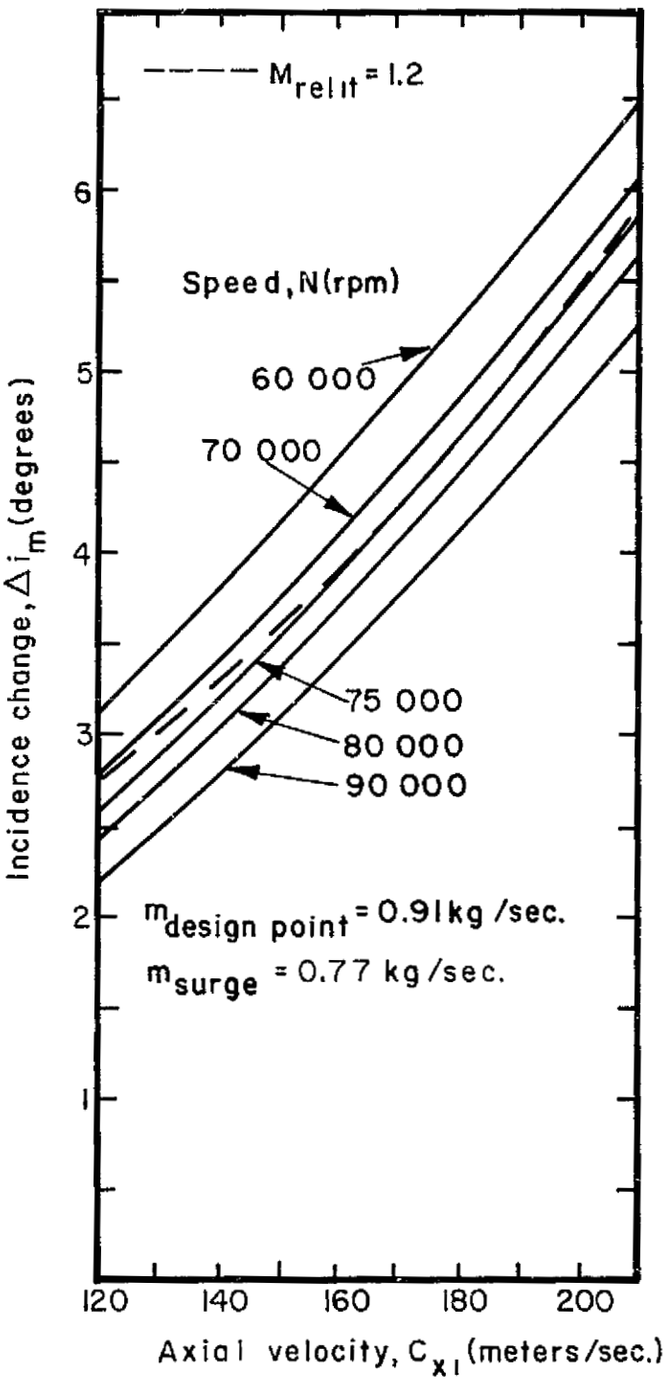

Figure 6 — Change in Inducer Tip Incidence Between Design Point and Surge – $Z_0 = 0.5$

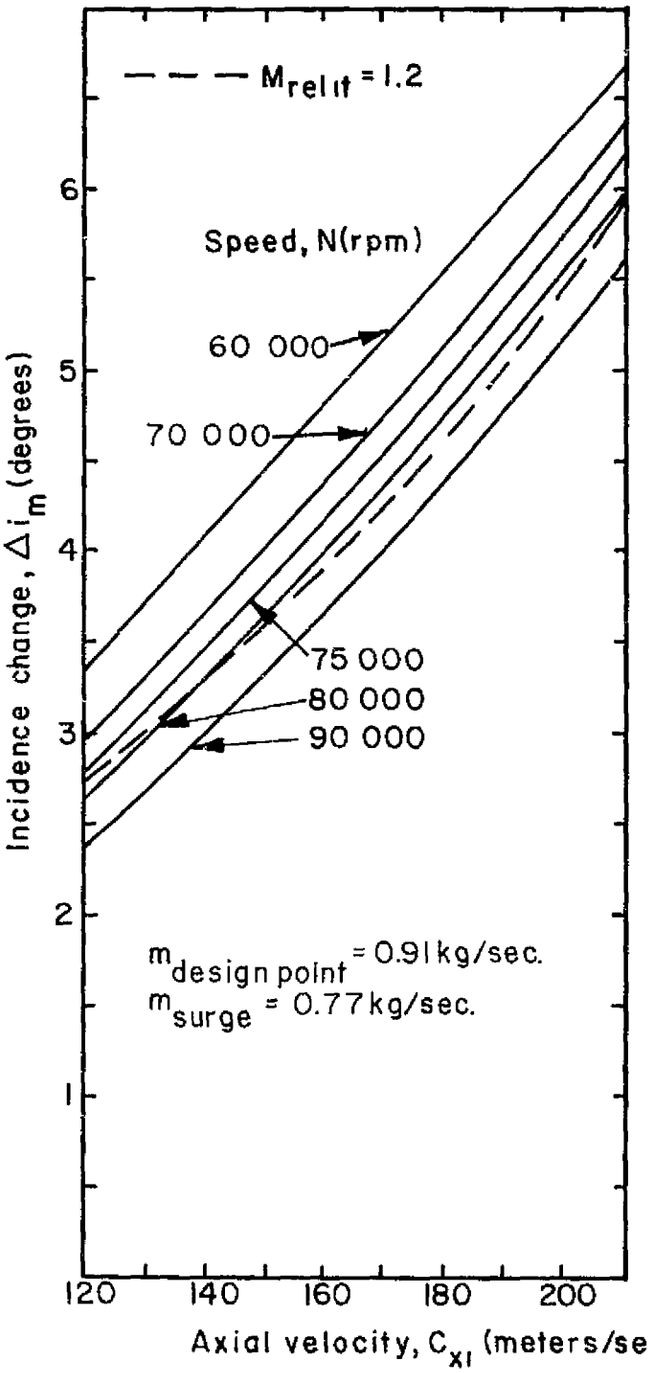

Figure 7 – Change in Inducer Tip Incidence Between Design Point and Surge – $Z_o = 0.3$

A design axial velocity of 195.7 m/s was selected corresponding to an inducer inlet relative flow angle $\beta_{1t} = -60.3°$. This selection results in a change in inlet relative flow angle of 5.25° between 9.07×10^{-1} and 7.711×10^{-1} kg/s (15% flow margin choke to surge). A rotational speed of 75,000 RPM at a hub-to-tip ratio $(r_h/r_t)_1 = 0.5$ was selected to match this relative air inlet angle.

Inducer analysis - Inducer performance has been calculated using the inducer performance map displayed in Figure 8. This map has been prepared using measured transonic axial compressor rotor performance as shown in Figure 9 (References 2, 3 and 4).

The incidence range, choke to stall, at $M_{rel\ 1t}$ values > 1.0 has been set higher than measured for the progenitor axial compressor rotor. Performance measurements on the axial fan stage indicated that at 90% of design speed and above stator performance controlled stage stall. On the basis of this evidence, it was judged that the axial fan rotor is capable of maintaining higher values of unstalled incidence up to $M_{rel\ 1t} = 1.2$ than are displayed in Figure 9. This assumption has been made in preparing Figure 8.

Figure 8 displays the important inducer variables, inducer tip diffusion ratio DR as a function of inducer tip relative Mach number $M_{rel\ 1t}$ and inducer tip mean incidence angle i_m. To design for a change in incidence angle of $\Delta i_m = 5.25°$ between design point flow and surge flow, the mean incidence i_m on the inducer map of Figure 8 has been set at 4°. This provides an inducer tip diffusion ratio of 1.425 at the design match point conditions.

Impeller design - The Creare design methodology utilizes the separated flow model in the impeller and incorporates the sudden expansion mixing model in the vaneless diffuser space at the exit of the impeller.

The inducer map and inlet flow analysis described above determine the value of diffusion ratio and hence

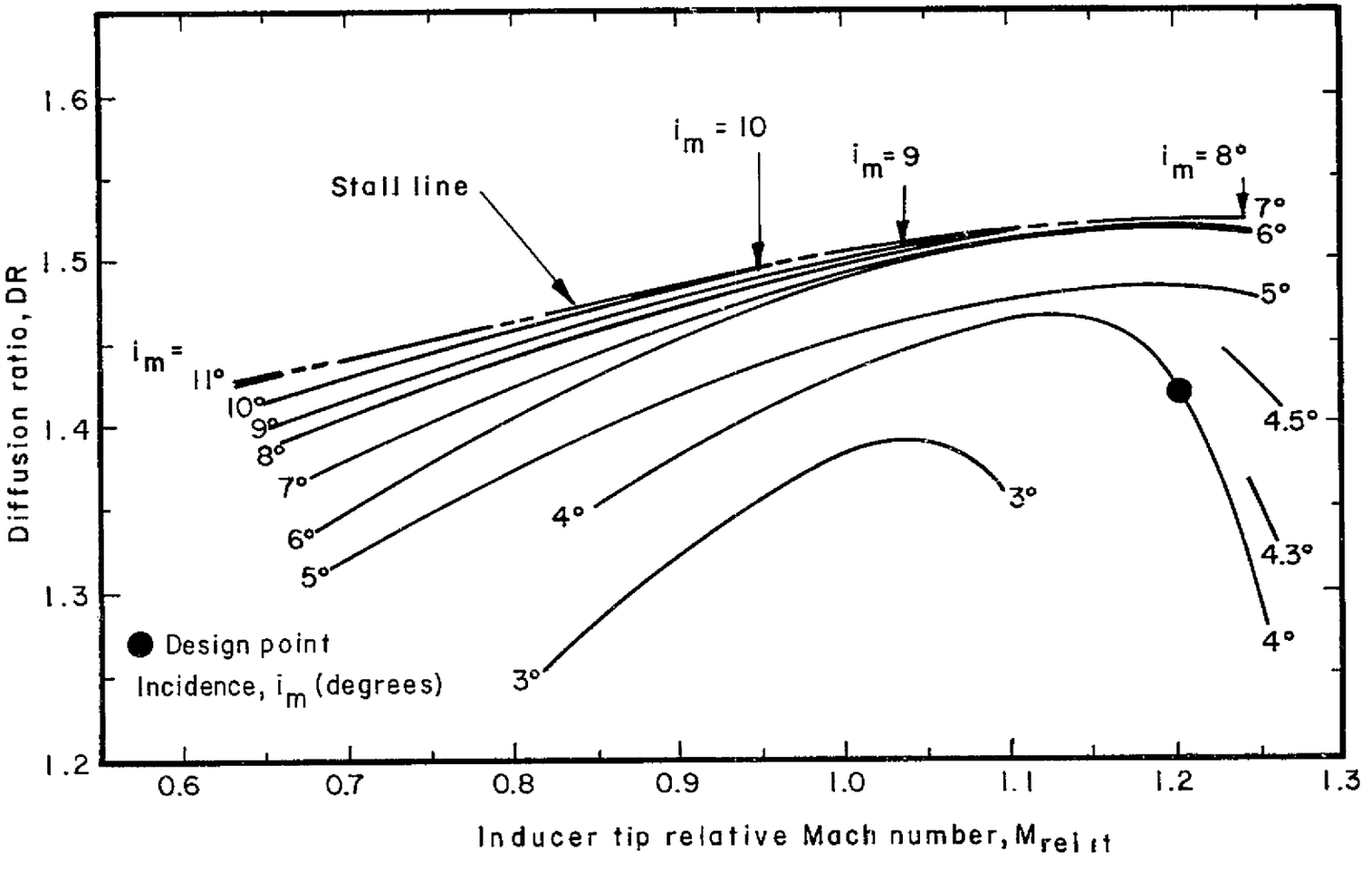

Figure 8 — Inducer Performance Map (IM-70)

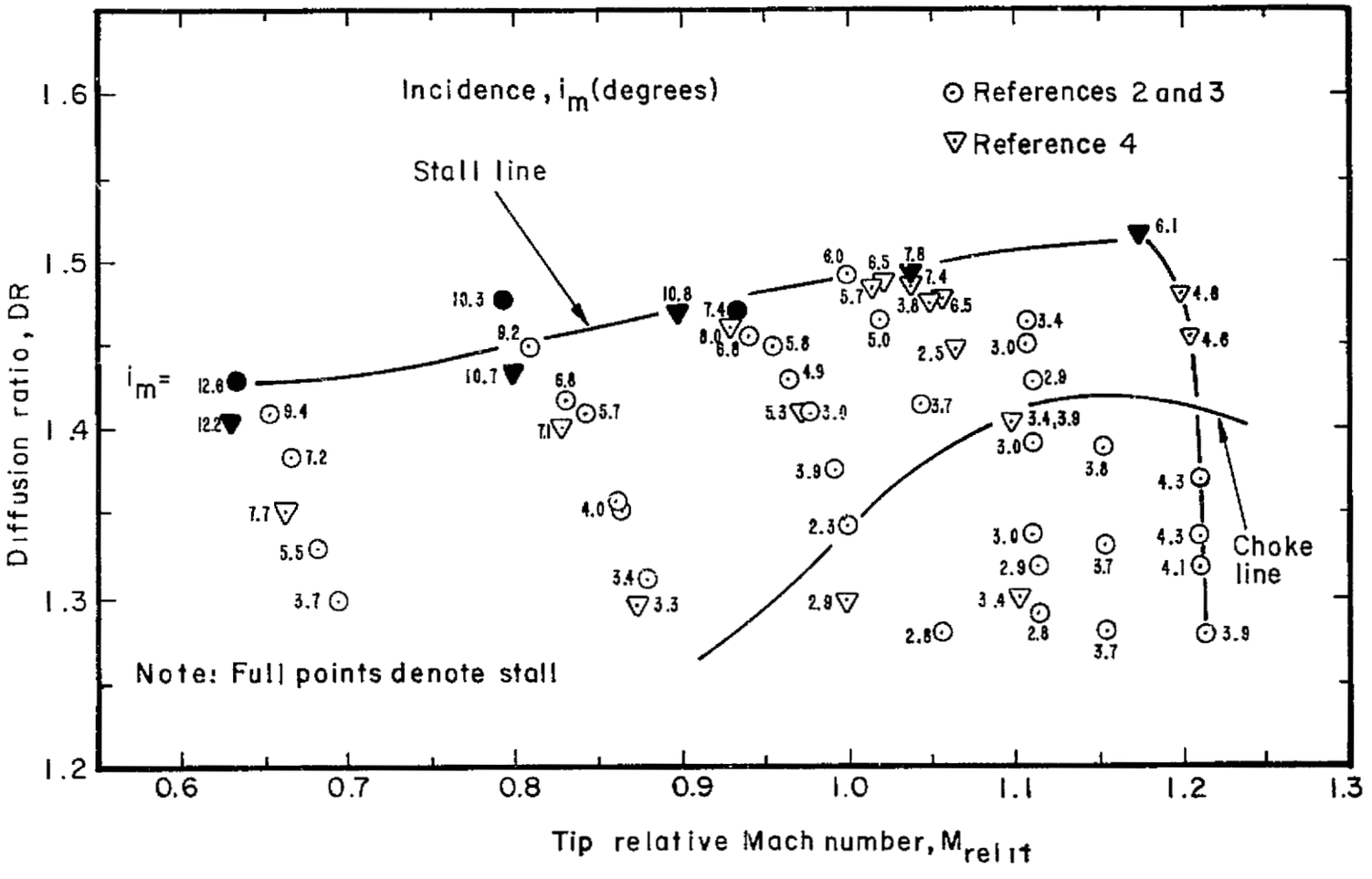

Figure 9 — Axial Fan Rotor Performance Map — P & W 305 Meters/Sec. (1000 fps) Fan

impeller tip jet relative Mach number and relative velocity. Several other parameters must be selected for the preliminary design analysis.

The mass flow fraction in the wake m_w/m has been set at 0.2 for all cases analyzed. Experimental measurements (e.g., Reference 5) have verified, at least for radial bladed impellers, that the mass flow fraction in the wake can be expected to vary between 0.15 and 0.25.

The swirl parameter λ_{2*} (= tangent of the swirl angle measured to radial at impeller exit) has been set at 2.75. It is believed that for high pressure ratio centrifugal stages, this is close to the optimum value.

Backflow from the diffuser vaneless space into the impeller is often a serious design ill for high pressure ratio compressors. Unfortunately little is known definitively about this phenomena.

Our present analytical capabilities are insufficient to quantify the expected magnitude of this loss as a function of compressor design variables (λ_{2*}, number of diffuser channels, etc.). Throughout the preliminary design task a constant backflow loss of three points in stage efficiency has been assumed. This may be treated as "insurance" on efficiency prediction since recent experience with impellers and diffusers designed by Creare methods indicates zero backflow loss. We are thus hopeful that up to three points gain in efficiency above the predictions herein might be achieved. However, we are reluctant to credit this margin at this time and prefer to treat it as reserve and hedge against uncertainties in the design predictions.

Channel diffuser design - Clearly defined single plane divergence diffuser performance maps are available only for channel diffuser aspect ratios of 0.25, 1.0, and 5.0 (References 6 and 7). To decide what the optimum geometry is for a diffuser aspect ratio not equal to those for which performance maps are available, some interpolation scheme is needed. Such a scheme has been used in this preliminary analysis and is described below.

The diffuser throat aspect ratio ($AS_4 = b_4/W_4$) has been set by requiring $b_4 = b_2$. The resulting aspect ratio for all designs studied lies between 0.25 and 1.0. Since there are no geometrical limitations on the value of the diffuser exit radius, radial plane (rather than meridional plane) diffusion has been employed for the channel diffusers. At the high match point blockages encountered in this design, there is a distinct possibility of achieving better channel diffuser recovery with radial plane diffusion rather than meridional plane diffusion. The reason stems from the fact that diffuser recovery falls off faster for throat aspect ratios greater than 1.0 than for throat aspect ratios less than 1.0 at high blockages. The situation is reversed for low blockages.

Channel diffuser recovery $C_{p\ 4\text{-}c}$ charts are needed for aspect ratios between 0.25 and 1.0. These were created for $AS_4 = 0.25$ and 1.0 for a fixed diffuser geometry of $2\theta = 10°$ and $L/W = 17$. This geometry has been chosen as a compromise made between (i) providing a sufficient buffer region between this geometry and the steep fall off in $C_{p\ 4\text{-}c}$ that occurs at high values of 2θ and (ii) on the other hand not providing too large a buffer region and unnecessarily penalizing channel diffuser recovery and, therefore, stage performance.

The number of diffuser channels has been set at 17 to achieve adequate flow area at the channel diffuser throat yet maintain $AS_4 > 0.25$ for radial plane divergence.

Blade stress calculations - There are several uncertainties in the stress analysis of blading for centrifugal compressors. Blading stresses arise from at least four different sources:

1) centrifugal loads,
2) vibration,
3) displacement of boundaries, i.e., distortions at the blade attachment point to the disc due to combined thermal and centrifugal stresses in the disc, and
4) thermal stresses within the blade.

To calculate all these stresses is impractical; the number of boundary conditions is formidable, and a (properly manufactured) blade usually fails by fatigue which means a cumulative calculation of the stress history of the material is needed. The procedure adopted by most stress analysts is to model the loadings on the blade in a very simple way. These models are, of course, augmented as often as possible by insight gained from hardware tests and/or numerical solutions for simplified boundary conditions.

A fairly standard approach is outlined below for the preliminary estimate of blade stresses for radial blades. Some special calculations performed for backward leaning blading are described later. The approach used for radial blades was as follows:

1) The blades were considered to be cut into radial strips to calculate the average tensile stress in the root. This calculation was performed ignoring the fillet radius at the blade root.

2) The material properties were derated to account for vibration. The diminution of properties depends on the type and number of blade natural frequencies present within the operating range of the machine. Typical vibration allowances are between 1.379×10^4 and 5.516×10^4 Newton/meter^2.

3) The impeller disc was designed so as to minimize the blading deformations. That is, no direct account of the stresses due to displaced boundary conditions was attempted.

4) Thermal stresses were estimated at stations along the blade from a one-dimensional heat transfer analysis.

The calculations were performed in full only for several very critical stress configurations. Usually then, only Item (1) was effected for a design and this quantity was calculated only because it is necessary input to calculate disc stresses.

Creare has no prior experience calculating stresses in backward leaning impellers, so a preliminary investigation of the effects of the backward lean per se was undertaken. For this purpose, the centrifugal force was decomposed into components along and perpendicular to the blade. To first order, the increase in stress due to the backward lean is contained in the perpendicular components of force.* The stresses in the blade were then calculated as follows:

A section was cut perpendicular to the blade and extending into the depth of the blade axially. The forces due to the centrifugal loading on a small element were determined by the mass of the element, hence the density of the material, the square of the rotation speed, etc. These forces produce moments in the blade section. These resultant stresses were calculated using the slender beam approximation:

$$\sigma = \frac{Mc}{I}$$

where:

M = moment at the section

$\frac{I}{c}$ = section modulus

It is then a straightforward process to determine the distribution of stress along the blade. This has been done for two simple shapes represented by a linear and a parabolic taper. The variation in stress along the beam is different for the two cases; for present purposes, it was of interest to compare the maximum stress occurring in the root for the two shapes versus taper ratio -- taper ratio being the ratio of thickness at the root compared to the thickness at the tip of the blade. The effect of a blade root fillet was not considered in these calculations in the anticipation that the calculations are conservative.

*The uniaxial equivalent stress of the biaxial stress field is approximately the difference of the principal stresses. Thus in the worst case, the compressive stress due to bending of the blade would add to the tensile stress to determine the equivalent stress.

Preliminary Design Analyses

The Creare design methodology was applied to a number of radial bladed and backswept bladed designs ($0° \leq \beta_{2b} \leq -40°$). Various inducer performance maps and diffuser designs using both meridional and radial plane channel diffuser divergence were studied. Only the final design calculations using the "best" projected inducer performance and radial plane diffuser divergence, as discussed in the previous section, are presented here.

Speed and inducer hub-to-tip ratio - The future use of this stage as a "workhorse" compressor dictated the choice of a low rotational speed. An upper limit of inducer lead edge $(r_h/r_t)_1 = 0.5$ was selected. As described in the previous section, the corresponding rotational speed of 75,000 RPM was then specified to meet the requirement of inducer relative Mach number $M_{rel\ 1t} = 1.2$. The specific speed of the compressor ($\beta_{2b} = -30°$) at this rotational speed is $N_s = 0.633$.

It is common belief that best efficiency performance for high pressure ratio compressors is attained at high specific speeds (order of $N_s = 0.775$. The preliminary design analysis was used to examine the predicted stage efficiency increase at the maximum allowable rig speed N = 82,650 RPM for $\beta_{1t} = -65.2°$ and $-60.3°$, $\beta_{2b} = -30°$ and $(r_h/r_t)_1 = 0.3$. The results for both C_{x1} values (corresponding to the β_{1t} values) are tabulated below. No great significance should be attached to the difference in efficiencies for N = 75,000 RPM cases.

TABLE I - EFFICIENCY VARIATION WITH SPEED

Inlet Axial Velocity C_{x1} (meters/s)	Total to Static Efficiency, η_{T-S} (Backward Leaning Angle $\beta_{2b} = -30°$)	
	Rotational Speed N=75,000 RPM; Z_o=0.5	Rotational Speed N=82,650 RPM; Z_o=0.3
167.6	76.3%	76.8%
195.7	76.4%	76.8%

The increase in η_{T-S} of approximately 0.5 points comes principally from a reduction in friction work. This stems from a smaller impeller tip radius (r_2) for the higher speed case ($N_s = 0.698$) in providing an equal pressure rise across the impeller. The sensitivity of efficiency at the design point (η_{DP}) is $\partial \eta_{DP} / \partial N = 0.6\%$ per 10,000 RPM.

Thus going to a higher rotational speed (N = 82,650 RPM) would raise the predicted stage efficiency about 0.5 points; this was not considered warranted relative to the desire to maintain low rotational speed.

Design point inducer performance/impeller exit swirl parameter - Early in the preliminary analysis, a study was made of the sensitivity of stage performance (η_{T-S}) and flow path dimensions to the independent design parameters of inducer tip diffusion ratio DR and impeller exit swirl parameter λ_{2*}. This study was carried out over the range of backswept blade angles $0 \leq \beta_{2b} \leq -40°$. The results are presented in Figures 10 through 12.

Figure 10 displays the stage efficiency η_{T-S} at the design point as a function of inducer DR for $\beta_{2b} = -30°$ and $-40°$ for several values of λ_{2*} ($\lambda_{2*} = 2.25$ and 2.75). The influence of DR is readily apparent as is the effect of increased blade backsweep in raising stage efficiency.

Sensitivity factors are displayed in the table below for the match point efficiency with respect to the input parameters β_{2b}, DR, $(\bar{m}_w/\bar{m})$, λ_{2*}, and N. These sensitivity factors are useful for deciding the optimum set of trade-offs in a situation requiring a compromise among the several input parameters.

The sensitivity factors are expressed as $\partial \eta_{DP} / \partial X$ where X is an independent (input) variable and η_{DP} is the design point total-to-static stage efficiency. These sensitivity factors were obtained from the results of a large number of calculations of design configurations using several values of the above input parameters. To obtain these factors, two large numbers were subtracted

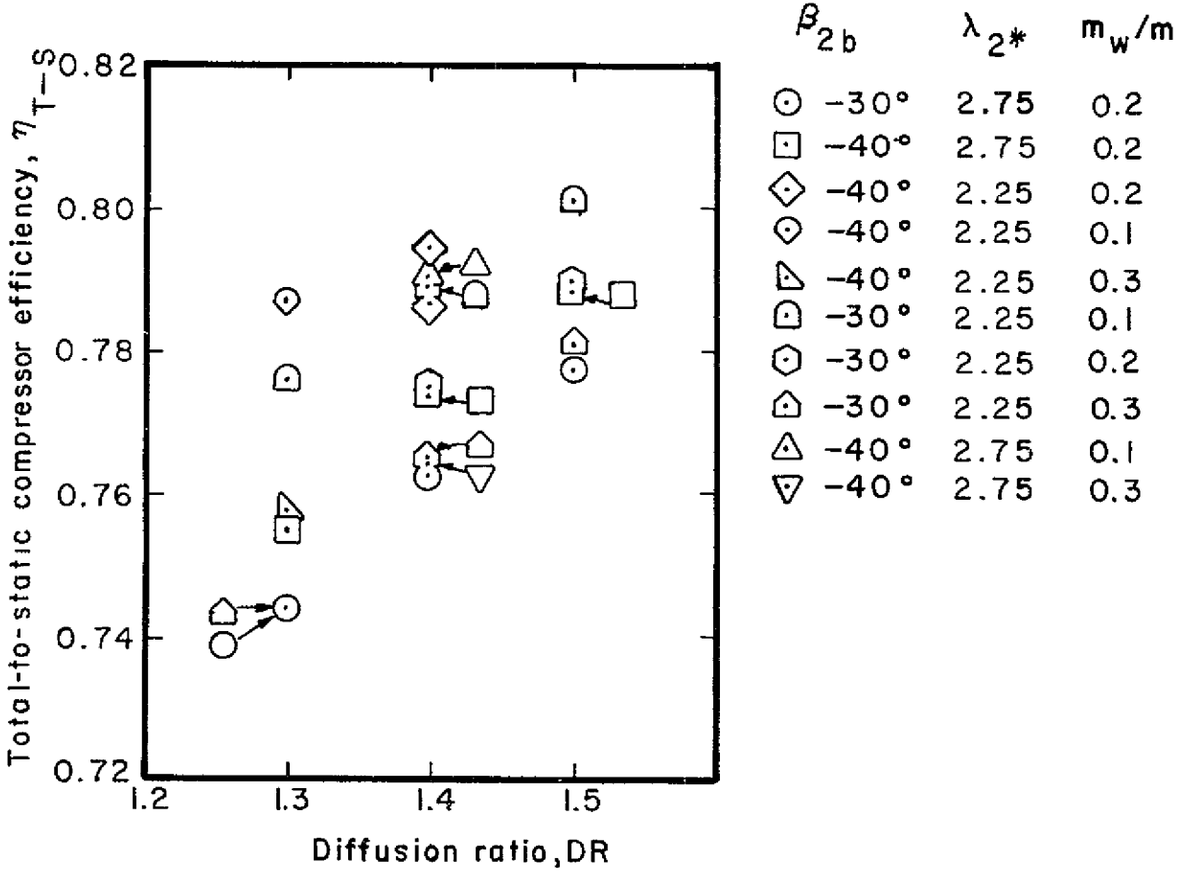

Figure 10 — Variation of Compressor Efficiency with Design Parameters

from one another and this introduces some uncertainty. Further error may result just from the tolerances allowed within the computer programs to match the required input quantities.

The following table displays a representative value of these sensitivity factors that are valid around the range of designs reported herein.

TABLE II - SENSITIVITY FACTORS

Rate of Change of Total-to-Static Efficiency per Change in Variable, X $\partial \eta_{DP}/\partial X$	Variable X				
	Backward Leaning Angle, β	Diffusion Ratio, DR	Wake Mass Fraction, m_w/m	Swirl Parameter, λ_{2*}	Speed, N
	0.6 pts per -10°	1.6 pts per 0.1	-1.3 pts per 0.1	-1.1 pts per 0.5	0.6 pts per 10,000 RPM

Figure 11 displays the impeller exit tip depth b_2 as a function of DR and λ_{2*} with β_{2b} as the parameter. The strong dependence of impeller tip depth on blade angle β_{2b} and λ_{2*} is apparent.

Figure 12 shows the diffuser vaneless space radial dimension as a function of the same variables used in Figure 11. The vaneless space radial dimension (Δr) equals $r_3 - r_2$, where $r_3 = 1.05 \times r_2$ with r_3 defining the diffuser vane leading edge radius. The Δr variation is primarily a function of blade angle β_{2b}.

These results were used to assist in the selection of the proposed λ_{2*} and amount of blade backsweep. Because of the strong sensitivity of b_2 with change in λ_{2*}, a value of $\lambda_{2*} = 2.75$ was selected for all of the final design calculations. This provided the largest value of b_2 consistent with empirical design correlations

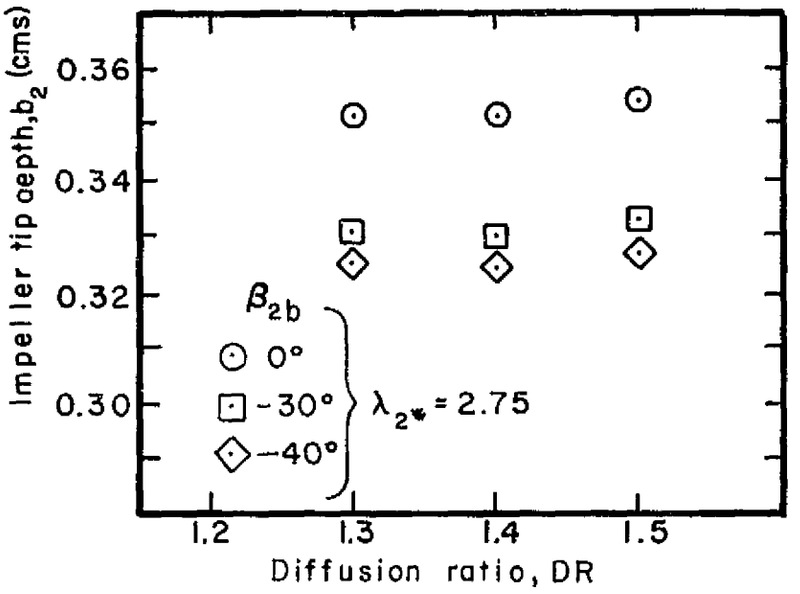

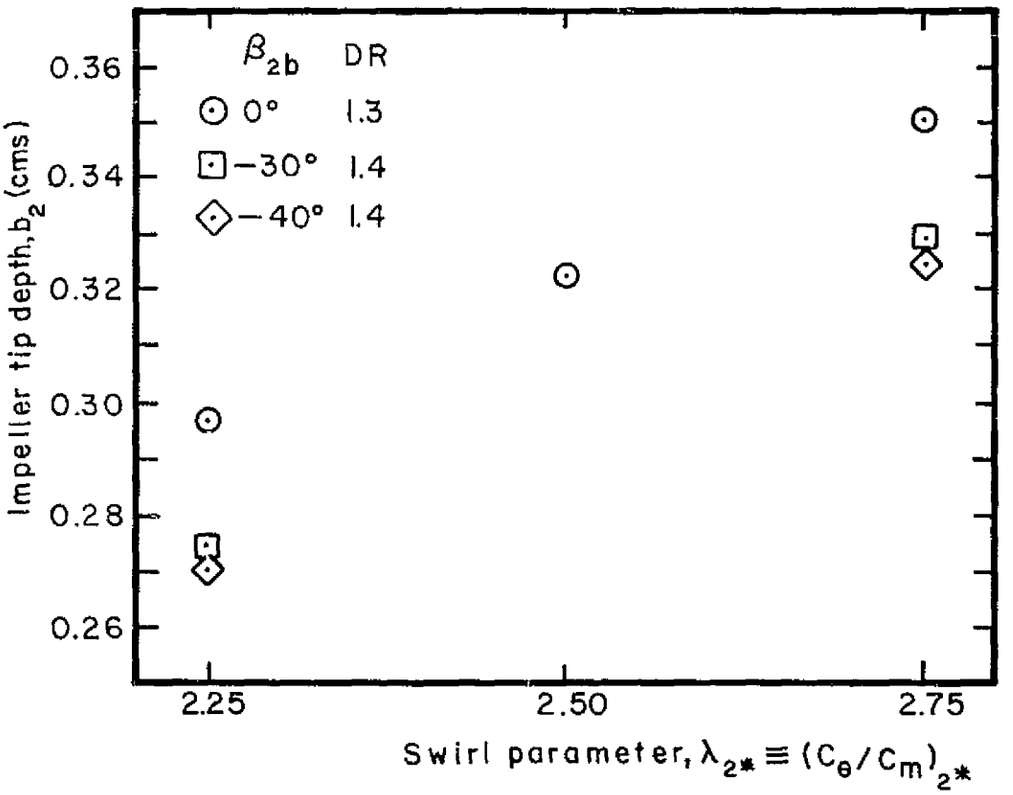

Figure 11 — Impeller Exit Depth Variation with Design Parameters ($m_w/m = 0.2$)

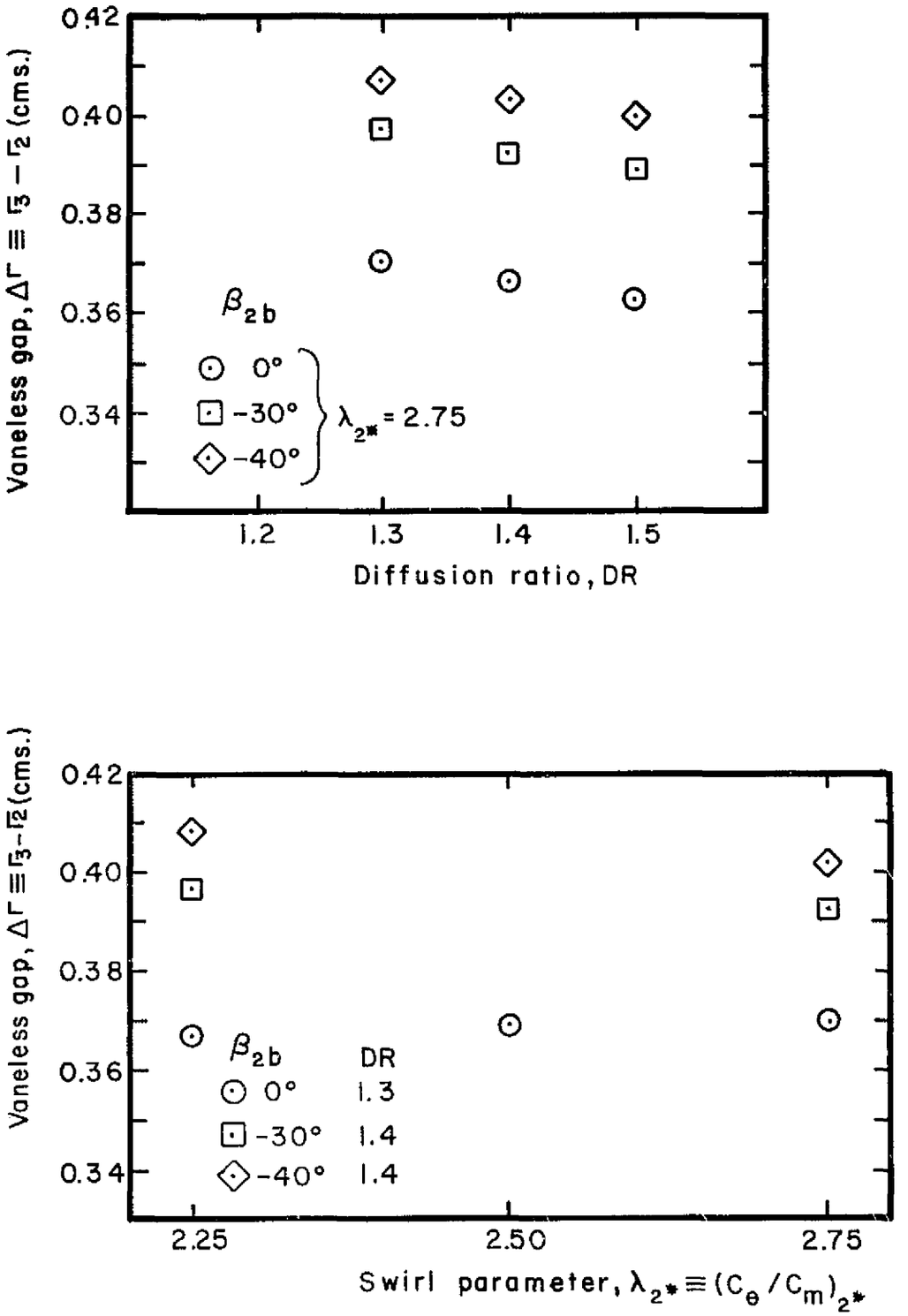

Figure 12 —Vaneless Space Radial Dimension Variation with Design Parameters ($m_w/m = 0.2$, $r_3 = 1.05\, r_2$)

on the optimum value of λ_{2*} as discussed under "Design Procedures". A large value of b_2 is advantageous for use with LDV instrumentation.

DR values have very little influence on the flow path physical dimensions. Hence DR at the design point was selected to provide reasonable range to choke at design speed using the final inducer map selected for this design study. The inducer map and selection of design DR were discussed previously.

It is evident that efficiency can be increased with backsweep. However, the impeller tip depth b_2 dimension size is decreased somewhat with large backsweep ($\beta_{2b} = -30°$ to $-40°$) and, as discussed previously, the design proposed was one of some degree of backsweep in order to seek increased efficiency performance.

Disc and impeller blade stress calculations - Using the preliminary stress analysis procedures for blade stress presented previously, the following calculations were made for disc and blade stresses.

Past experience with many designs has shown that it is possible (with careful design) to limit peak disc stresses to

$$\sigma_{max} = (0.75 - 1.0)\ \rho U_2^2\ \frac{3+\nu}{8}$$

where:

ρ = material density
U_2 = tip speed
ν = Poisson's ratio

A preliminary decision was made to use titanium 6Al-4V for the design because it offered the best strength to weight ratio of candidate materials whose strength to weight ratios versus temperature were known.

The table below shows the expected tip speed limits for the impeller at a maximum bore temperature of 93°C.

TABLE III - TITANIUM STRESS LIMITS

Peak Allowable Tip Speeds for the Impeller at 93.33°C Using 6Al-4V Titanium	
Stress Limit Condition	Range of Limiting Tip Speeds, m/s
0.2% yield stress = 6.619×10^8 Newton/m^2	603.5 - 670.6
Ultimate strength = 7.446×10^8 Newton/m^2	640.1 - 746.8

In summary, it is feasible to operate at tip speeds between 600 and 670 m/s, and with careful design, it should be possible to achieve tip speeds as high as 750 m/s -- with well-known materials. It was concluded that no problem should arise in designing an impeller to run at the highest tip speed proposed to meet the aerodynamic performance targets, provided blade backsweep was not too large.

The following table shows the comparison between the non-dimensional stress in the root of the blade and the taper ratio for two cases, a linear and a parabolic taper.

TABLE IV - STRESS FUNCTION VS. TAPER RATIO CONSTANT

k	0	0.5	1.0	2.0	3.0	4.0	6.0
f_1, linear taper	0.5	0.259	0.167	0.093	0.063	0.047	0.031
f_2, parabolic taper	0.5	0.241	0.146	0.074	0.047	0.033	0.020

where:

$t = 1 + kx$ (linear taper) or

$t = 1 + kx^2$ (parabolic taper) and

t = blade normal thickness distribution (normalized)

x = distance along blade from tip to root (normalized)

The quantity f is defined by

$$f(x) = [1/t(x)]^2 \int_0^x (x-z)z\,dz$$

and k is related to the taper ratio by $k = (t_{hub}/t_{tip})-1$.

Assuming a taper ratio of 2, a normalized stress of approximately 0.15, the peak stress in the blade root was calculated. The equation for peak stress is:

$$\sigma = \frac{fh^2\ 6\rho r\omega^2\ \sin\beta_b}{t_{tip}}$$

The preliminary aerodynamic design only gave the blade height at the tip of the wheel. The stress was calculated below for this case:

$r = r_2 = 7.976 \times 10^{-2}$ m

N = 75,000 RPM

$\beta_b = -30°$

$h = b_2 = 3.302 \times 10^{-3}$ m

$t_{tip} = 1.27 \times 10^{-3}$ m

k = 1.0

$\sigma = 8.481 \times 10^7$ Newton/meter^2

The above stress of 8.481×10^7 Newton/m^2 was low enough that the extra loading due to the centrifugal effect on backward curved blades did not appear to be of paramount importance. However, it was expected that the maximum bending stress would occur at less than the tip radius.

Results

Aerodynamic states and stage geometry - Table V displays the important aerodynamic flow states and stage geometry at the design point for four values of impeller blade backsweep ($\beta_{2b} = 0°, -20°, -30°, -40°$).

Figure 13 displays the increase in predicted stage design point efficiency η_{DP} as a function of blade angle β_{2b}.

TABLE V - RESULTS FOR RADIAL AND BACKSWEPT BLADE DESIGNS (DESIGN POINT CONDITIONS)

	Radial Blade Design	Backswept Blade Design		
β_{2b}	0°	-20°	-30°	-40°
pr	8	8	8	8
m	9.072×10^{-1}	9.072×10^{-1}	9.072×10^{-1}	9.072×10^{-1}
N	75,000	75,000	75,000	75,000
$M_{rel\ lt}$	1.2	1.2	1.2	1.2
C_{x1}	195.7	195.7	195.7	195.7
U_{1t}	343.2	343.2	343.2	343.2
α_1	0	0	0	0
β_{1t}	-60.3	-60.3	-60.3	-60.3
p_{oo}	1.014×10^{5}	1.014×10^{5}	1.014×10^{5}	1.014×10^{5}
T_{oo}	288.2	288.2	288.2	288.2
β_{1tb}	-56.3	-56.3	-56.3	-56.3
M_{1t}	0.583	0.583	0.583	0.583
W_{1t}	395.3	395.3	395.3	395.3
C_{2J}	577.0	525.8	498.0	463.9
C_{T2J}	489.8	445.6	425.5	403.6
C_{M2J}	304.8	279.3	258.9	229.2
C_{2w}	589.5	586.1	585.2	578.8
C_{T2w}	582.5	580.3	579.4	573.0
C_{M2w}	90.2	82.6	81.4	82.75
W_{2J}	318.5	324.3	327.7	331.0

Continued..

Table V - Continued

β_{2b}	0°	-20°	-30°	-40°
W_{2w}	90.2	87.87	94.00	108.1
M_{2j}	1.427	1.280	1.201	1.109
M_{2w}	1.356	1.319	1.300	1.271
$M_{rel\ 2j}$	0.791	0.791	0.792	0.792
W_{sep}	277.3	277.3	277.3	277.3
DR	1.425	1.425	1.425	1.425
ϵ	0.494	0.497	0.483	0.450
P_{o2}	1.117×10^6	1.034×10^6	9.997×10^5	9.515×10^5
P_{o2W}	1.007×10^6	1.082×10^6	1.138×10^6	1.172×10^6
$\bar{P}_{o2}$	1.096×10^6	1.041×10^6	1.027×10^6	9.997×10^5
P_2	3.385×10^5	3.833×10^5	4.123×10^5	4.433×10^5
T_{2j}	406.2	420.8	429.4	438.3
T_{2W}	470.3	492.4	516.7	518.1
T_{o2j}	568.3	555.3	550.1	542.9
T_{o2W}	637.2	656.7	668.9	677.8
U_2	582.5	610.5	626.4	642.2
T_{2*}	440.3	453.4	460	465.4
T_{o2*}	582.2	575.6	573.9	570
T_{o2**}	593.9	588.3	587.2	583.9
P_{2*}	3.827×10^5	4.220×10^5	4.447×10^5	4.661×10^5
P_{o2*}	1.034×10^6	9.928×10^5	9.860×10^5	$9.653.10^5$
M_{2*}	1.288	1.181	1.133	1.080
Δp_{o2}	5.716×10^4	4.806×10^4	4.033×10^4	3.034×10^4

Continued..

Table V - Continued

β_{2b}	0°	-20°	-30°	-40°
C_{T2*}	508.4	472.4	456.3	437.4
C_{M2*}	184.9	171.8	166.0	159.1
C_{2*}	540.7	502.9	485.5	465.4
λ_{2*}	2.75	2.75	2.75	2.75
σ	0.873	0.877	0.882	0.889
M_4	0.95	0.95	0.95	0.95
P_4	5.709×10^5	5.571×10^5	5.523×10^5	5.426×10^5
P_{o4}	1.020×10^6	9.860×10^5	9.791×10^5	9.653×10^5
B_4	0.160	0.135	0.118	0.103
C_{p2*-4}	0.288	0.236	0.199	0.153
C_{p4-c}	0.541	0.581	0.610	0.634
C_{pD}	0.657	0.675	0.685	0.689
$\Delta\eta_{BF}$ (%)	3.0	3.0	3.0	3.0
$\Delta\eta_{RD}$ (%)	0.99	1.33	1.56	1.82
$\Delta\eta_{FC}$ (%)	1.19	1.60	1.87	2.18
$\Delta\eta_{SF}$ (%)	2.19	2.93	3.42	4.00
$\Delta\eta_{DM}$ (%)	2.76	2.44	2.08	1.61
$\Delta\eta_{D}$ (%)	12.04	10.36	9.52	8.87
$\Delta\eta_{IW}$ (%)	4.81	5.00	5.01	4.91
η_{ITT} (%)	87.24	86.62	86.49	86.48
η_{TS} (%)	75.20	76.27	76.98	77.62

Continued..

Table V - Concluded

β_{2b}	Geometry 0°	-20°	-30°	-40°
r_{1h}	2.187×10^{-2}	2.187×10^{-2}	2.187×10^{-2}	2.187×10^{-2}
r_{1t}	4.371×10^{-2}	4.371×10^{-2}	4.371×10^{-2}	4.371×10^{-2}
r_2	7.417×10^{-2}	7.772×10^{-2}	7.976×10^{-2}	8.179×10^{-2}
b_2	3.480×10^{-3}	3.327×10^{-3}	3.226×10^{-3}	3.175×10^{-3}
b_4	3.480×10^{-3}	3.327×10^{-3}	3.226×10^{-3}	3.175×10^{-3}
W_4	1.090×10^{-2}	1.133×10^{-2}	1.148×10^{-2}	1.166×10^{-2}
AS_4	0.32	0.29	0.28	0.27
r_3	7.798×10^{-2}	8.153×10^{-2}	8.382×10^{-2}	8.585×10^{-2}
$\Delta r (\equiv r_3 - r_2)$	3.708×10^{-3}	3.886×10^{-3}	3.988×10^{-3}	4.089×10^{-3}
#Diffusers	17	17	17	17
# Blades	19	19	19	19

Notes:

1. Mass flow in kilograms per second.
2. Velocities in meters per second.
3. Pressures in Newtons per square meter.
4. Temperatures in °K.
5. Angles in degrees.
6. Lengths in meters.

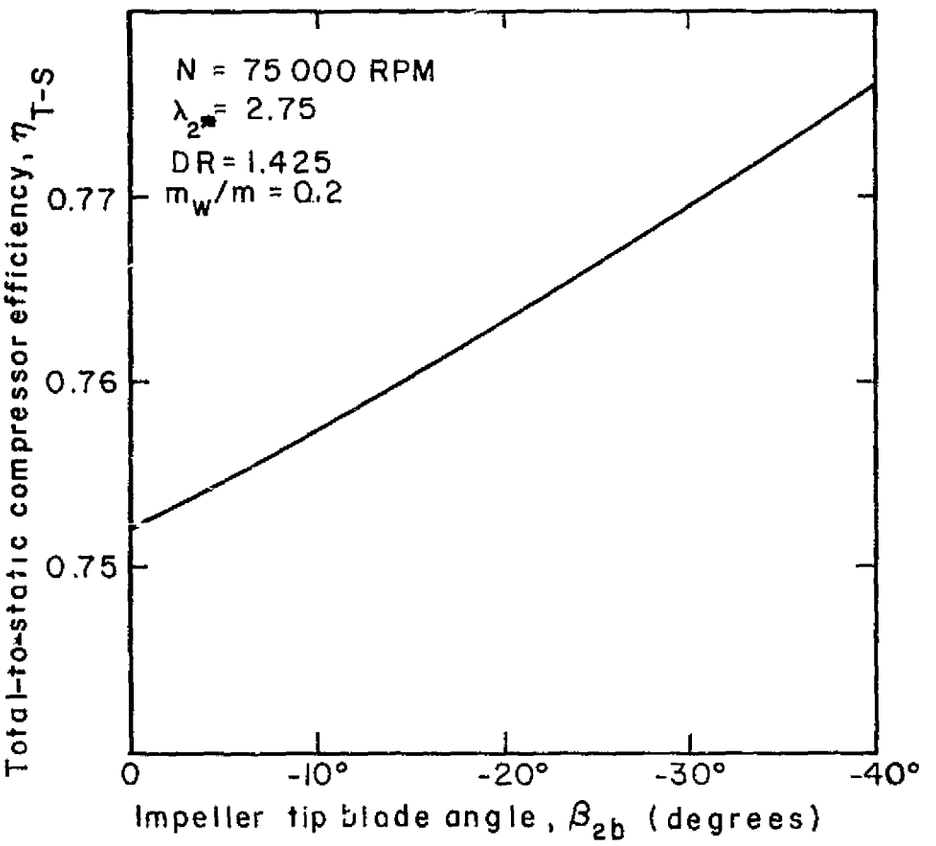

Figure 13 - Design Point Stage Efficiency as a Function of Impeller Blade Backsweep Angle

Figures 14 and 15 display the predicted performance at 100% speed for the designs with β_{2b}=0° and -30°, respectively.

Figures 16 and 17 show the inducer inlet and impeller exit velocity diagrams, respectively, for the two designs displayed in Figures 14 and 15 (β_{2b} = 0° and -30°).

A definition of the impeller meridional plan form and detailed blade shapes was not available as this type of calculation was performed as part of the final aerodynamic and mechanical design. An estimate of the impeller meridional configuration based on prior "experience" and assumed blade thickness distribution was used in performing the preliminary stress analyses.

Preliminary stress analysis - There are four chief areas of concern regarding the mechanical design of an impeller for high tip speed.

1) The disc material and design must be adequate to withstand the centrifugal loading imposed upon it during its required lifetime.

2) The blades must be adequate to withstand the centrifugal and thermal loading.

3) The blades (and disc) should be designed so that there are no severe vibration modes which can cause failure.

4) The impeller deflections during operation should be smaller than the clearances.

The preliminary stress analysis was directed toward areas (1) and (2) of the above. The aerodynamic design had not progressed to the point where it was possible to design mechanically with respect to areas (3) and (4).

The disc stress analysis indicates that it will be possible to operate the proposed designs up to tip speeds of order 670 m/s using titanium (6Al-4V). With careful design, tip speeds up to order of 750 m/s should be possible.

The first order blade stress analyses (see section on disc and impeller blade stress calculations) indicated that the backward leaning blade designs proposed would not meet difficulties re to blade stresses. However,

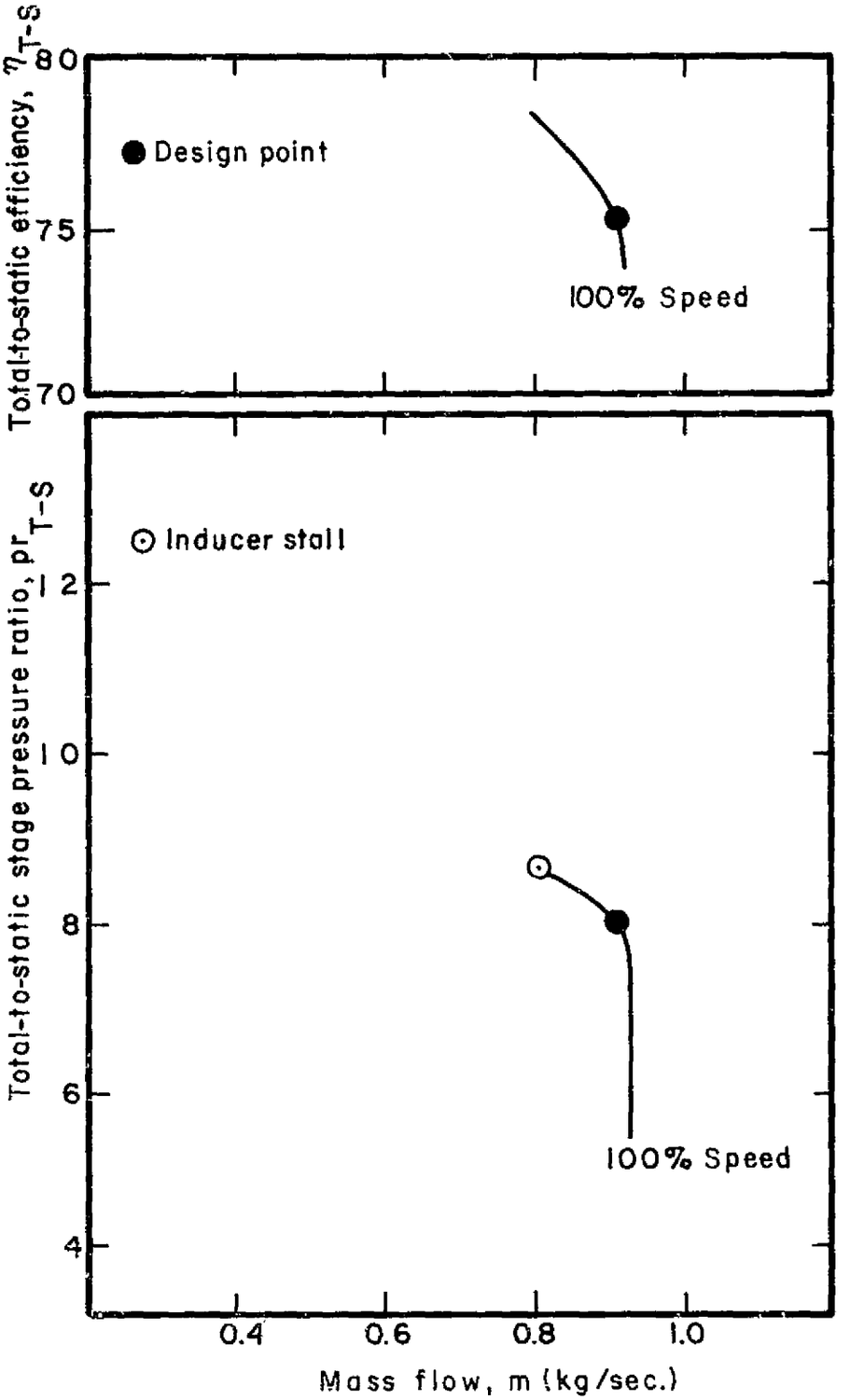

Figure 14 — Compressor Performance Map — $\beta_{2b} = 0°$

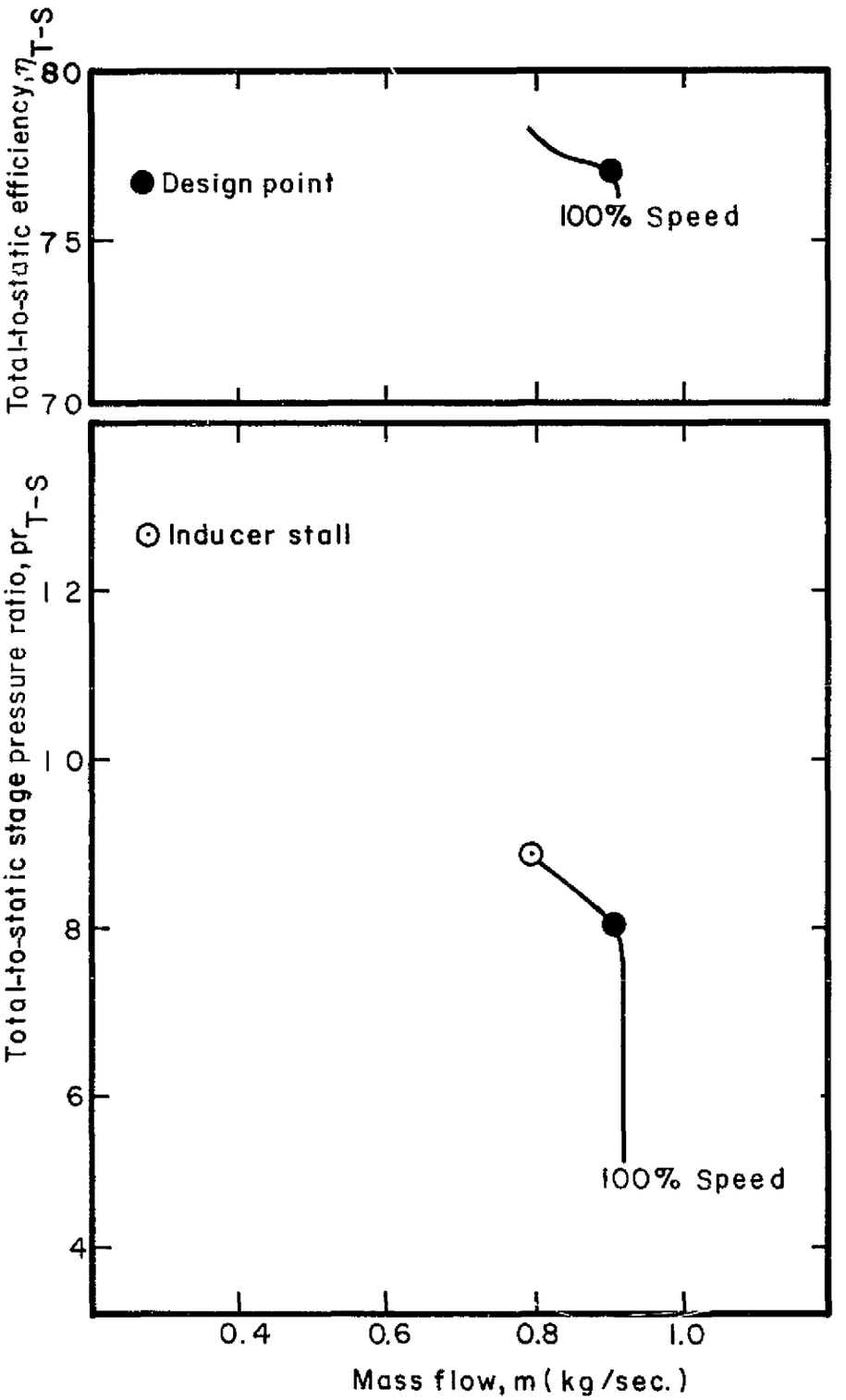

Figure 15 — Compressor Performance Map — $\beta_{2b} = -30°$

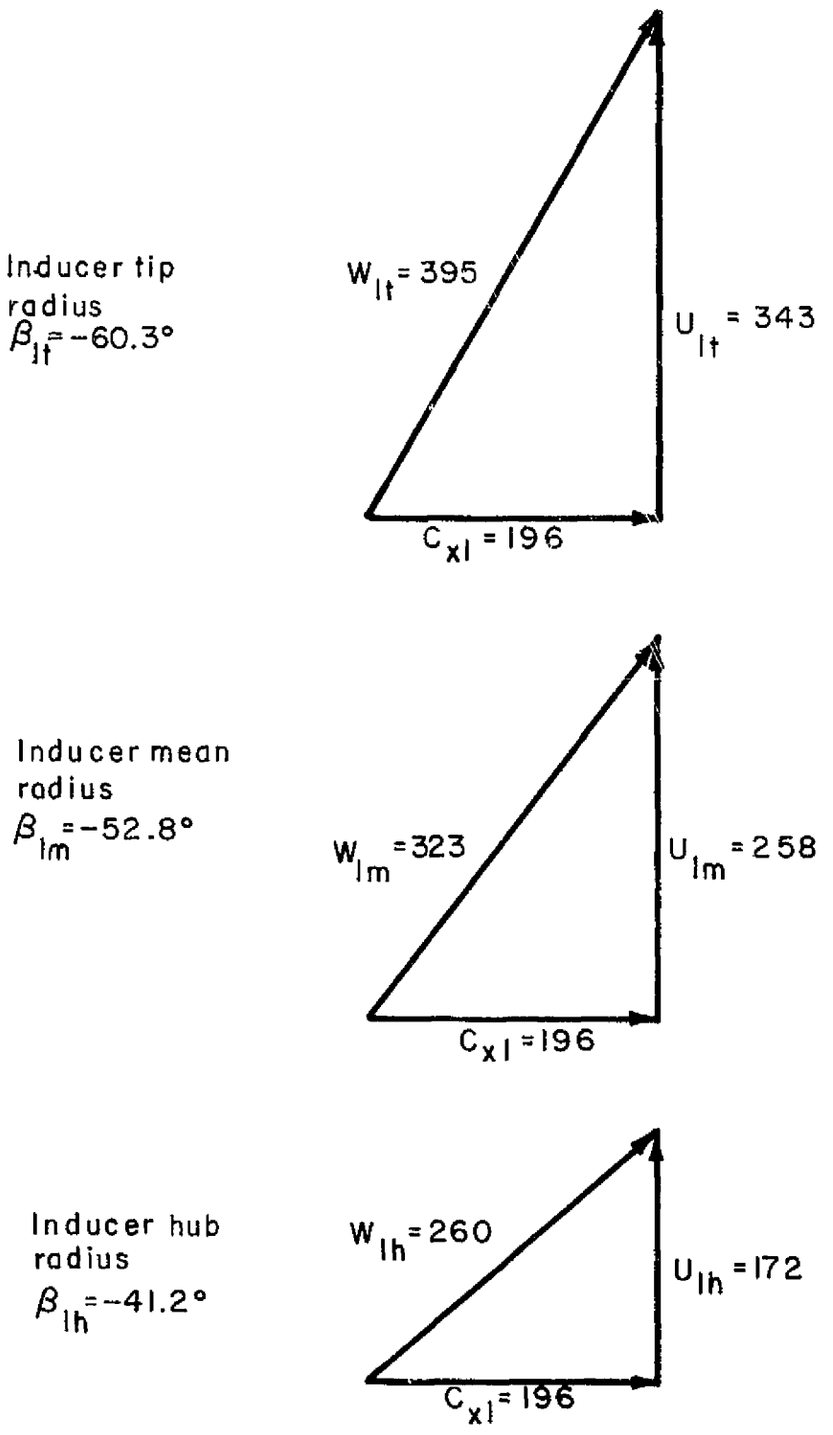

Figure 16 — Velocity Vector Diagrams at Inducer Inlet
(Velocities in meters/sec.)

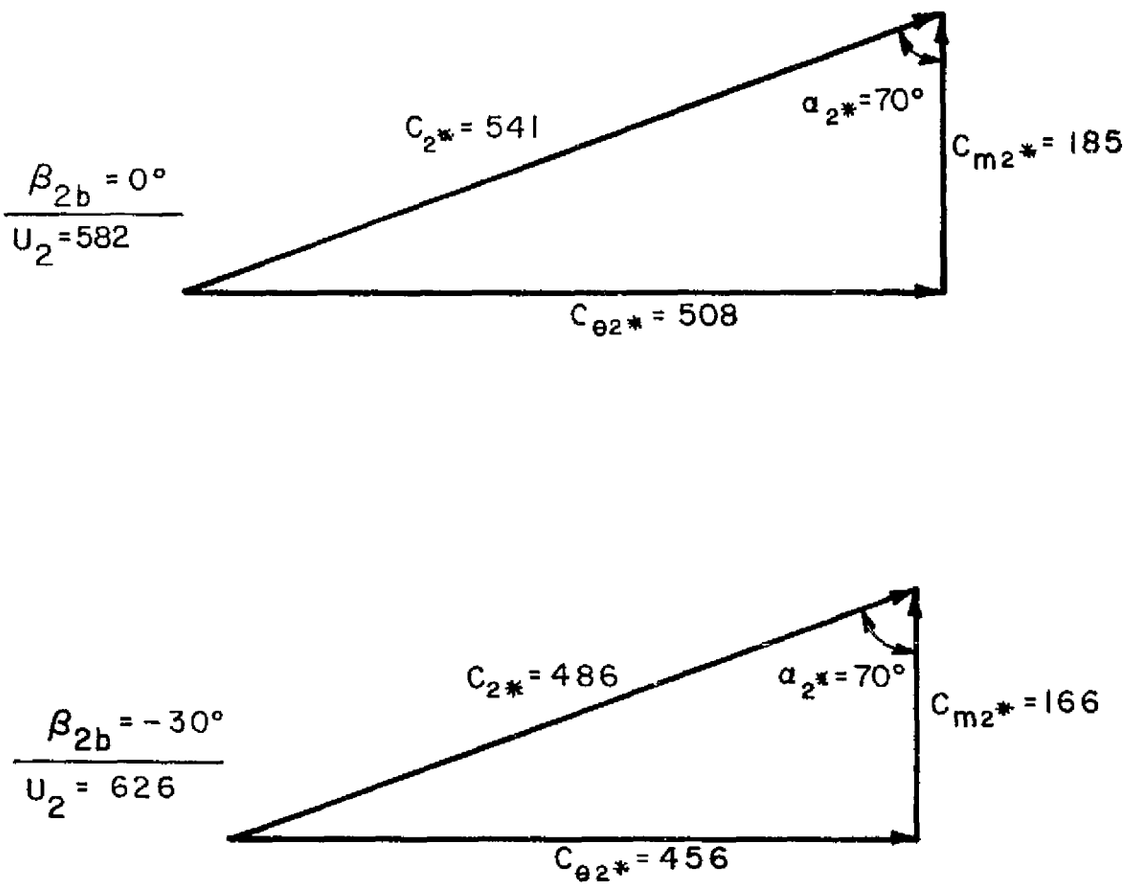

Figure 17 — Velocity Vector Diagrams at Impeller Exit $\beta_{2b} = 0°$ and $-30°$ (Velocities in meters/sec.)

these were very preliminary and approximate calculations and the final value of β_{2b} used for the final design had to await a more complete blade analysis that was made during the final mechanical design. At the same time, empirical evidence has demonstrated that impeller designs in titanium have been routinely run with $\beta_{2b} = -32°$ at tip speeds up to 701 m/s. Therefore, the proposed design for $\beta_{2b} = -30°$ appeared to be reasonable of attainment at the 120% overspeed required.

Conclusions/Recommendations

The following conclusions/recommendations were made on the basis of the preliminary design analysis and the contract requirements.

1. A rotational speed of 75,000 RPM with an inducer inlet hub-to-tip ratio = 0.5 was proposed. This speed produces a stage specific speed $N_s = 0.633$. The highest speed deemed practical* for this design (N = 82,646 RPM at hub-tip ratio = 0.3) would produce a specific speed $N_s = 0.698$, but only a predicted increase in stage efficiency of order of 0.5 points.

2. Stage efficiency increases on the order of 2 to 2.5 points at the optimum impeller design is changed from radial ($\beta_{2b} = 0°$) to backswept blades ($\beta_{2b} = -30°$ to $-40°$) respectively. The predicted efficiency of a radial bladed impeller ($\eta_{TS} = 75.2\%$) was judged too low to be representative of state-of-the-art performance at the design pressure ratio and mass flow. The performance ($\eta_{TS} = 77.0\%$ for $\beta_{2b} = -30°$ and $\eta_{TS} = 77.6\%$ for $\beta_{2b} = -40°$) with backsweep was sufficiently high to recommend that a backsweep design of $\beta_{2b} = -30°$ be selected for the final design.

*This upper speed limit is set by the LSM facility capability.

3. A 19 blade inducer/impeller was recommended with an inducer configuration established on the basis of empirical transonic axial compressor aerodynamic performance. A design with no splitters will reduce the uncertainties of aerodynamic design and provide a design more compatible with the use of LDV equipment.

4. A 17 channel, radial plane divergence diffuser was proposed to optimize the overall diffuser pressure recovery C_{pD} and provide the predicted stage efficiencies.

5. At the impeller tip speed for the proposed backswept design (of -30°), hub and blade stresses were not judged to be critical limiting factors at 100% speed. However, at 120% overspeed, these calculations showed that hub stress may be critical for the proposed backswept design. Confirmation of the preliminary stress analysis was made after the final mechanical design analysis.

AERODYNAMIC DESIGN OF INDUCER

General Philosophy

The general impeller design approach followed here recognizes two parts of the rotor - an inducer section and the remainder of the impeller. This view is being updated continuously at Creare as more and more is learned about the flow physics of the centrifugal rotor. Presently, it appears that the impeller (i.e., complete rotor) flow is best divided into an inlet flow (the inducer) and an internal flow within the impeller. The inlet flow is controlled by incidence and Mach number effects. The performance of the inlet region of the impeller is strongly determined by blade shape, blade thickness, blade number, taper ratio, hub-tip ratio, etc. This inlet region may be considered to extend about one throat width downstream of the throat.

Farther into the impeller, the flow appears to behave as if it were in a complicated diffuser. Overall diffusion within the impeller is controlled by the inducer inlet (as mentioned above), and impeller parameters such as blade shape, blade number, blade loading, discharge flow angle, etc. These parameters determine the relative velocity distributions on the four surfaces bounding the impeller channel. These relative velocity distributions and the incidence and relative Mach number effects at the inducer inlet determine the capability of the wall boundary layers to negotiate the adverse pressure gradients of the diffuser-like flow in the impeller. The boundary layer behavior is also exacerbated by blade tip leakage and rotational effects (Coriolis effects) which are not well understood. It appears from available empirical data that there may be a limiting impeller relative velocity diffusion ratio for a given area ratio impeller. Just how the impeller aerodynamic and geometric parameters will control the diffusion ratio within the impeller is not well established today either by theory or experimental evidence.

As will be described below, the inlet part (i.e., the "inducer") of the impeller was designed by a method of transference from axial compressors. The centrifugal

impeller will then have ensured excellent and predictable inlet performance.

The rear portion of the impeller has been designed to give good "diffuser-like" characteristics by controlling the velocity distributions on critical surfaces (the suction surfaces at the tip and hub). By this means, the design should attain the impeller discharge conditions predicted in the Preliminary Design Phase.

Inducer Design Method

The design of the inducer blade geometry is based upon a controlled scaling of a high performance transonic rotor. The progenitor axial fan used in this design is a Pratt and Whitney propulsion fan (Reference 2). The inducer map used in the Preliminary Design Phase was based on data for this transonic rotor. The basis of the design procedure is the logical assumption that the inducer performance will be replicated if the geometrical and aerodynamic parameters of the original transonic fan blading are duplicated. Clearly, not all these parameters can be duplicated; nevertheless, an attempt was made to duplicate what are believed to be the most important ones.

Design parameters - The most important parameters are deemed to be:

- approach relative tip Mach number, $M_{rel\ lt}$,
- blade tip pitch to chord ratio, $(s/c)_t$,
- approach incidence, i_m (camber line),
- blade suction surface profile,
- blade "throat" to approach flow area ratio, A_{min}/A_{rel}.

The blade-tip flow region is transonic and is believed to be the most critical aerodynamically (in terms of the above parameters) for duplicating the fan

performance. Consequently, emphasis was placed on the tip section in performing the basic scaling. The inducer blade shape, particularly in the hub region, will diverge significantly, behind the throat, from the original transonic blading of the progenitor fan. This will be evident from the design procedures described below. However, as a consequence of the low approach relative Mach numbers, this portion of the blading is thought to be less critical to the replication of the rotor performance than is the tip section.

Finally, the rotor performance is assumed to be describable in terms of blade element performance. The rotor performance should be essentially duplicated if the critical parameters (listed above) of each blade element are maintained, even if the blade elements are stacked differently than for the original fan.

The above philosophy is reflected in the detailed design procedures below. The two major steps in this procedure provide:

1) fan parameters (i_m, A_{min}/A_{rel}, suction surface profiles) from the progenitor blading, and

2) the blade characteristics for the present impeller by the maintenance of these parameter values.

The geometric quantities discussed above are defined in Figure 18.

Design Procedures

The fan blade profiles are defined in coordinate form on a number of cylindrical sections. The relevant parameters for each of these sections are to be calculated and the constancy of these parameters maintained in defining the blading for the present design.

Scaling factors - Geometric similarity is ensured by scaling all dimensions in the ratio of the blade pitch at the tip, between the fan and the present inducer as follows:

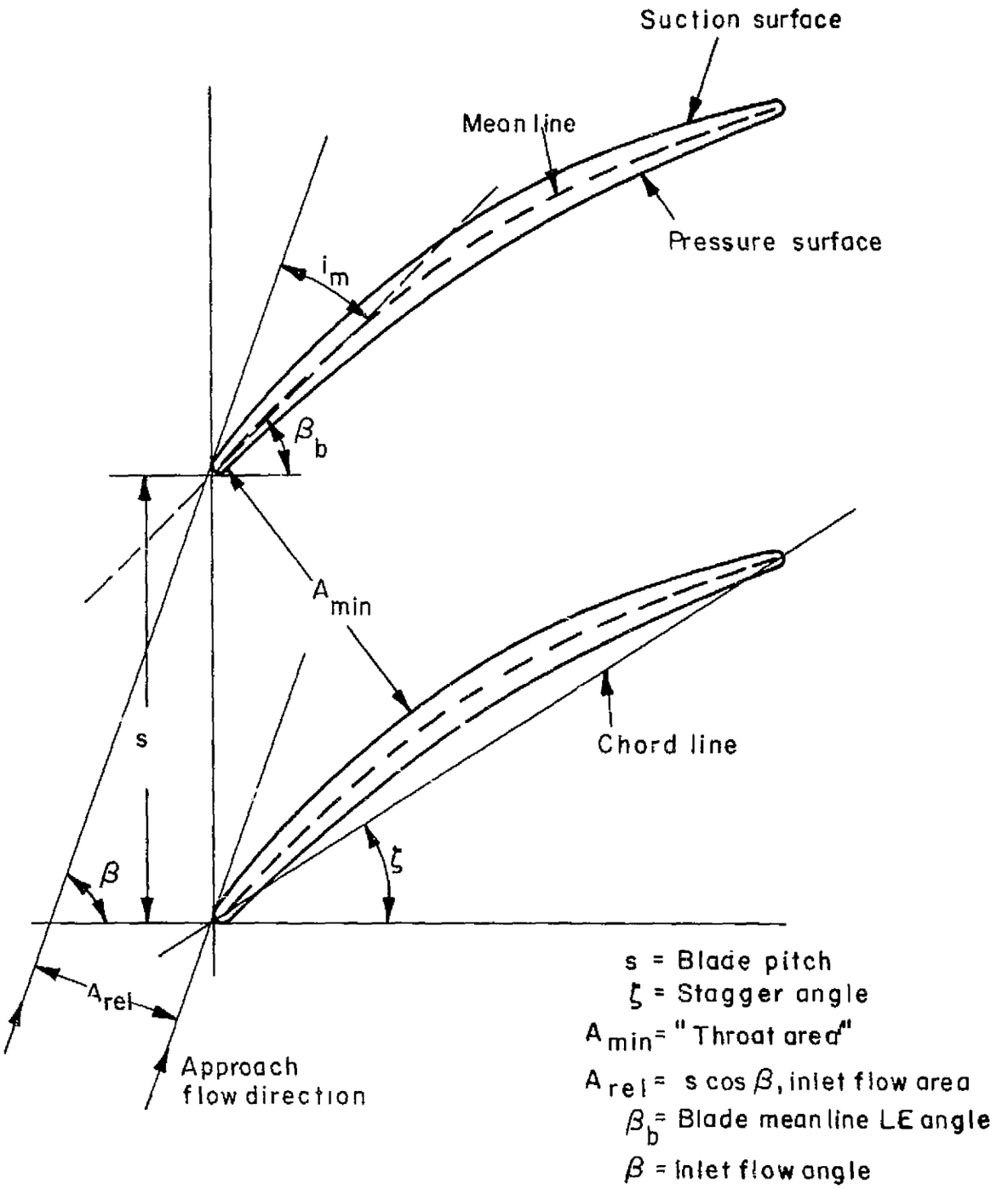

Figure 18 — Definition of Inducer Geometric Parameters

$$s = \text{pitch} = \frac{2\pi\, r_{lt}}{Z_i}$$

where:

r_{lt} = leading edge tip radius

Z_i = blade number

$$S_{fan} = \frac{2\pi(78.6206/2)}{24} = 10.2914 \text{ cm}$$

(Reference 2, Table 7, Page 68)

$$S_{inducer} = \frac{2\pi \times 4.3716}{19} = 1.4457 \text{ cm}$$

$$\text{scaling factor} = \frac{S_{inducer}}{S_{fan}} = 0.1405$$

A number of fan cylindrical sections are given in Appendix 9 of Reference 2. These sections were scaled by the above factor to provide the basic blade sections to be used in the present design, i.e.:

$$(X,Y)_{inducer} = \frac{S_{inducer}}{S_{fan}} (X,Y)_{fan}$$

where:

X,Y = coordinates of blade given in Appendix 9 of Reference 2. These blade sections were "laid out" to 20x scale.

Fan stagger angles - In Appendix 9 of Reference 2, the static fan stagger angles (ζ_{static}) for each cylindrical section are given. The rotating stagger angles ζ_{rot} (the change is due to the untwist of the blades caused by rotating inertia forces) were obtained by substracting an amount ($\beta_{b\ static} - \beta_{b\ rotating}$) from the static stagger angles. ($\beta_{b\ static} - \beta_{b\ rotating}$) was deduced from Figure 20 (Reference 2). The basic assumption implied is that each section rotates as a solid body about the leading edge.

Fan A_{min} values - A_{min} is the "throat" dimension for a cylindrical section. A_{min} was measured from a drawing wherein two adjacent fan blade profiles are drawn at the appropriate fan pitch (from Appendix 9 of Reference 2 and stagger angle as defined above). A_{min} then corresponds to the "throat" dimension and was measured from the drawing. This was easily and accurately done by using the 20x section drawings for the present design. If A_{rel} is calculated using the same scale geometry, then the A_{min} to A_{rel} ratio will be the same as for the fan. An important feature in the above approach is that the fan stagger angles were retained.

Fan blade setting angles - The blade setting angles on cylindrical surfaces are needed for the fan rotor for calculating A_{rel} and the new stagger angles. Unfortunately, Reference 2 does not give the blade setting angles on cylindrical surfaces, but only on conical streamline surfaces used in the aerodynamic calculations. The cylindrical surface values were checked in an approximate way and were found to differ by at most 1° from the conical surface values. Furthermore, the largest difference occurs at the least important location, that is at the hub where the approach relative Mach number is low. Consequently, the blade setting angle distribution (Figure 19) as given in Reference 2 was used to generate the A_{rel} values.

Fan incidence angle distribution - The consistent fan incidence distribution with span is that corresponding with the design tip Mach number (1.2) and tip incidence angle (4°). For the present design, the design tip Mach number of 1.2 corresponds to approximately 110% of design speed (N_D) for the progenitor fan.

The incidence variation with % span for the present design tip conditions, taken from Reference 1, is shown in Figure 20.

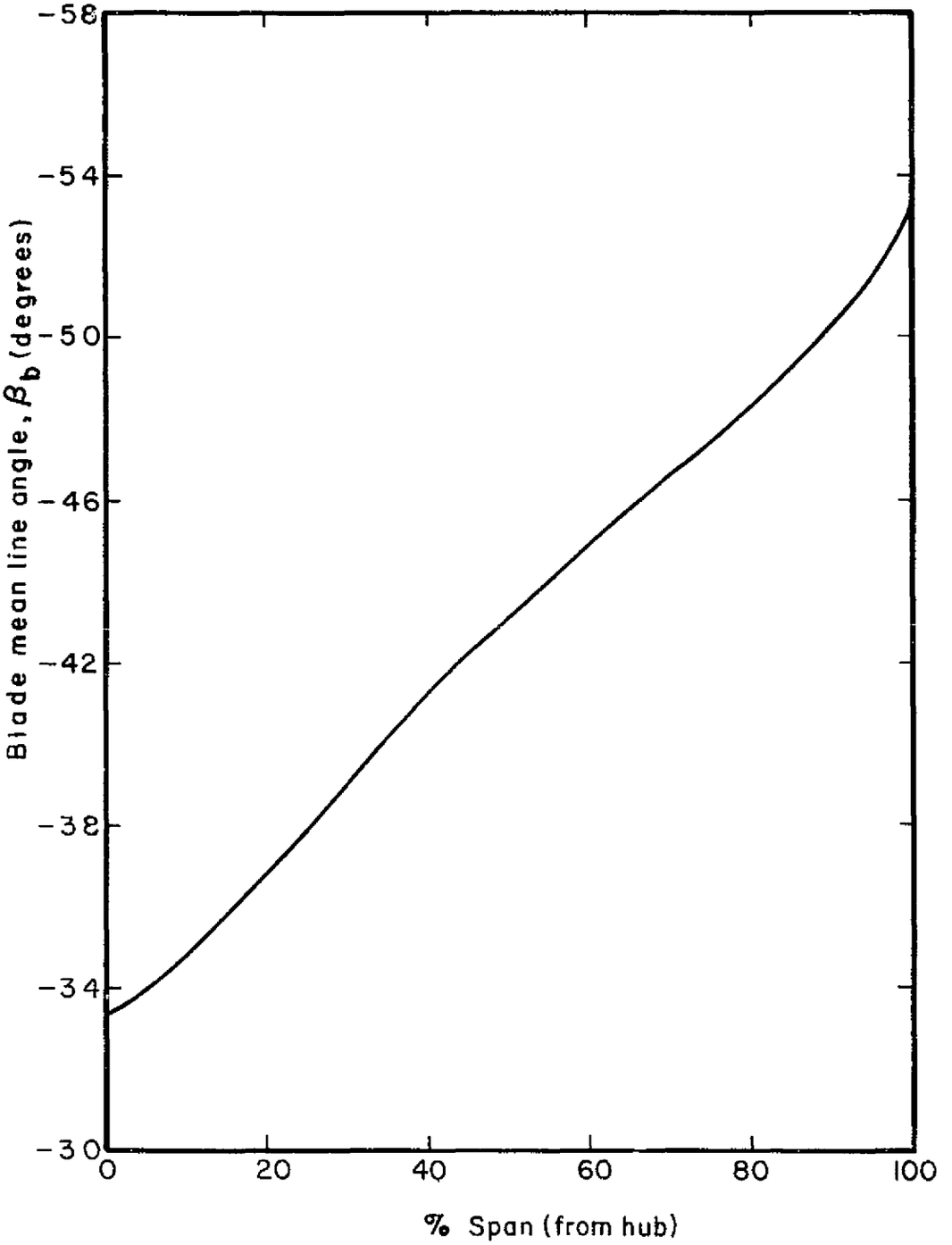

Figure 19 — Blade Mean Line Angle Distribution at Rotor Leading Edge (on Stream Surfaces)- P&W Blading

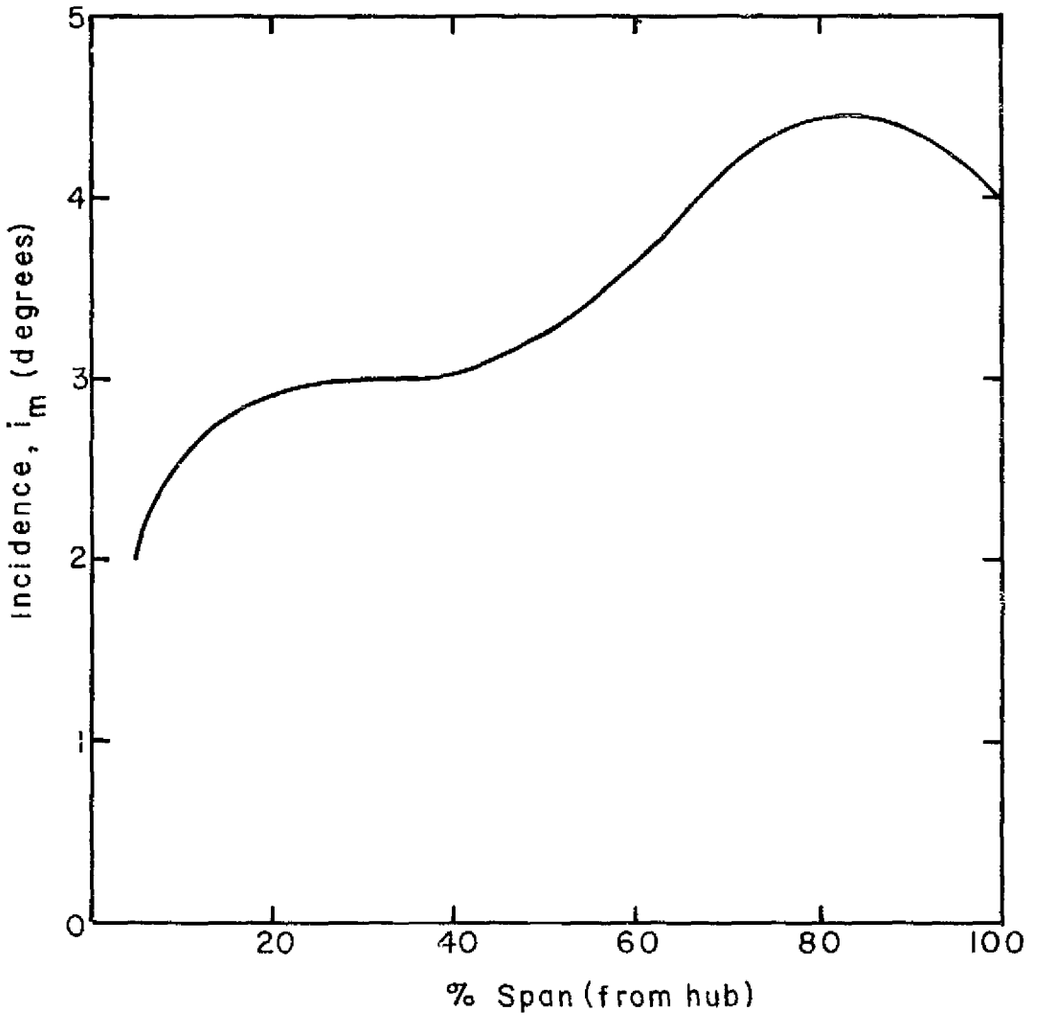

Figure 20 – Incidence Distribution at Rotor Leading Edge

Fan A_{rel} values - The approach A_{rel} values were calculated from

$$A_{rel} = s \cos \beta$$

where β is the fan section air angle calculated from

$$\beta = \beta_b - i_m.$$

β_b is picked off Figure 19.
The A_{rel} for each section for the 20x scale geometry was calculated. The A_{min}/A_{rel} ratios for the progenitor fan then follow from the previously measured A_{min}'s

Up to this point, all the required fan parameters have been generated. From this information and the design intent of maintaining constancy of these parameters, the quantities A_{min} and ζ_{rot} (which together with the scaled profiles define the blading) were calculated as indicated below.

Inducer A_{min} values - The A_{min} values for each cylindrical section are calculated from the constancy of A_{min}/A_{rel} and the calculated value for A_{rel}. The latter quantity is calculated from

$$A_{rel} = s \cos \beta$$

where β is the approach flow air angles deduced from the potential flow calculations and s is the blade pitch for the particular section.

Stagger angles, ζ_{rot} - The new section stagger angles were calculated in the following way. The blade mean line angle (at the inducer leading edge) was deduced using the potential flow air angles and the i_m incidence distribution from Figure 20. The change in blade mean line angle (between present design and the progenitor fan) was then added to the fan rotating stagger angle to produce the inducer rotating stagger angle. Implicit in this is that the blade sections are re-staggered about the leading edge. The relevant formula is:

$$\gamma_{rot} = \gamma_{rot\ fan} + \Delta\beta_b$$

where:

$$\Delta\beta_b = \beta_b - \beta_{b\ fan}$$

with $\beta_b = \beta + i_{m\ fan}$

The airfoil shape derived by these design methods was used to define the inducer blade at 100% design speed. A radial element inducer design was used and this will prohibit deformation of the inducer blades between static and rotating conditions. Therefore the ζ_{rot} values can be used to specify the manufacturing coordinates of the blades.

Blade layout - The blade profiles (for each section) for the present design were generated from the above information in the following way.

The scaled blade profiles were set at the calculated ζ_{rot} angle to lay out two suction surface profiles spaced one blade pitch s apart.

The locus of A_{min} values was then laid off from the suction surface toward the leading edge of the "trailing" blade contour (see the sketch below).

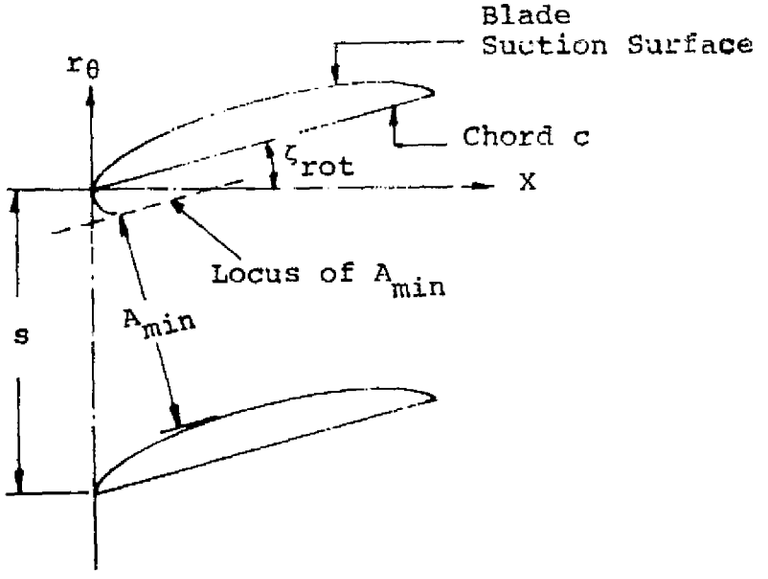

The leading edge of the blade was constructed by joining the existing suction surface with a pressure surface contour at the leading edge satisfying the A_{min} criteria. This specifies the leading edge normal thickness.

Furthermore, the nominal blade mean line pressure and suction surface locations are known for each section and hence may be laid out. This information is available because the blade setting angle and blade thickness distributions are prescribed together with the requirement that radial elements exist in the inducer.

The final blade suction surface profile was generated by blending from this prescribed suction surface into the original fan blade profile. The location of this "blend" point (tangent point) was carefully controlled near the tip regions of the blade where transonic performance will be obtained. The A_{min} location is approximately where the bow shock from the leading edge will strike the suction surface in transonic supersonic flow. ($M_{rel\ approach} > 1$) or where λ shocks will terminate on the suction surface, from imbedded supersonic regions, in transonic subsonic flow ($M_{rel\ approach} < 1$). It was therefore important to keep the blend point well downstream of the A_{min} location.

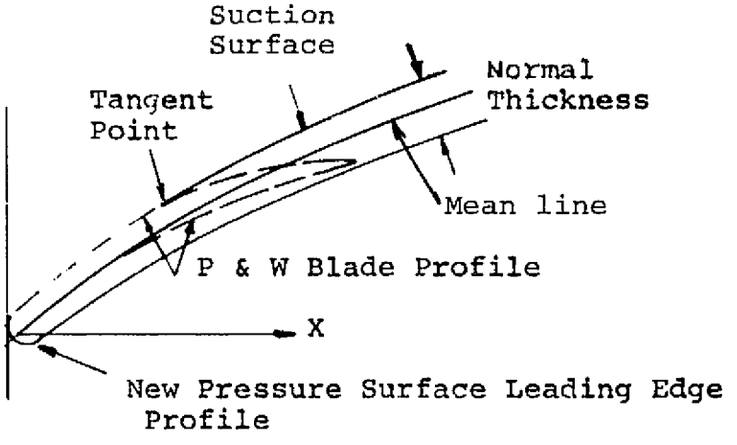

Finally, the remaining pressure-surface contour was generated from the leading edge portion defined above to meet the specified blade pressure surface contour. Usually, this presents no great problem as a smooth contour can be so joined.

For blade sections close to the hub, it is more difficult to match the suction surface contours of a radial element inducer blade to the original fan profiles except close to the leading edge. This is because the fan blade is not a radial element blade and has significant turning toward (or beyond) axial in the hub sections. Nevertheless, it was possible to maintain the A_{min} criteria for all section profiles. Furthermore, it is probably not critical to hold the exact blade profiles close to the hub since these are low Mach number blade sections.

The final blade shape was obtained by laying out radial plane sections (sections normal to the rotor axis) of the blade and smoothly joining the pressure/suction surfaces through the original fan sections laid out as above. Some iteration is required to smooth out small irregularities that appeared in the radial plane profiles. This was accomplished by slightly "shifting" some of the cylindrical section profiles.

AERODYNAMIC DESIGN OF IMPELLER

Approach

The aim of the impeller design was to generate the geometric details of the impeller blades and the hub and cover meridional contours within the geometric constraints determined in the Preliminary Design Phase for the $\beta_{2b} = -30°$ case. The inducer design actually forms part of the impeller design and is faired into the impeller form in the approach used here.

The basic criterion used for the impeller design is to ensure that certain aerodynamic features are achieved that will yield the tip conditions set in the Preliminary Design Phase (PDP). At the same time the blade loading distribution must be controlled. These aerodynamic features are influenced in some complex manner by the required geometrical quantities, i.e. the hub and cover meridional contours, the thickness distribution of the blades and the blade setting angle distribution. It is impossible to study all geometric combinations of these variables. Therefore, certain geometric features (e.g. thickness distribution) are prescribed and maintained, while other features are altered to meet the aerodynamic criteria. Inevitably, a measure of arbitrariness enters the design when these fixed geometric features are prescribed.

The available geometric choices may be limited by questions of impeller stresses, blade and impeller deflections, impeller inertia, blade vibrational modes and instrumentation constraints (such as have been impressed upon this design by the use of LDV instrumentation). The aerodynamic criteria should be achieved within these constraints. This may lead to some compromises being made in the aerodynamic criteria or even in the basic specifications.

For the present design, the use of LDV instrumentation played a major role in the design as discussed fully in the Introduction. The impact of the LDV constraints on selection of a minimum impeller tip depth and the no-splitter requirement had already been considered in the Preliminary Design phase, as had the requirement for a constant inducer cover radius. As it transpired, these restrictions did not appear to prevent the attainment of the aerodynamic criteria.

The only methods presently available for the calculation of flow in the impeller are those assuming potential flow. The Creare flow model dictates that the flow in most of the impeller consists of an isentropic jet which, however, may separate. The separated jet will then have a constant Mach number on its separated face and a wake region (most likely of increasing area) growing towards the tip. The potential flow solution must reflect this flow model.

The remainder of this chapter contains a discussion of the potential flow program and the aerodynamic criteria to be used. The results of the calculations are then presented, together with the definitions of all the relevant geometry for the impeller.

VANCO Potential Flow Program

The potential flow program used is a version of the calculation procedure of Vanco (Reference 8), who extended the basic program of Katsanis (Reference 9) to deal with centrifugal compressor flows. Briefly, the program solves the velocity-gradient equation with the assumption of a hub-to-cover mean stream surface along arbitrary quasi-orthogonals (i.e., lines which intersect each streamline once only) in the meridional plane. The velocity-gradient equation is Euler's equation transformed to a coordinate system fixed to the mean stream surface. The latter is the two-dimensional stream surface running up the middle of a blade channel and extending from hub to cover. For the VANCO program, the quasi-orthogonals must be lines of constant θ extending from hub to cover (they lie in the meridional plane by definition of θ = constant). The use of quasi-orthogonals has a clear advantage over methods which employ normals to streamlines in that they remain fixed straight lines regardless of any streamline form change. Having found the mean-stream-surface relative velocities, velocities on the pressure and suction surface are found using the rapid approximate method of Stanitz and Prian (Reference 10).

The basic inputs to the program, other than the obvious ones of mass flow, rotational speed, number of blades, etc., are the end point coordinates of the quasi-orthogonals with the associated wrap angles (θ) and the blade-normal thickness at hub and cover. The program linearly interpolates along the quasi-orthogonals to find the normal thickness at intermediate points. In fact, any normal thickness distribution may be input;

the linear distribution was chosen as being convenient. Since the quasi-orthogonals are fixed straight lines, the mean blade shape is completely defined by specifying wrap θ as a function of meridional distance m for the hub and cover streamlines. Furthermore, the pressure and suction surfaces are defined since the normal thickness is specified. The actual blade geometry for the present design will be defined in the above manner, i.e., in the "VANCO implied" way.

Further important inputs to the program are the exit flow angle (set equal to the jet angle) and the possibility of including losses by means of a distribution of loss of relative total pressure with meridional distance.

Modifications to Reflect Creare Flow Model

The VANCO program cannot be used with the usual input if it is to reflect the Creare flow model of an isentropic jet flow and a growing wake region. However, the basic physics of this model can be represented approximately by an appropriate change in the values of the normal input quantities as outlined below.

For the present design, a fairly simple and traditional approach was taken. No experimental evidence is available that indicates how the wake region grows within the blade passages of the centrifugal impeller. Therefore, recourse must be made to a cruder representation. For the present design, this entailed iterating boundary layer calculations with the potential flow calculations and then treating the boundary layer displacement thickness as wake flow by taking it as additional blade blockage.

Aerodynamic Criteria

The aim of the aerodynamic criteria is to ensure, insofar as possible, that the Preliminary Design Phase (PDP) tip conditions are matched. These rules are:

1) Achieve the PDP target impeller tip diffusion ratio (DR_2).

2) Limit the diffusion to no more than 50% in the inducer (i.e., near-axial portion of the impeller).

3) Limit the diffusion to no more than 15% futher diffusion in the "radial" portion of the impeller.

4) Ensure that, if separation does occur, it does so two-dimensionally.

Recall that the traditional Creare flow model with the assumption of a constant relative Mach number along the jet face, starting at the jet/wake separation location, means $DR_2 < DR_{sep}$. Clearly maximizing DR_{sep} implies that DR_2 is maximized. The former was the intent of the Preliminary Design Phase and so presumably Rule 1 is already accomplished, assuming that the remaining three rules are satisfied.

The other rules seek either to ensure that separation occurs along a two-dimensional line between hub and cover suction surface or to eliminate separation altogether. Rule 2 suggests that no more than 50% diffusion be allowed in the inducer portion of the impeller or else the turbulent boundary layers will separate there. This separation cannot be accomplished two-dimensionally because the hub M_{rel} is far too low. The separation line should be a line of constant M_{rel} for steady internal flow.

Some recent work (Ref. 13) has shown that fully developed turbulent boundary layers in rotating channels may become "stabilized" when a critical rotation number ($\ell\Omega/W$) is exceeded. "Stabilize" means the boundary layers take on a laminar character and it is postulated that no more than 15% diffusion may be applied before separation occurs. Actually separation is allowable in the radial portion because this can usually be done two-dimensionally. However, such a separation will be acceptable only if the separation Mach number (on suction surface) matches the target tip value from the Preliminary Design Phase.

The most critical stream tube affecting the flow in the impeller is the one along the blade suction surface at the cover. When the above rules are applied to this stream tube, the loading distribution suggested is that of a rapid diffusion in the inducer or axial portion, followed by a gradual diffusion in the radial portion. At the same time, the rules are applied to the

hub suction surface, so that no more than 50% diffusion should occur in the axial portion of the hub stream tube. Hub separation, should it occur, will tend to raise the cover suction surface relative velocity because of blockage of the separation bubble, making it more difficult for the flow on this latter surface to reach the target M_{rel} within the 15% radial diffusion constraint.

The potential flow calculations for the pressure surfaces will show higher diffusion rates than for the suction surfaces, indicating the possibility of separation on these surfaces. However, this will probably not occur since the pressure surface boundary layers are vigorously stirred in the radial portion of the wheel by the action of Coriolis forces, which remove low energy boundary layer fluid created on the blade driving surface. In the axial part of the impeller the driving mechanism is the large blade-to-blade loading.

Another important constraint is that no "potential flow reversal" should occur. This is most likely to occur upon the hub pressure surface. Reverse flow at the hub has the effect (because of its pseudo blockage effect) of accelerating the flow on the suction surface. For these reasons, rapid deceleration at the hub, if any, should be delayed as far as possible toward the impeller exit.

Creare's ideal loading distribution is indicated in Figure 21. For the present design, an attempt was made to match this loading distribution and to meet the target $M_{rel\ 2j}$ at the same time. If possible, the target $M_{rel\ 2j}$ is to be met without separation occurring. If separation does occur, it should occur two-dimensionally. As may be seen, this can only be accomplished near the impeller exit if the ideal loading distributions are to be followed.

These criteria were used in the present design. However, they were impacted by the mechanical constraints of hub and blade stress limitations and by the desire to have a constant radius at the inducer shroud where the LDV window is located. A low number of blades at impeller exit (i.e. no splitters) was desired for the LDV studies.

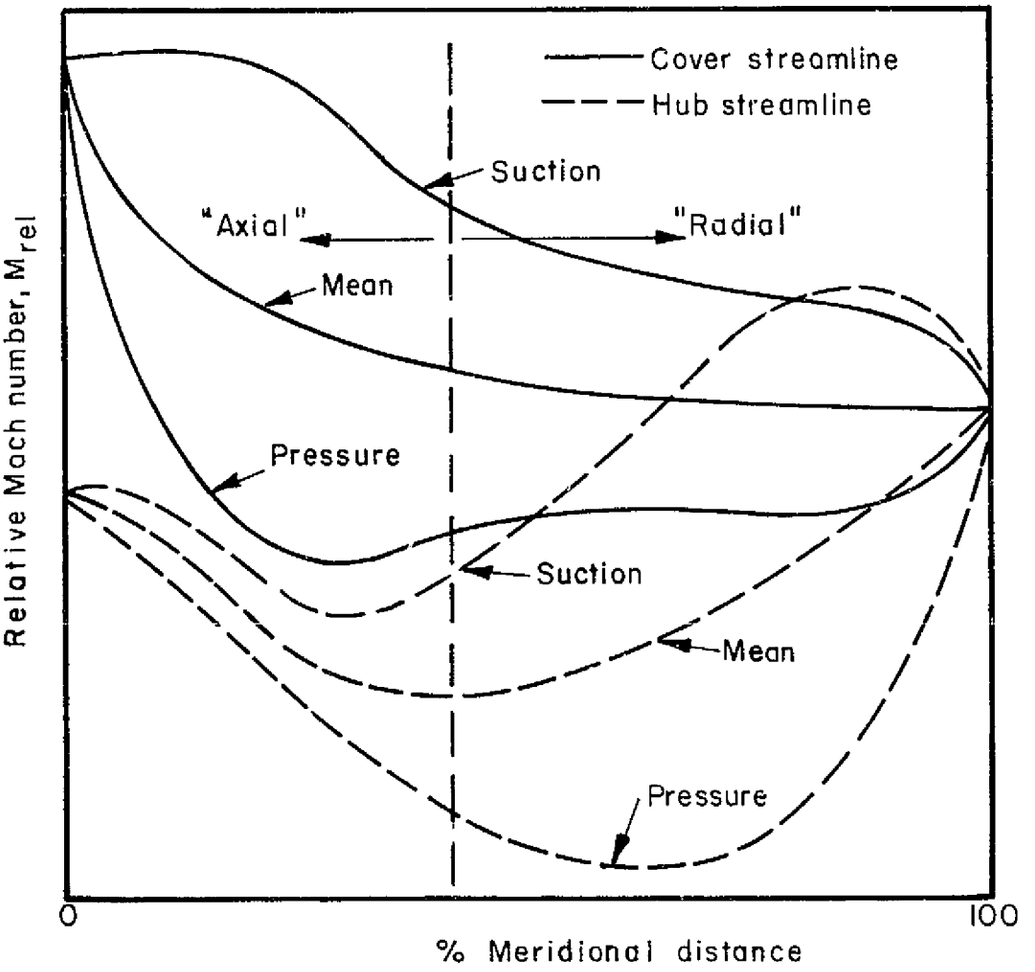

Figure 21—Creare's Ideal Impeller Loading Distribution

Results

The above general approach was applied to the design of the present impeller. The geometric constraints, already fixed in the Preliminary Design Phase, are the inducer leading-edge hub and cover radii (r_{1h} and r_{1t}), impeller tip radius, depth and blade angle (r_2, b_2 and β_{b2}) and a constant inducer cover radius deep into the impeller (LDV constraint).

Within the above constraints, the following geometric features must be chosen:

i) the hub and cover meridional contours,

ii) the hub and cover blade setting angle (β_{bh} and β_{bs}) distributions, and

iii) the hub and cover normal blade thickness distributions.

Initiation - The above items were set initially in the following way. The cover in the inducer portion was set at constant radius (i.e., r_{1t}) in order to eliminate the need for a curved inducer LDV window. The hub contour was made a 7° ramp in order to satisfy (approximately) continuity at the end of the inducer. The remaining part of the contours (both hub and cover to the tip) were generated using a simple continuity check.

The cover β distribution was set by drawing a smooth curve from the known tip value of -30° (β_{2b}) to blend into the previously prescribed inducer (β_b) distribution. In the inducer section, the hub β_b distribution follows from the radial element assumption, while the rest is generated by drawing a smooth curve between the inducer portion and the tip value of -30°.

The blade normal thickness along the cover was set in the inducer portion by laying out the tip inducer section and then using a constant blade thickness distribution for the remainder of the blade. The blade normal thickness distribution along the hub was initially chosen "arbitrarily" with a peak value (chosen by intuition) at the position likely to have the highest stress value, followed by a fall-off in thickness.

Iteration - The basic procedure was to vary the shape of the meridional contours and the β_b distributions in attempting to match the ideal loading distribution (see Figure 21). The normal thickness distributions remained essentially fixed. The hub normal thickness was changed slightly to alleviate stress problems as these stresses were calculated. The final blade normal thickness distributions at hub and cover are shown in Figure 22.

The blade turning distribution (β_b) has a strong effect on the loading distribution in the axial part of the impeller (i.e., inducer region and slightly beyond), but less so in the radial portion where centrifugal and Coriolis effects largely determine the loading. Consequently, the β_b distribution in the latter half of the inducer portion (on the cover side from Z = 0.89 cm to about approximately Z = 3.3 cm) is varied in conjunction with the meridional contours to produce the required cover suction surface loading distribution. Recall that the β_b distribution in the first portion of the inducer is determined by the fan scaling (see Inducer Section).

The rest of the β_b distribution is developed by laying out a smooth curve from the tip value (-30°) to blend into the desired β_b distribution (indicated above) just beyond the end of the inducer. This curve is not drawn completely arbitrarily in that it is necessary to keep the β_b's and hence the blade tip wrap θ_2 as low as possible in order to minimize blade stress. The hub β_b distribution is largely determined by the cover β_b's because:

1) radial elements are required in the inducer portion,

2) zero rake angle (θ plane) at the tip is prescribed. This means that the hub blade wrap angle $(\theta_2 - \theta_1)_h$ must be equal to the cover blade wrap angle $(\theta_2 - \theta_1)_c$.

The final blade β_b distributions at cover and hub are shown in Figure 23.

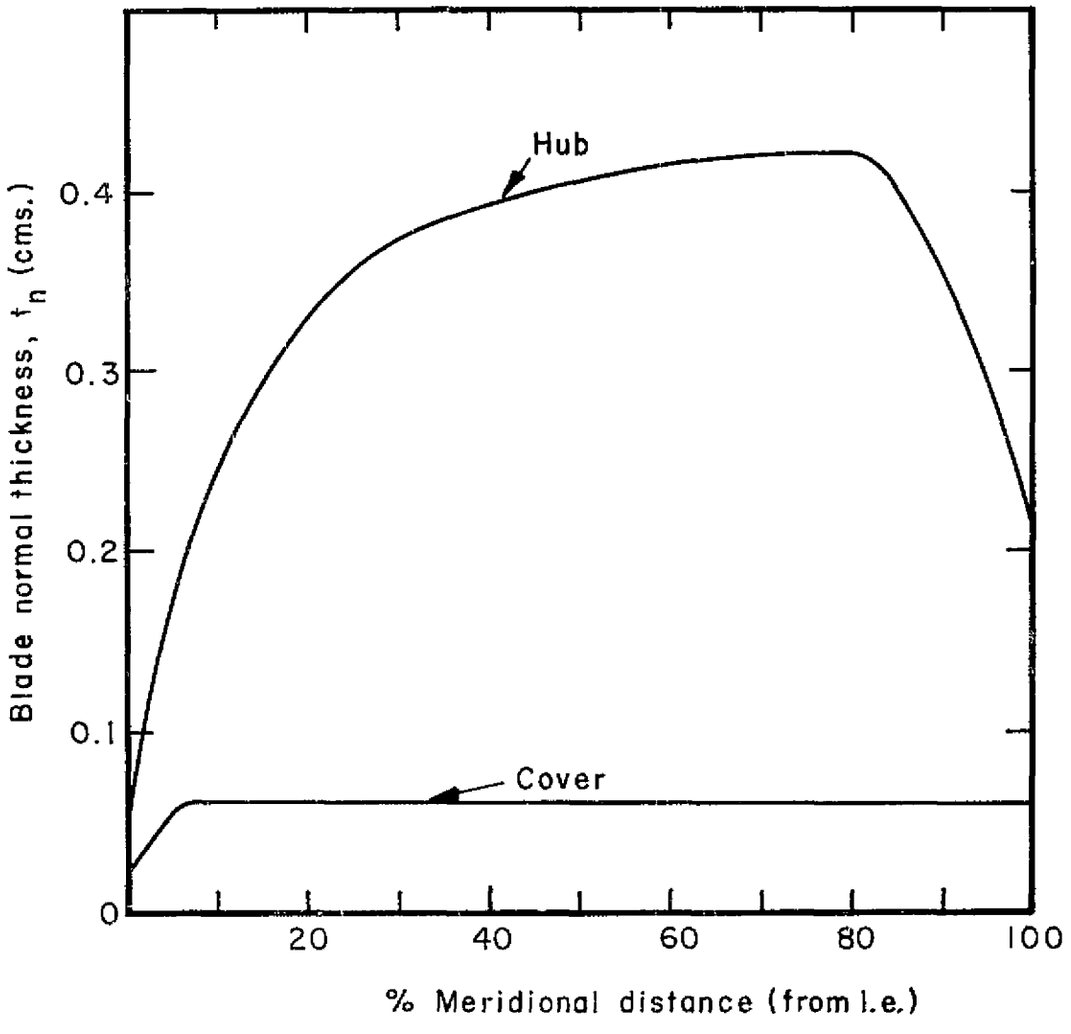

Figure 22 — Blade Normal Thickness Distribution — Hub and Cover

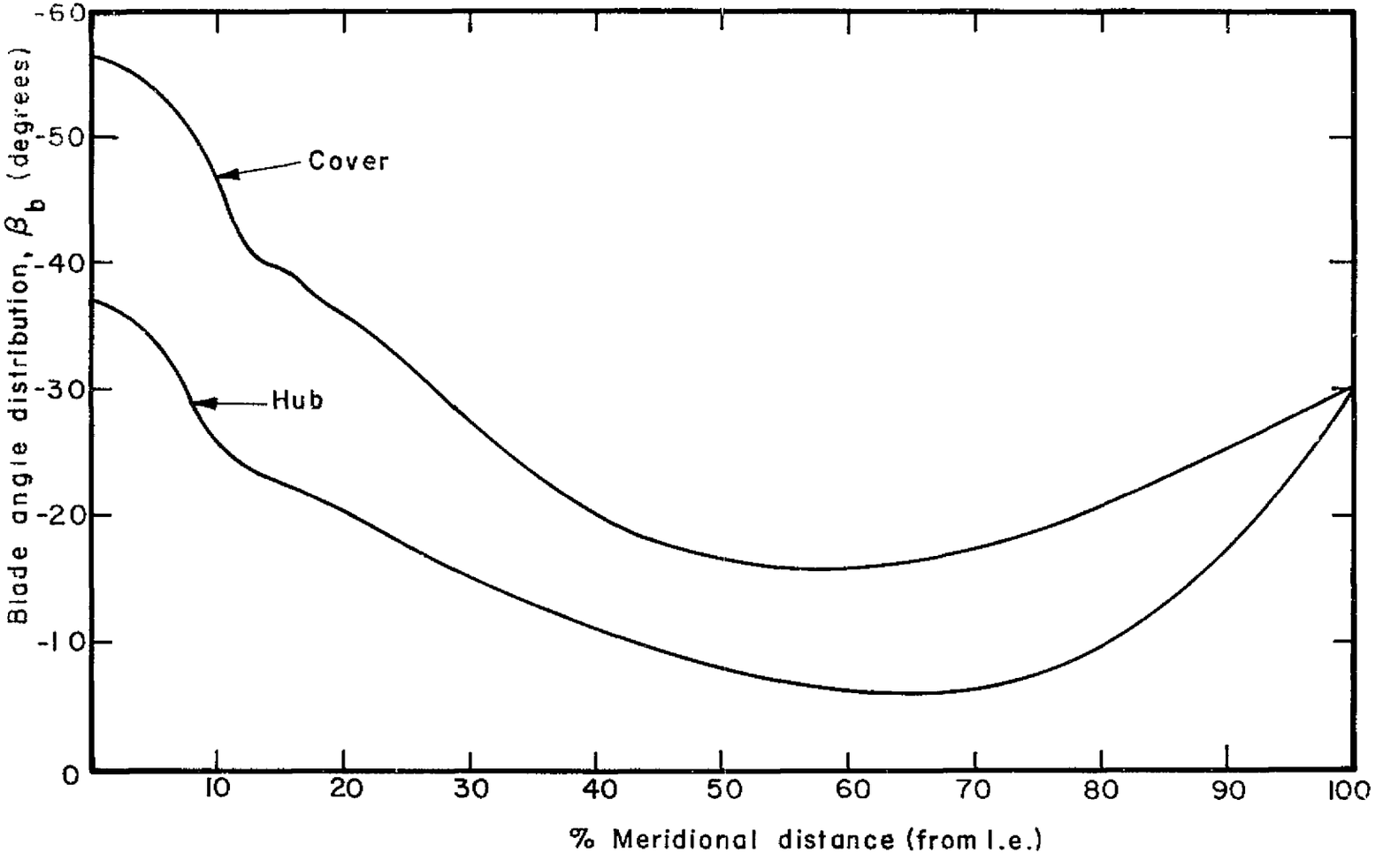

Figure 23 — Blade Angle Distribution— Hub and Cover

The meridional contours (particularly the cover contour) have a large effect on the mean and blade surface velocities. The principal effect is in the regions beyond the inducer because of the significant curvatures there. (This will be especially true in a low inertia impeller.) Initially, a reacceleration on the cover suction surface was encountered just beyond the inducer end. This was eliminated by increasing the impeller length, thereby decreasing the curvatures. Recall that the cover contour was constrained by the requirement of constant radius in the inducer section. The hub meridional contour is largely determined once the cover one is set because:

i) the tip radius and depth (r_2, b_2) are known, and

ii) the hub ramp angle and length are given.

Boundary layer calculations - Boundary layer calculations were carried out for the cover and blade suction surfaces using a boundary layer prediction technique based upon the methods developed by Englert (Reference 11). The input for these calculations came from the potential flow results. The assumption was made that the boundary layer growth throughout the impeller is typical of that calculated for the blade suction surfaces. The action of Coriolis forces is to sweep excess boundary layer fluid created on the blade driving (pressure) surfaces toward the suction surface near the exit of the impeller.

Final results - As well as iterating the geometrical quantities indicated above in attempting to reach the ideal loading distribution, the potential flow calculations were iterated with the boundary layer calculations. This was accomplished in the traditional manner of calculating the potential flow without boundary layers as a first step, then calculating the boundary layers as indicated above and re-doing the potential flow calculations by including the boundary displacement thickness as extra blade blockage. Only one loop of this iteration was performed.

The final results are displayed in Figures 24 to 31. Figures 24 through 29 show the relative Mach number and relative velocity distributions as calculated for the impeller flow. Distributions are shown as a function of impeller meridional distance for the cover streamline (streamline 13), for the approximately mid-span streamline (streamline 7), and the hub

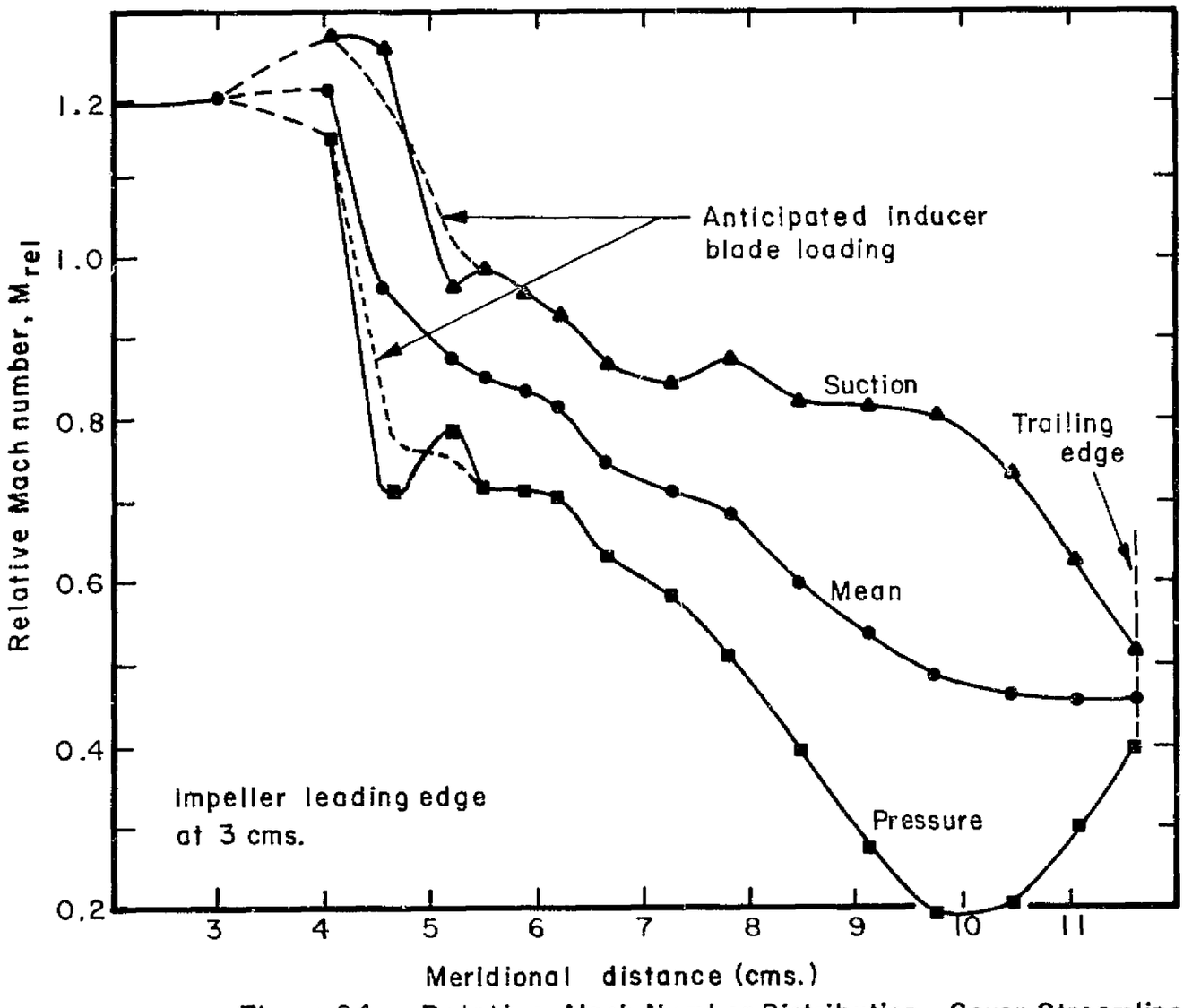

Figure 24 — Relative Mach Number Distribution—Cover Streamline

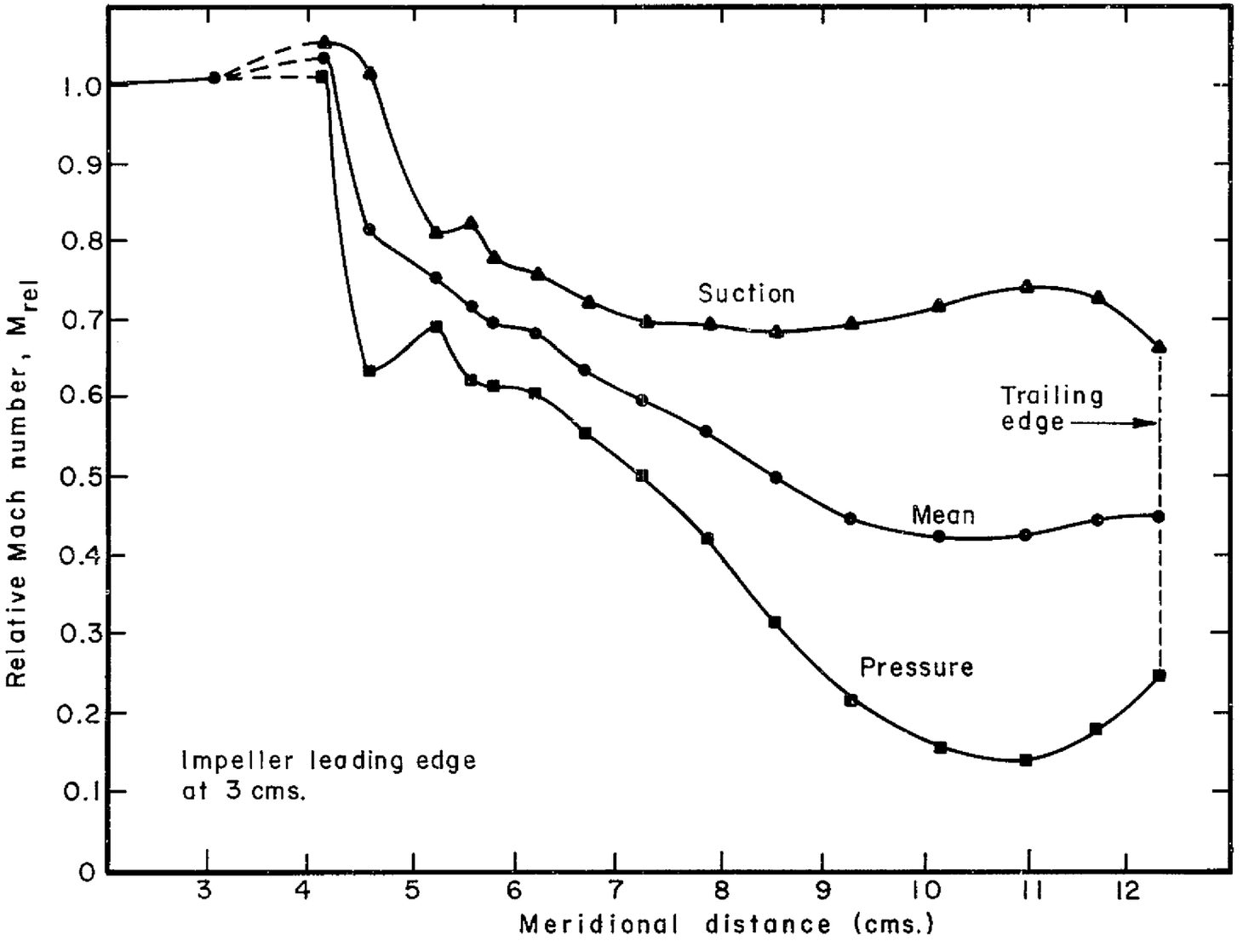

Figure 25 – Relative Mach Number Distribution – Mean Span Streamline

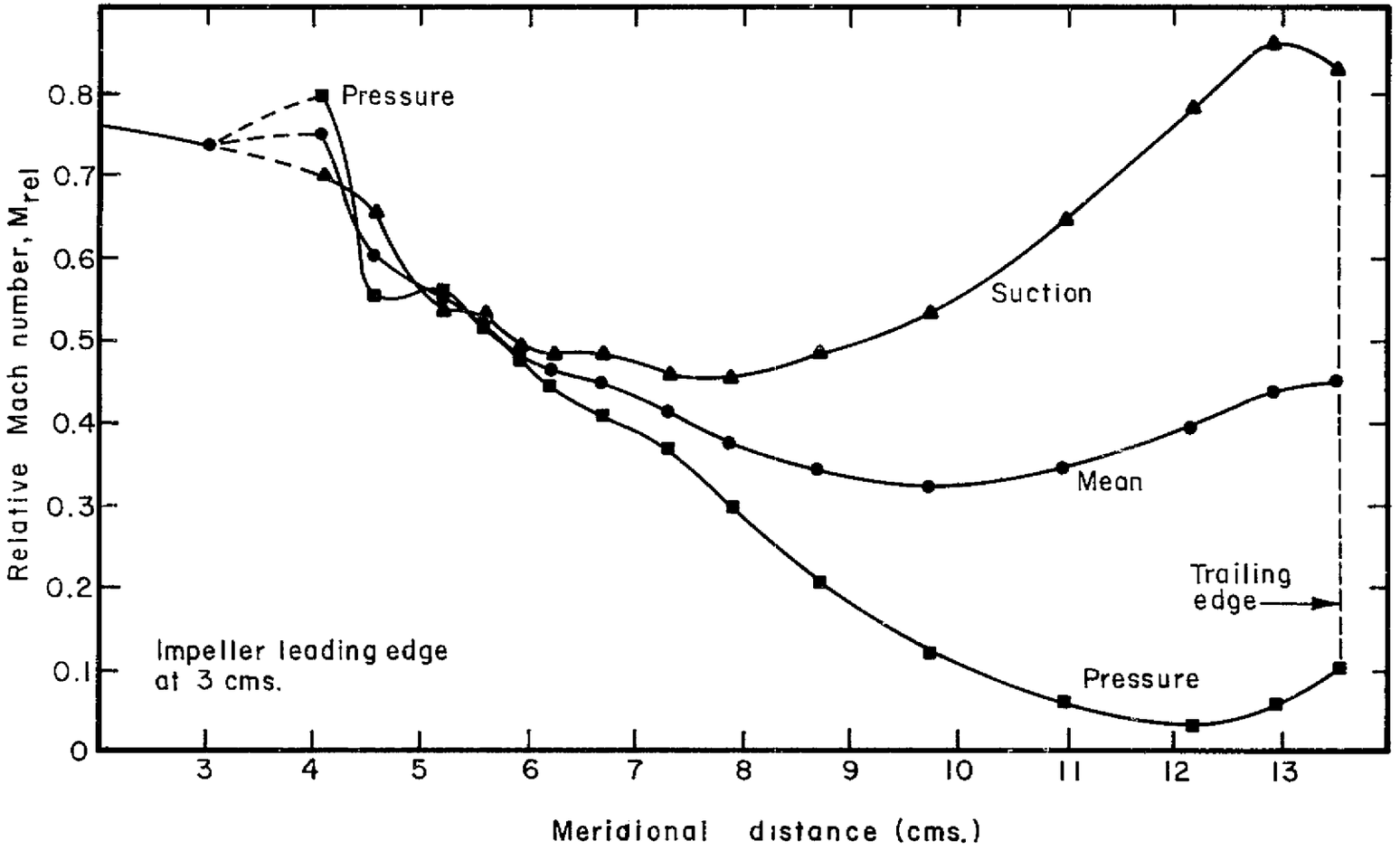

Figure 26 – Relative Mach Number Distribution — Hub Streamline

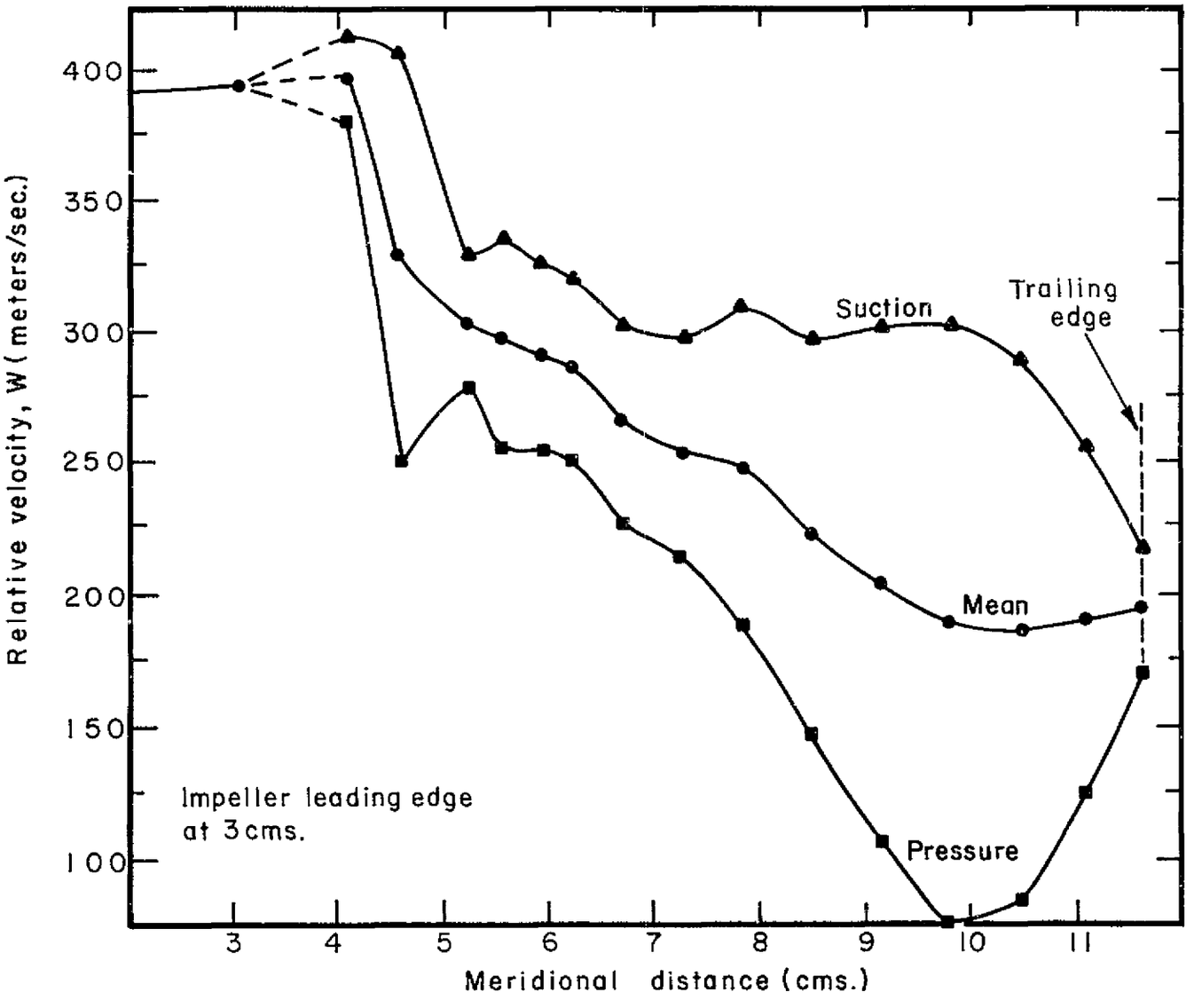

Figure 27 – Relative Velocity Distribution – Cover Streamline

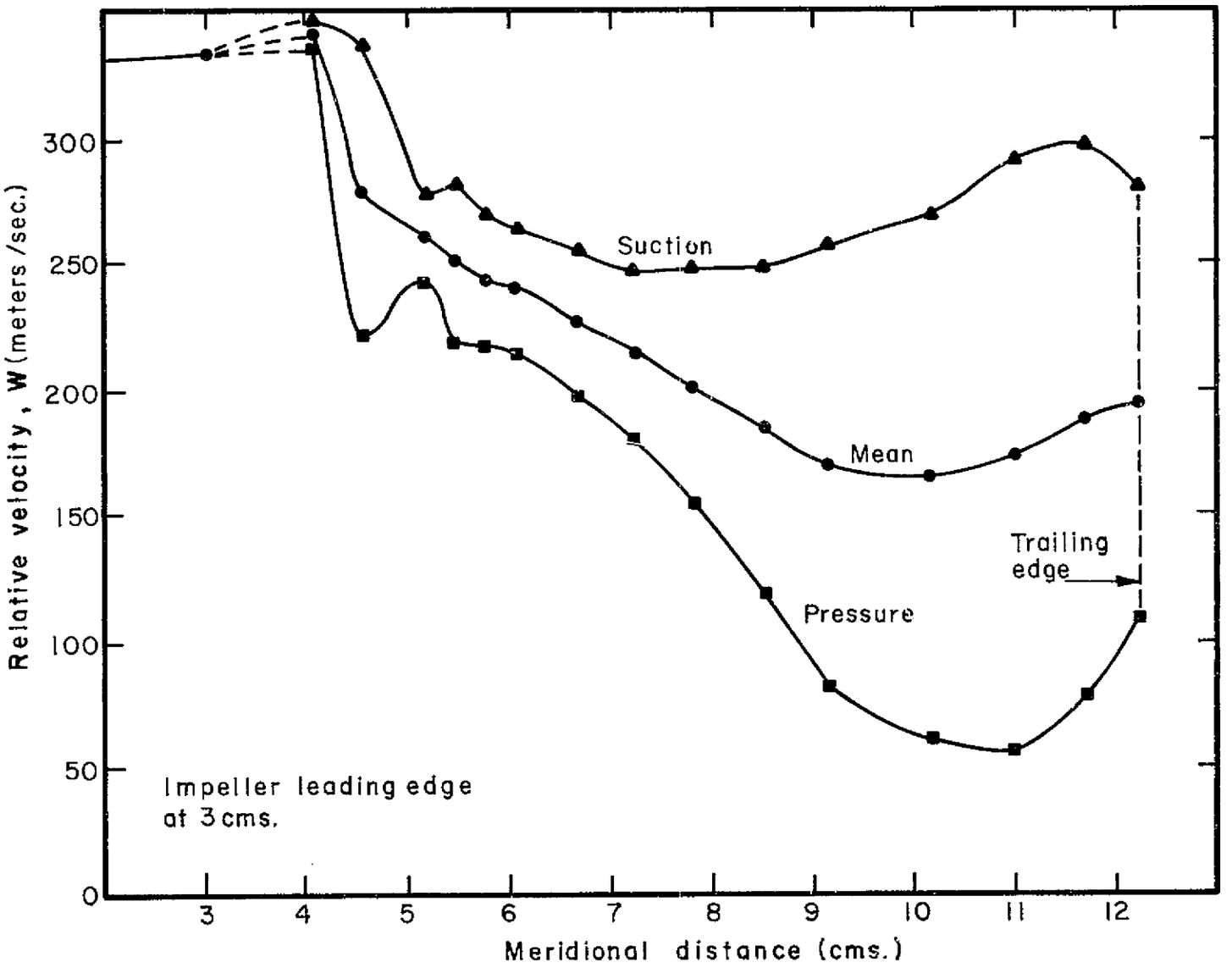

Figure 28 – Relative Velocity Distribution – Mean Span Streamline

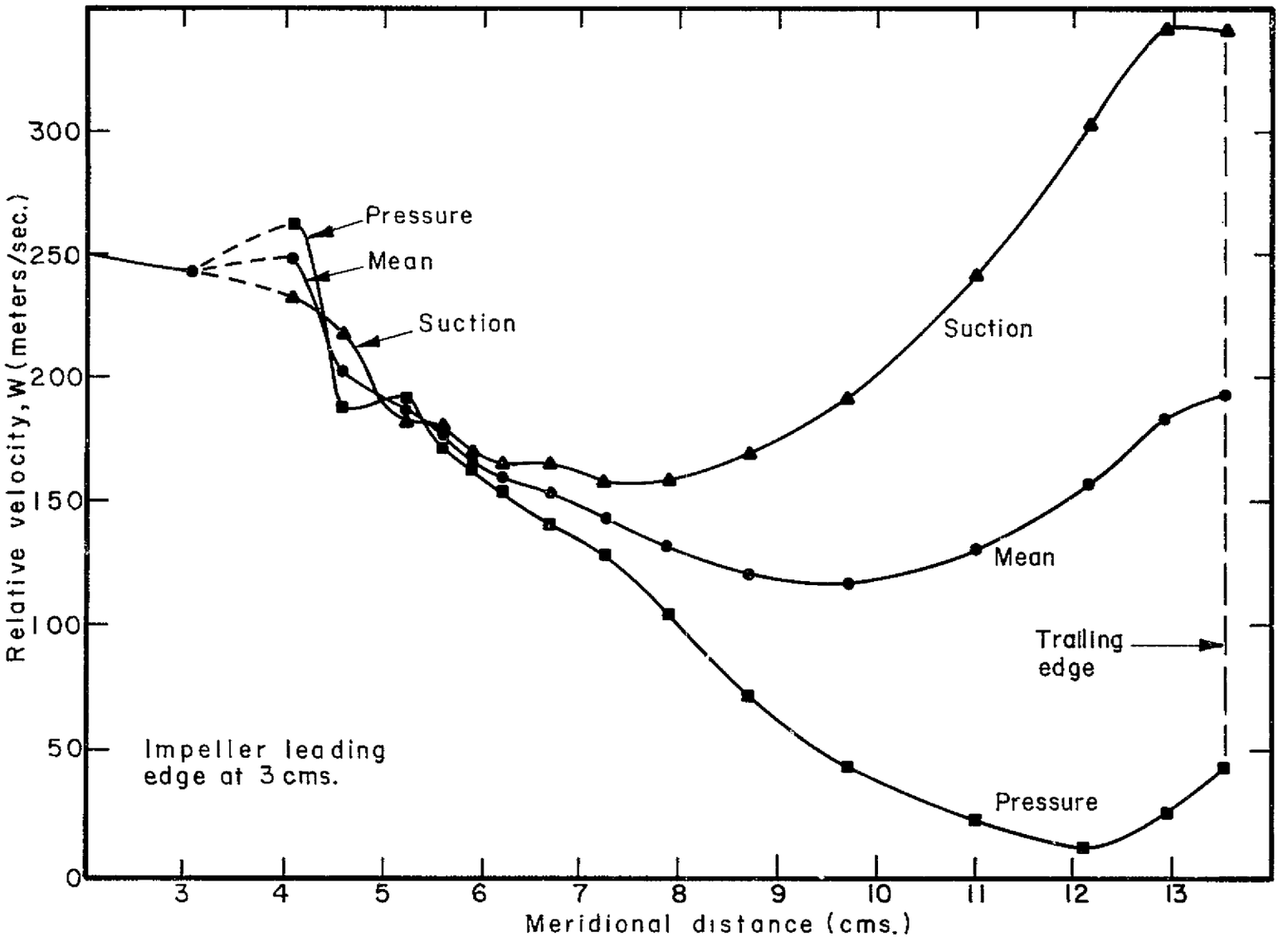

Figure 29 — Relative Velocity Distribution — Hub Streamline

streamline (streamline 1). For each streamline, the data is displayed for the suction (trailing) blade surface, the pressure (leading) blade surface, and for the flow passage mean streamline.

The calculations are shown "dashed" immediately at the entrance to the impeller, since the calculated results are not expected to be correct in the leading edge portion of the inducer blades.

A rapid diffusion occurs in the axial inducer, followed by the more gradual diffusion in the radial portion of the impeller. In these figures, the cover and mid-span plots show an initial, large "loading" in the inducer and then a reduced loading until the loading is again increased in the radial portion of the impeller. Actually, the loading is expected to be more uniform, e.g., as shown in Figure 24; the spline fit routines used in the calculations are incapable of accurately following the details of the blade β distributions in this region. Thus, the ideal loading distribution (Figure 21) was matched reasonably well for the hub streamline, but the cover streamline exhibits too much loading in the radial part of the impeller. The use of splitters would have prevented the latter.

Separation is expected to occur on the cover suction surface near the exit of the impeller at the target separation relative Mach number of 0.792. The flow is assumed to establish a separation line across the blade span at this Mach number and to flow at constant jet Mach number to the impeller exit.

There is a significant divergence between the actual and ideal loading near the impeller tip. However, the actual loading, velocity, and Mach number distribitions at and near the impeller exit are probably not correct because (1) the flow is expected to separate within the impeller as discussed above, and (2) the blade loading calculation routine calculates loading at the impeller exit where none will exist and the routine is "sensitive" to rapid changes in flow blockage (such as exists near the impeller exit when the boundary layer displacement thickness is included).

Figures 30 and 31 show the cover and hub blade boundary layer displacement thickness and shape factor H ($\equiv \delta^*/\theta$) distributions. These distributions have been used for both pressure and suction surfaces in setting the effective boundary layer blockage distribution used in the potential flow calculations. A linear distribution

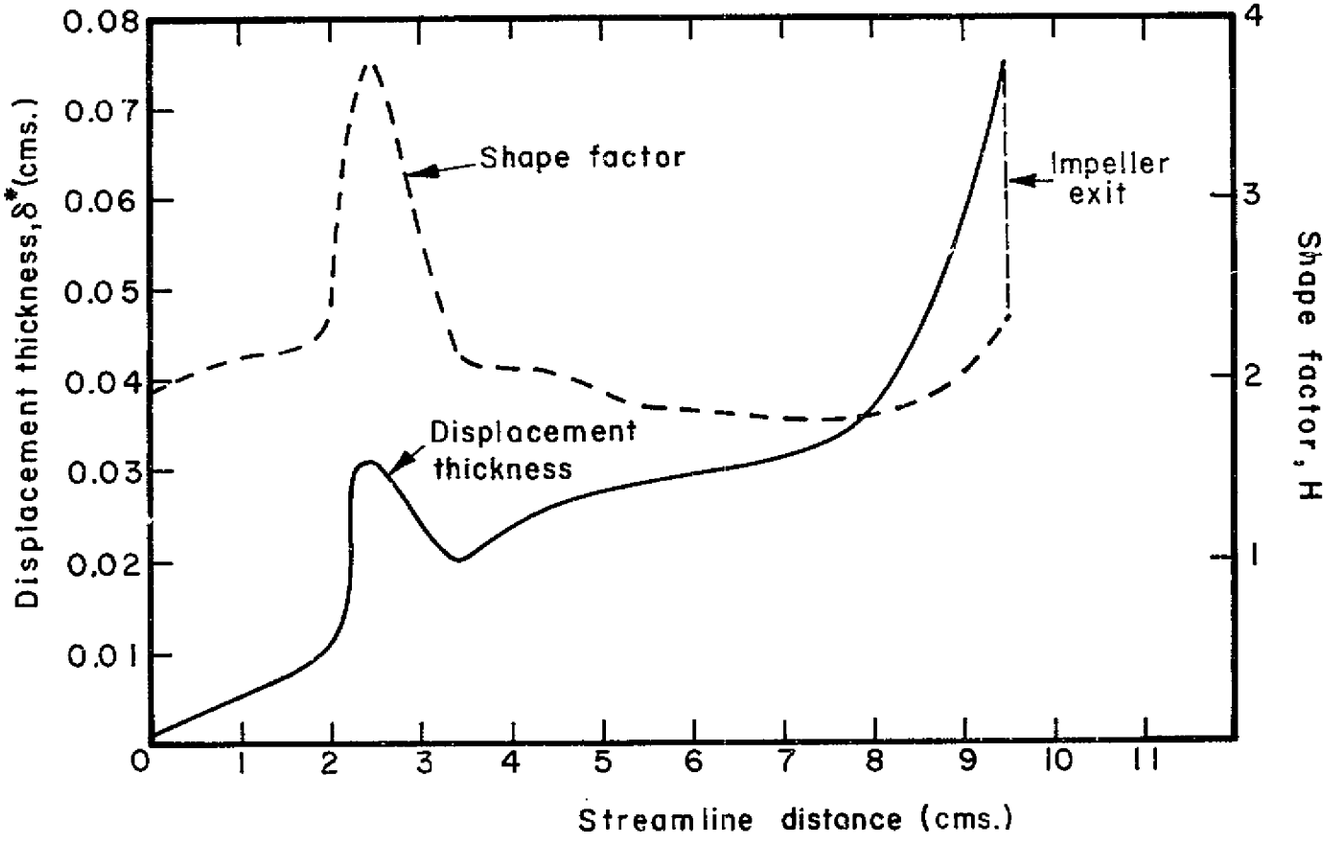

Figure 30— Boundary Layer Characteristics for Blade Suction Surface — Cover Streamline

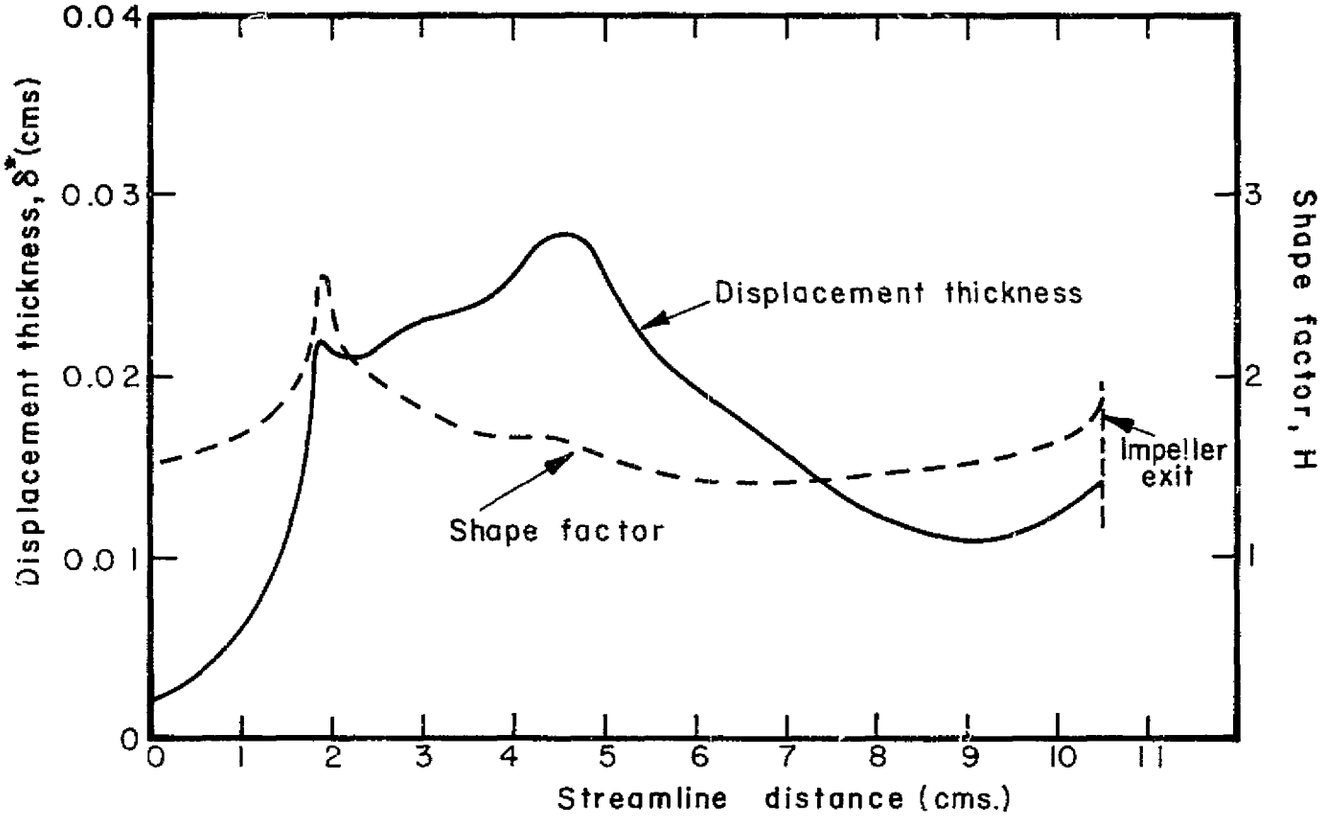

Figure 31 — Boundary Layer Characteristics for Blade Suction Surface — Hub Streamline

between hub and cover values was used across the blade span. Figure 30 shows a rapid increase and decrease in boundary layer characteristics in the middle of the inducer on the cover streamline. The shape factor far exceeds traditional boundary layer separation values (of order 2.7). However, as indicated above, the rate of change of blade angle (and hence diffusion rate) will be less than calculated and, hence it is anticipated that separation will not occur in the inducer.

Final Blade and Passage Definition

"Nominal" hub and cover meridional contours are defined corresponding to the above calculations. Additional calculations must be made before the final coordinates for the cover, the blade tip, and the hub contours are defined. The coordinates for the "nominal" hub and cover meridional contours are given in Table VI together with the blade definition (β, t_n) at the same points.

Turbulent boundary layer calculations were carried out for the surfaces of the compressor inlet (both hub and cover) using the Englert (Ref. 11) method (see below for the inlet contour definition). These calculations indicated approximately the same displacement thickness at the inducer leading edge for both the outer and inner inlet contours. The boundary layer blockage effect must be considered in defining the cover and hub meridional contours.

Cover contour - The final cover contour was constructed very simply by using the nominal cover contour as a base. A smooth contour was constructed from a point displaced radially 0.025 cm at the inducer leading edge to blend into the nominal cover contour just beyond the end of the inducer. This curve defines the final cover contour.

The blade tip contour is defined simply by specifying a clearance distribution with respect to the final cover contour as defined above. A 0.025 cm running clearance normal to the above meridional contour was used from impeller inlet to exit. This represents a clearance of approximately 8% of the impeller tip exit depth.

Hub contour - The actual hub contour was constructed by reducing the leading edge radius by 0.023 cm (to allow for boundary layer blockage) and putting in a ramp angle of slightly more than 7° to blend into the nominal hub contour just beyond the inducer end. Figure 32 shows the impeller meridional view.

Blade geometry - For the inducer portion of the impeller, the blading was developed by scaling the P & W fan blading as stated in the Inducer Section.

TABLE VI - NOMINAL IMPELLER GEOMETRIC COORDINATES[1]

Quasi-Orthogonal Number	Blade Angle, β (degrees)		Axial Distance, x (cms)		Radial Distance, r (cms)		Angular Location, θ (degrees)	Normal Thickness, t_n (cms)	
	cover	hub	cover	hub	cover	hub		cover	hub
4 (inlet)	-56.34	-36.70	0.	0.	4.3716	2.1858	0.	0.0152	0.0305
5	-54.24	-35.33	0.5080	0.5080	4.3716	2.2482	-9.2537	0.0610	0.1829
6	-43.33	-26.33	1.0160	1.0160	4.3716	2.3105	-16.9675	0.0610	0.2489
7	-37.18	-22.36	1.6510	1.6510	4.3716	2.3885	-24.0015	0.0610	0.3048
8	-30.25	-19.56	2.1755	2.1538	4.3859	2.4603	-28.6043	0.0610	0.3401
9	-24.78	-17.33	2.6708	2.5853	4.4294	2.5440	-31.9627	0.0610	0.3602
10	-19.94	-14.94	3.2841	3.0812	4.5345	2.6691	-35.2184	0.0610	0.3759
11	-17.21	-12.97	3.8417	3.5220	4.6954	2.8124	-37.6289	0.0610	0.3833
12	-16.03	-11.21	4.3413	3.9443	4.9142	2.9855	-39.5633	0.0610	0.3912
13	-16.11	- 9.06	4.8808	4.5064	5.2727	3.2892	-41.6539	0.0610	0.4013
14	-17.14	- 7.24	5.2419	5.0461	5.6300	3.6971	-43.2458	0.0610	0.4094
15	-18.40	- 5.99	5.4701	5.5383	5.9407	4.2394	-44.4685	0.0610	0.4163
16	-20.06	- 6.76	5.6607	6.0262	6.2889	5.1405	-45.7654	0.0610	0.4191
17	-22.13	-10.10	5.8128	6.2802	6.6756	6.1284	-47.1816	0.0610	0.4155
18	-25.55	-18.85	5.9541	6.3500	7.2527	7.1275	-49.3400	0.0610	0.3353
19	-30.00	-30.00	6.0262	6.3500	7.9756	7.9756	-52.2312	0.0610	0.2032

[1]Before correction on hub and shroud for inlet boundary layer growth.

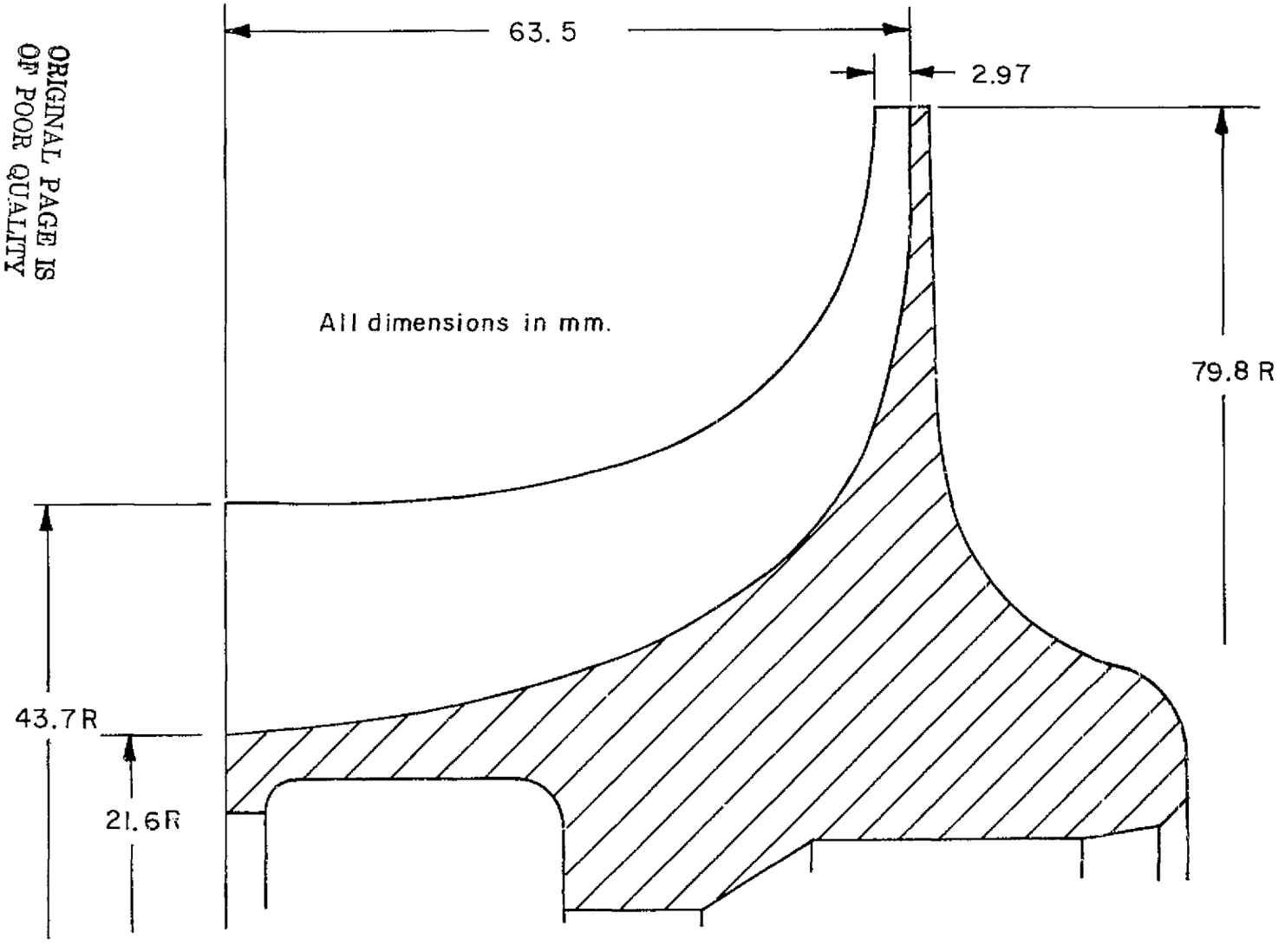

Figure 32- Meridional View of Impeller

The blading for the remainder of the impeller was developed in the "VANCO implied" way. Thus, radial plane cuts were passed through innumerable quasi-orthogonals (constant θ lines), which define the mean line of the blades. The pressure and suction surfaces were then developed assuming a linear distribution in normal thickness along the quasi-orthogonals with a linear blade angle distribution along the radial plane cuts. Some smoothing of the blade contours was done by iterating between tangential plane cuts and the radial plane cuts.

Inlet Design

As stated above, boundary layer calculations showed approximately a 0.025 cm boundary displacement thickness on the outer and inner inlet contours at the inducer leading edge. This represents an inlet area blockage of approximately 2.25% based on flow area at the impeller inlet. This blockage was taken into account in defining the inlet contours shown in Figure 33. The final inlet configuration uses long radius ellipses on both the inlet "bellmouth" outer contour and the inner centerbody contour. The centerbody is supported on an inlet sting of 0.935 cm diameter extending from upstream in the inlet plenum chamber. Both the bellmouth and centerbody configurations have been used in previous compressor test programs. Adequate aerodynamic and mechanical performance has been obtained with these designs.

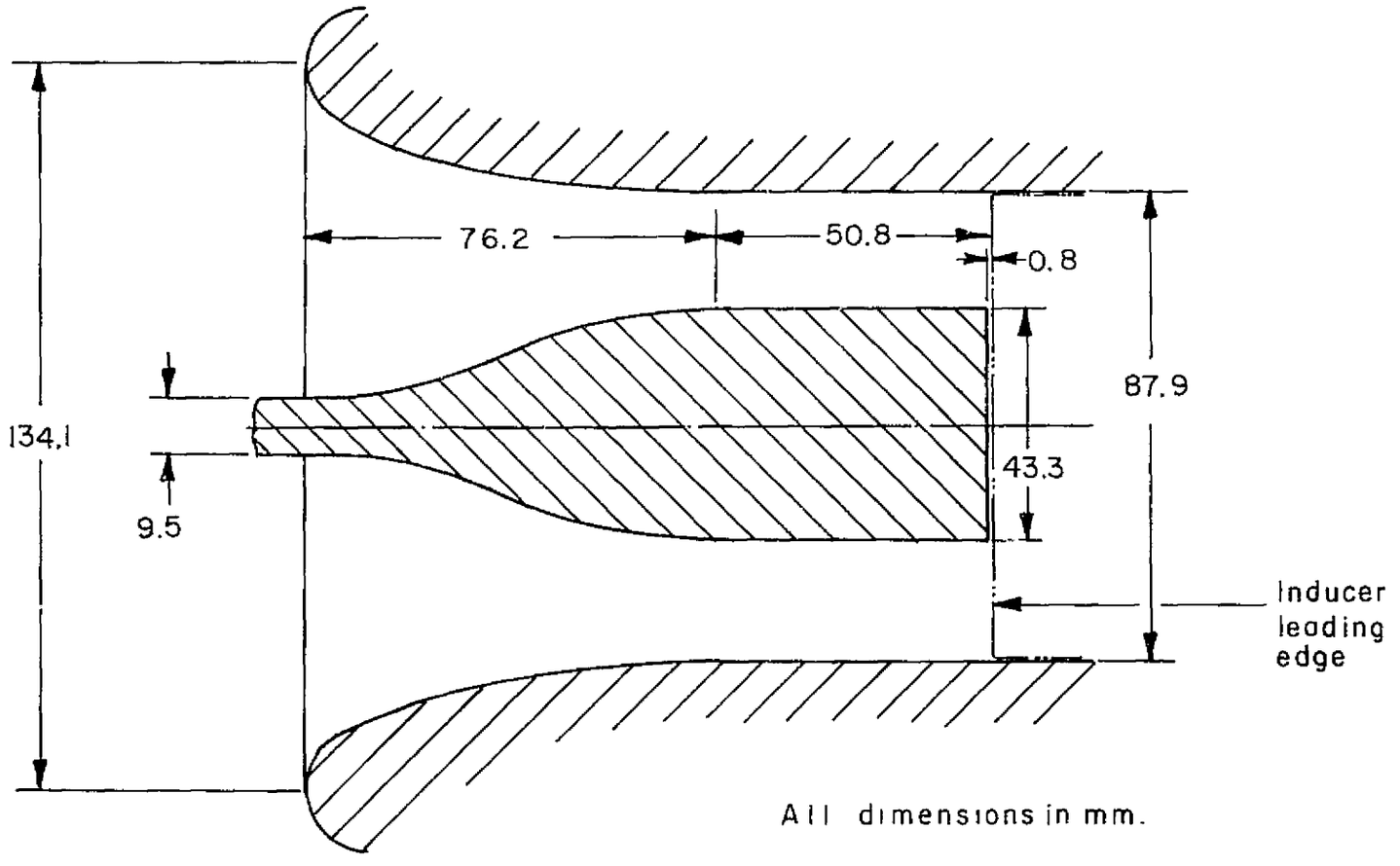

Figure33 – Compressor Inlet Geometry

DIFFUSER FINAL DESIGN

Objectives

The objectives of the final diffuser design exercise were:

1) to establish the diffuser geometry in detail,

2) to identify any deviations from the preliminary design phase performance predictions which are occasioned by the final diffuser design geometry, and

3) to examine and evaluate an alternate diffuser design which could lead to possible improved diffuser performance in terms of lower losses and increased range.

Input from Preliminary Design Analysis

All of the geometric specifications for the diffuser, as established by the preliminary design phase output were used in the design of the primary diffuser configuration. The second diffuser configuration, called here the alternate design configuration, used an increased diffuser depth. This increased depth, with the constraint of maintaining constant throat Mach number and hence total throat area at the design point, resulted in an altered channel diffuser throat aspect ratio. Hence a re-evaluation of the channel diffuser geometry was also undertaken.

The primary diffuser design had as basic input from the Preliminary Design Phase all the geometry and aerodynamic quantities for the $\beta_{2b} = -30°$ case (see Table V).

The diffuser vane-leading edge radius was not established definitively by the preliminary design analysis. A radius ratio $R_3 \simeq 1.05$ was considered to be approximately that desired based upon Creare experience. The choice cannot be defended on a very sound deterministic fluid dynamic basis. Small values of R_3 are known to:

1) increase noise level,

2) increase vibratory stress of impeller-blade trailing edges,

3) increase vibratory stress in the diffuser-vane leading edge region, and

4) increase the strength of the aerodynamic generated pressure fields in the impeller exit/diffuser entry region.

The limit on increasing the ratio R_3 is basically set by wall friction. While the design correlations for B_4, stagnation pressure loss between impeller tip and channel throat, and impeller backflow loss do not now recognize R_3 (nor any other diffuser geometrical values), it is expected that B_4 tends to rise above the blockage correlation as R_3 increases. In general, the assumption is made that it is undesirable to increase the extent of the sidewalls of the vaneless/semi-vaneless region; this implies keeping R_3 as small as possible.

As will be seen in the discussions that follow, the method used for defining the diffuser vane suction surface has effectively set the value of R_3 at 1.0764 (r_3 = 8.585 cm).

Approach

Primary diffuser design - The primary diffuser geometry was generated by applying the fluid dynamic model and methods described below to the diffuser entry region at 100% N_D and at design mass flow. It is to be recognized that the diffuser geometry generated by this approach, while presumably satisfying the aerodynamic performance at the design point conditions, may not necessarily represent the optimum geometry for other operating flows and impeller speeds. For example, incidence of the flow onto the diffuser vane lead edge, a change of channel diffuser throat Mach number with flow, etc. will change the level of overall diffuser recovery and hence stage performance.

The basic design approach assumes a core potential flow in the vaneless and semi-vaneless regions with turbulent boundary layer development on the cover and hub diffuser walls and on the vane suction surfaces. An iteration approach was used between successive solutions of the boundary layers and the core potential flow to arrive at the flow solution for the vaneless and semi-vaneless regions of the diffuser.

Once the boundary layer/core flow solution was obtained, the vane tip radius and vane suction surface were prescribed. These were set to provide for a smooth deceleration of the flow along the vane suction surface and a flow Mach number distribution approaching the channel diffuser throat close to that prescribed for the one-dimensional throat Mach number from the preliminary design analysis.

The potential core flow was calculated as a compressible, axisymmetric vortex flow. The flow was assumed completely mixed out to the 2* state at the impeller exit. The compressible vortex solution satisfies the mass flow and angular momentum relations at any radius:

$$\text{mass flow} = 2\pi\rho C_m (b-2\delta^*)r$$

$$\text{angular momentum} = 2\pi r^2 \rho C_m C_\theta (b-2\delta^*)$$

where:

C_m and C_θ are the local core flow radial and tangential velocities respectively,
b is the local diffuser depth (between cover and hub walls), and
δ^* is the boundary layer displacement thickness.

The Englert (Reference 11) compressible, turbulent boundary layer calculation technique was used to calculate the boundary layers on the hub and cover walls. The initial conditions for the boundary layer calculations were as follows. A turbulent boundary layer was prescribed to "start" on the hub wall since the boundary layer fluid leaving the impeller is "thrown" onto the hub wall at essentially wheel speed. The cover wall boundary layer was assumed to have a thickness equal to the prescribed running clearance between the impeller and cover at the impeller tip; it was assumed that the boundary layer cannot be any thicker than this since the impeller blades effectively "chop off" the boundary layer.

An empirical correlation (Ref. 1) of throat blockage B_4 versus non-dimensional pressure rise from the impeller exit-to-diffuser throat, C_{p2^*-4}, was used to establish the magnitude of boundary layer blockage at the throat. The boundary layer calculations, including the boundary layer blockage calculated on the vane suction surface,

usually do not agree exactly with the empirical B_4 vs C_{p2^*-4} correlation. Therefore, the boundary layer displacement thickness distribution between the impeller exit and channel throat was varied, proportional to streamline distance from the impeller exit, by an amount sufficient to produce the throat blockage given by the empirical correlation. Thus the throat area, aspect ratio and mean Mach number were all maintained as given by the preliminary design calculations.

The vane suction surface was displaced away from the core flow "suction surface streamline" by an amount equal to the calculated displacement thickness of the suction surface boundary layer so as to maintain the core flow streamlines as calculated. Finally, the location of the vane tip radius was prescribed by the necessity of the tip radius and vane suction surface contour providing the required channel diffuser throat width, W_4. The vane tip radius was set as small as practical from fabrication and assembly considerations. The vane suction surface (plus boundary layer displacement thickness) is aligned to follow the vortex flow streamline. The vane pressure surface was laid out tangent to the vortex flow streamline impinging on the vane lead edge. Thus all the divergence is taken in the suction surface. The mass averaged Mach number at the diffuser exit was calculated to be 0.155 with a total pressure of $8.24 \times 10^5 N/m^2$.

Figure 34 displays the type of vaned diffuser geometry specified by this design procedure and summarizes the conditions established by this design approach.

Alternate diffuser design - An alternate diffuser configuration separate from the primary diffuser design, was designed and fabricated. This diffuser is called the step diffuser because a sudden expansion (increase in axial diffuser depth) is provided immediately at the impeller exit radius. The concept behind this diffuser design is the provision of a "smoke shelf" on the front diffuser cover at the impeller exit radius. This "smoke shelf" is intended to provide the effect established in the chimney of a fireplace, namely, to establish a fixed separation point for the flow and prevent the backflow of fluid. In this case, the "smoke shelf" or step is provided on the diffuser front cover to prevent radially momentum deficient fluid on the cover from being driven back into the impeller by the imposed diffuser radial pressure gradient.

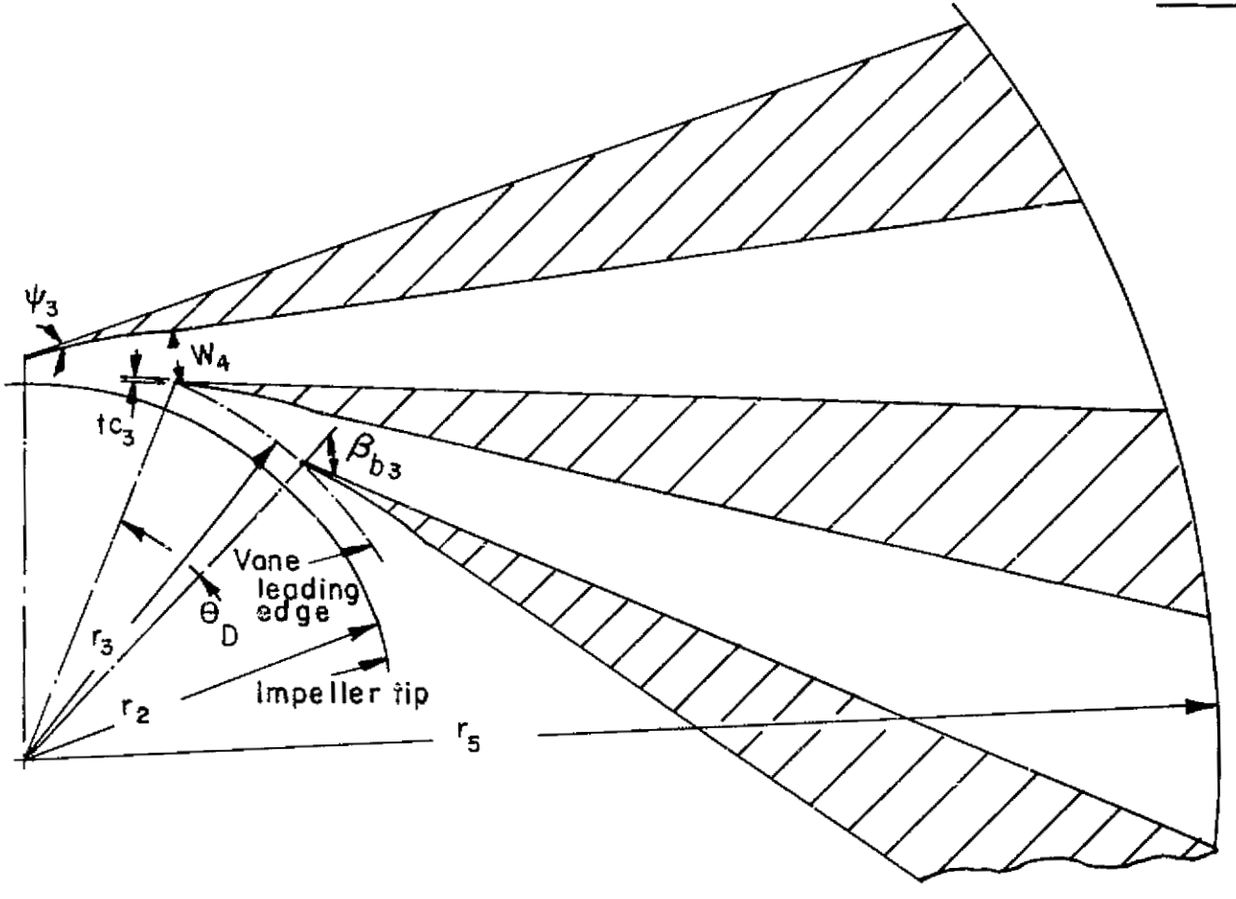

Diffuser parameters

$r_2 = 79.76$
$Z_D = 17$
$r_3 = 85.85$
$tc_3 = 0.254$
$\psi = 0°$
$\beta_{b3} = 70.04°$
$W_4 = 11.48$
$b_4 = 3.24$
$2\theta = 10°$
$L/W_4 = 17$
$r_5 = 254$
$\theta_D = 21.18°$

Circumferential plane divergence

All dimensions in mm.

Figure 34—Vaned Diffuser Geometry — Primary Design

The design provided for a step height equal to 10% of the nominal impeller exit depth. Downstream of this step change in depth, the diffuser passage was held at constant depth. The remaining design procedures, namely the specification of the diffuser vane suction surface geometry, lead edge radius and channel diffuser geometry, followed the same design methodology as described above for the primary diffuser. The additional input required in the step diffuser design was the description of the boundary layer displacement thickness growth on the front cover in the region of the step separation. Correlations of separation length behind backward facing steps, under a range of free stream Mach numbers up to sonic, show that the separation length is on the order of 5 to 10 step heights (Ref. 14 to 15). For the step height of this design (3.23×10^{-4} meters), the length of the separation zone is so small, order of 3.23×10^{-3} meters, that the influence of the free shear layer on the growth of the displacement thickness over the separation zone has been neglected; the boundary layer has been assumed to grow in displacement thickness the same as would occur if the separation zone were a solid surface. The final diffuser vane geometry was changed from the primary diffuser design because the free vortex flow occurs with a wider diffuser depth.

Figure 35 displays the final vaned diffuser geometry specified by this design procedure and summarizes the conditions established by this design approach.

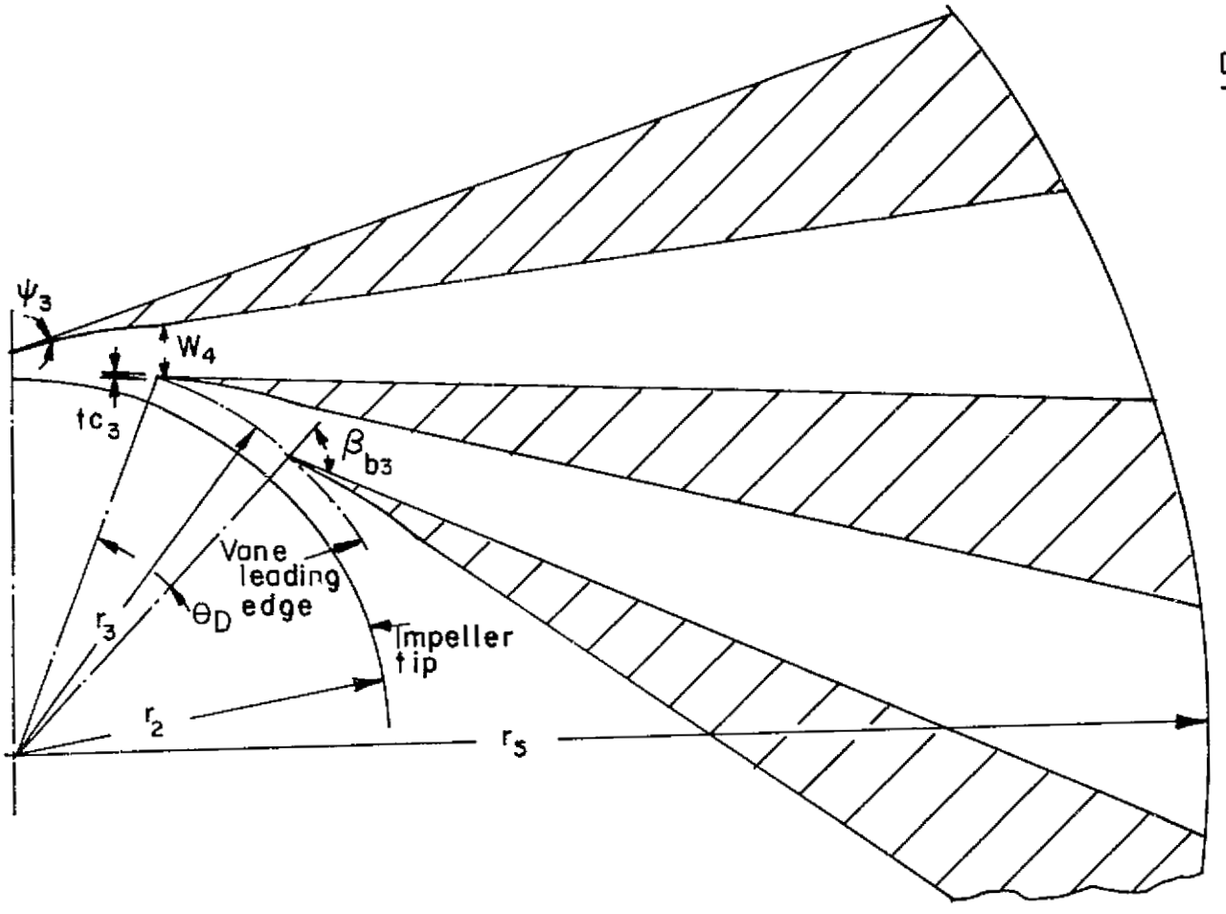

Diffuser parameters

r_2 = 79.76
Z_D = 17
r_3 = 85.48
tc_3 = 0.254
ψ_3 = 0°
β_{b3} = 71.87°
W_4 = 10.43
b_4 = 3.56
2θ = 10°
L/W_4 = 18.6
r_5 = 254
θ_D = 21.18°
Circumferential plane divergence

All dimensions in mm.

Figure 35—Vaned Diffuser Geometry — Alternate Design

COMPRESSOR INSTRUMENTATION

The compressor unit has been instrumented (emphasis on aerodynamic instrumentation) in order to provide (i) an adequate description of the flow states within the compressor unit and (ii) monitor shaft vibrational modes during running. This instrumentation includes instantaneous and time-averaged static pressure taps, time-averaged total pressure probes, temperature thermocouples, inlet flow survey instrumentation and dynamic clearance probes. These items are fully described below (with figures and tables) according to type of instrument and location.

Also included in the final instrumentation package to be used on this compressor is a Laser Doppler Velocimeter (LDV) system (designed and fabricated under a separate program). This LDV system will be used to measure velocity components in the impeller inducer region and in the diffuser vaneless and semi-vaneless spaces. Special LDV windows have been inserted in the cover and in the diffuser front plate to provide quality optical surfaces for the LDV optical studies. The critical LDV window configuration is the diffuser one, where the window must span several diffuser vane tips and mechanically support and aerodynamically seal across the diffuser vanes. Analyses and experimental bench tests have been made of these LDV window configurations to ensure that the problems associated with the thermal mechanical stress, differential thermal expansion and resultant leakage between window quartz and diffuser cover metal, and mechanical clamping of diffuser vanes with the quartz window can be successfully dealt with in compressor test operation. The design of the LDV system has been carried out under a companion contract. Full details of the LDV configuration may be found in Reference 12.

Type and Location of Aerodynamic Instrumentation

The following measurements will be made on this compressor unit:

- time-averaged static pressures
- instantaneous (time varying) static pressures
- time-averaged total pressures

- temperature measurements
- inlet flow direction survey

Reference system - Top dead center on the machine is identified as $\theta = 0°$. Theta is measured positive counterclockwise when looking into the inlet. One diffuser vane tip is located at $\theta = 0°$. An odd number of vanes then implies that bottom dead center splits the pitch of two vane tips. Since pitch = 21.18", $\theta = 0°$ aligns with the first vane tip and $\theta = 10.6°$ is mid-pitch. The inducer blade lead edge is set at X = 0, and X is positive in the flow direction.

Time-averaged static pressures

a) Inlet Static Taps - See Figure 36.

Three (3) taps, each at two (2) circumferential locations were positioned on the inlet cover. The axial locations of these taps are 0.63, 1.27, and 2.54 centimeters ahead of of the inducer leading edge (X = 0). The circumferential locations are at $\theta = 0°$ and $\theta = 10.6°$.

b) Impeller Cover Taps - See Figure 37.

Impeller cover taps are located at three (3) circumferential locations. These are at mid-pitch of channel 1 ($\theta = 10.6°$), 5/6 pitch of channel 1 ($\theta = 17.66°$), and 1/6 pitch of channel 2 ($\theta = 24.72°$).

The meridional locations of these taps coincide with the shroud streamline constant θ locations used in the VANCO program, plus several extra tap locations. Table VII presents the locations of these taps on the cover inside surface in terms of X (axial distance from inducer leading edge) and r (radius).

c) Impeller Tip Static Taps - See Figure 38.

Impeller tip static pressure taps are located on the front cover in an arc to span a diffuser entry region. Eight (8) taps span the entry

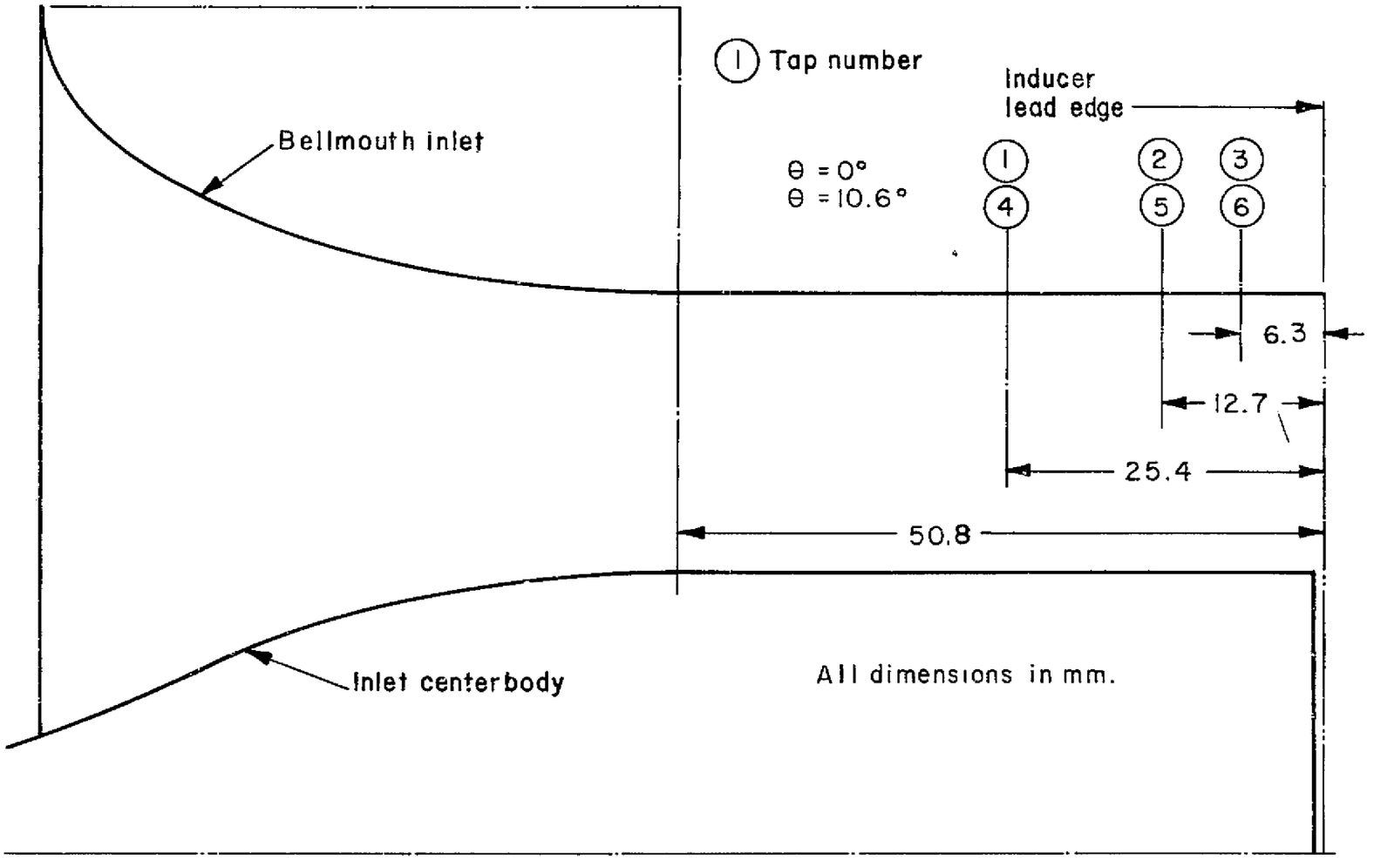

Figure 36–Inlet Static Tap Locations

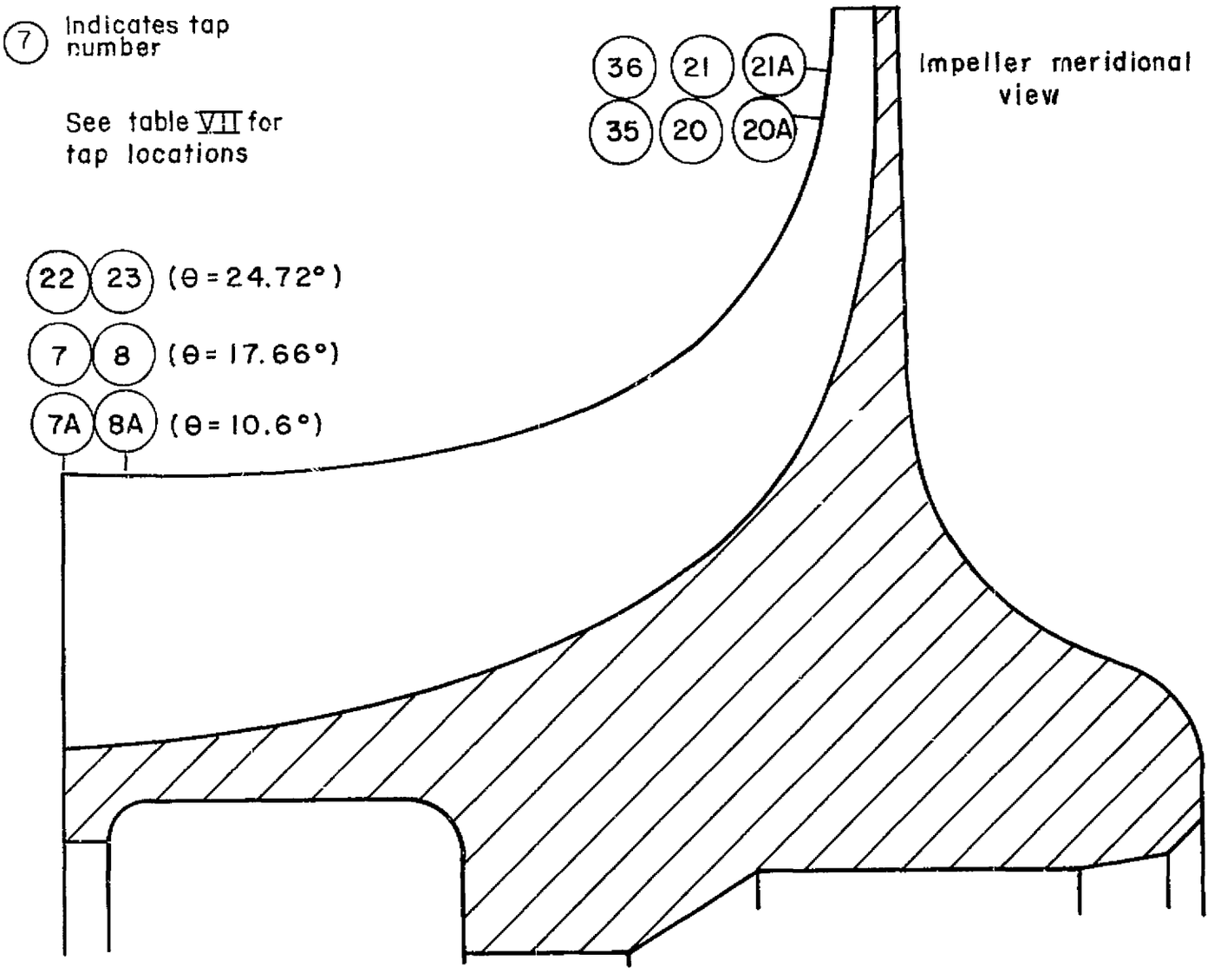

Figure 37—Impeller Cover Static Tap Locations

TABLE VII - IMPELLER COVER STATIC TAP LOCATIONS

Tap Number			Axial Distance, X (cms)	Radial Distance, r (cms)
7a	7	22	0	4.40
8a	8	23	0.51	4.40
9a	9	24	1.02	4.40
10a	10	25	1.65	4.40
11a	11	26	2.18	4.41
12a	12	27	2.67	4.45
13a	13	28	3.28	4.56
14a	14	29	3.84	4.72
15a	15	30	4.34	4.94
16a	16	31	4.88	5.30
17a	17	32	5.24	5.65
18a	18	33	5.47	5.97
19a	19	34	5.66	6.31
20a	20	35	5.81	6.70
21a	21	36	5.95	7.25

Taps 7a through 21a are located at $\theta = 10.6°$.

Taps 7 through 21 are located at $\theta = 17.66°$. See Figure 37.

Taps 22 through 36 are located at $\theta = 24.72°$.

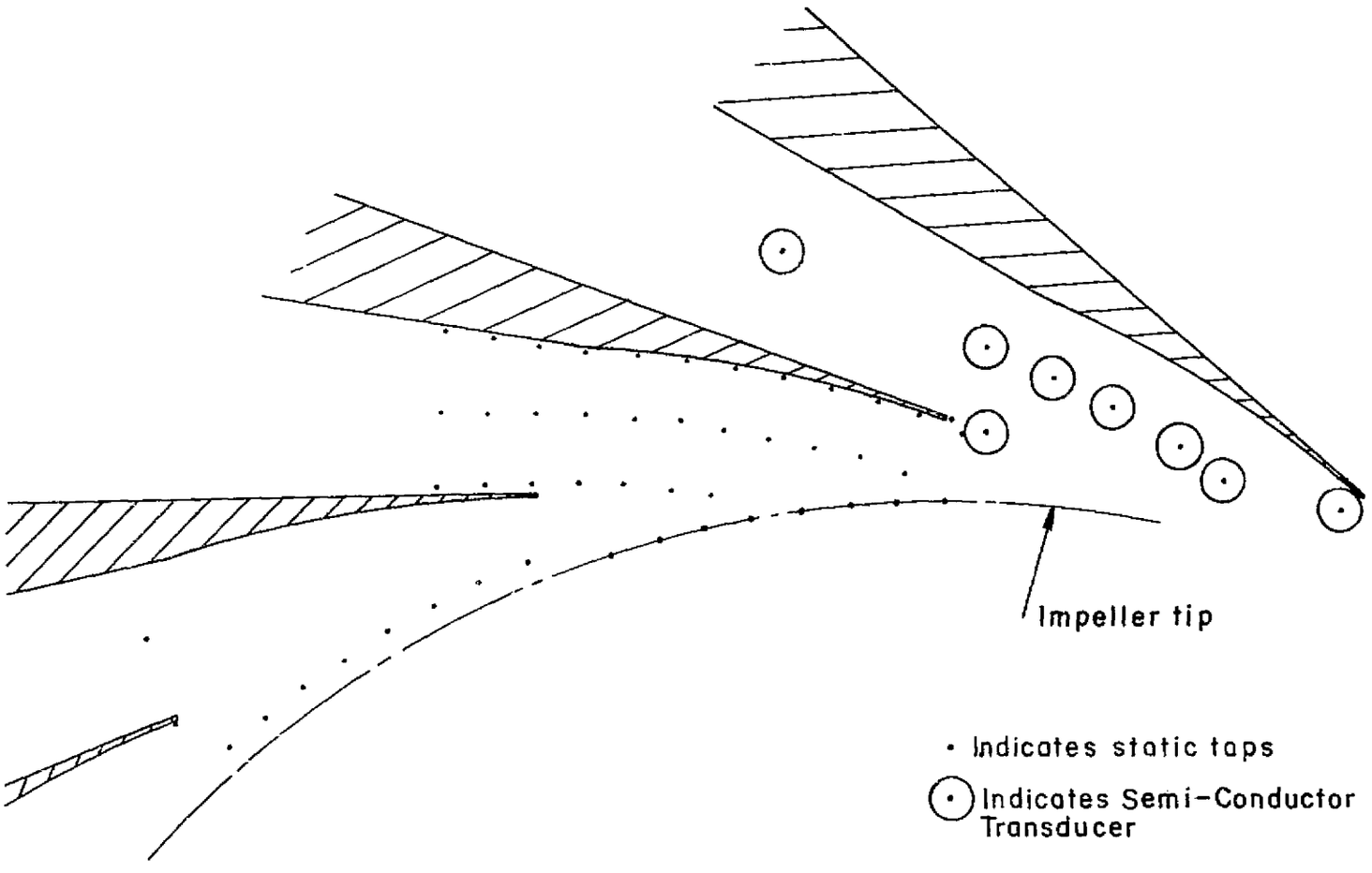

Figure 38 – Pressure Static Taps and Semi-Conductor Transducer Locations in Diffuser inlet

region between vane tips (in channel 1). Another set of eight (8) taps has been placed at r = 1.02 r_2 radius. This second set is located one vane island pitch over from the first set at r = 1.0 r_2 (i.e., in channel 2). r, θ positions are given in Table VIII.

TABLE VIII - IMPELLER TIP STATIC TAP LOCATION

Tap Number	Radial Distance, r (cms)	Angular Location, θ (degrees)
37	7.99	0
38	7.99	2.71
39	7.99	5.57
40	7.99	8.24
41	7.99	10.91
42	7.99	13.40
43	7.99	15.97
44	7.99	18.74
45	8.16	22.70
46	8.15	25.34
47	8.15	28.05
48	8.15	30.86
49	8.14	33.55
50	8.15	36.07
51	8.15	38.58
52	8.15	41.12

d) Vaneless/Semi-Vaneless Array - See Figure 38. An array of static pressure taps is located in the vaneless and semi-vaneless region between the impeller tip and the diffuser throat on the front cover. The taps form three (3) arcs which approximate the suction surface, centerline and pressure surface streamlines for channel 1. Table IX displays the r, θ coordinates of these taps.

TABLE IX - VANELESS/SEMI-VANELESS STATIC TAP LOCATIONS

Tap Number	Radial Distance, r (cms)	Angular Location, θ (degrees)
53	8.51	-1.00
54	8.64	1.27
55	8.76	3.30
56	8.87	5.54
57	8.99	7.76
58	9.12	9.91
59	9.25	12.16
60	9.36	14.27
61	9.48	16.45
62	9.63	18.43
63	9.80	20.23
64	9.98	22.05
65	8.20	2.20
66	8.32	4.30
67	8.44	6.66
68	8.56	8.99
69	8.68	10.99
70	9.25	13.13
71	8.91	15.13
72	9.02	17.32
73	9.16	19.59
74	9.28	21.67
75	9.43	23.62
76	8.21	12.24
77	8.33	14.38
78	8.45	16.57
79	8.55	18.67
80	8.69	20.96
81	8.80	23.04
82	8.95	25.11
83	8.63	-0.40
102	8.55	42.50

e) Channel Diffuser Taps

An array of static pressure taps is located in one channel diffuser on the front cover. These taps are spaced approximately three (3) throat widths apart along the centerline of channel 1. Table X presents the r, θ coordinates of the taps as well as those of additional throat taps.

TABLE X - CHANNEL DIFFUSER STATIC TAP LOCATIONS

Tap Number	Radial Distance, r (cms)	Angular Location, θ (degrees)
84	10.81	35.51
85	13.16	46.85
86	15.80	54.41
87	18.60	59.72
88	21.73	63.77
89	24.72	66.69
90	9.18	-1.98
91	9.17	40.77
92	9.17	61.97
93	9.16	83.22
94	9.17	104.60
95	9.15	125.78
96	9.16	147.00
97	9.17	168.20
98	9.17	230.90
99	9.17	252.14
100	9.18	266.76
101	9.20	336.90

Time Varying Static Taps

All dynamic (instantaneous) pressures are measured with semi-conductor pressure transducers. These transducers have a 0.216 cm diameter pressure-active diaphragm with an allowable minimum spacing between transducers of 0.939 cm, center to center. Because of a large zero pressure shift with temperature, DC pressure levels are not easily determined with these transducers.

a) Inlet and Impeller Locations - See Figure 39.

There are ten (10) semi-conductor pressure transducer locations spaced through the inducer and impeller. The scheme employed was to wrap the transducer locations to correspond with the impeller blade wrap so that the transducers see the blades beneath them simultaneously. The locations are staggered circumferentially as required for clearance

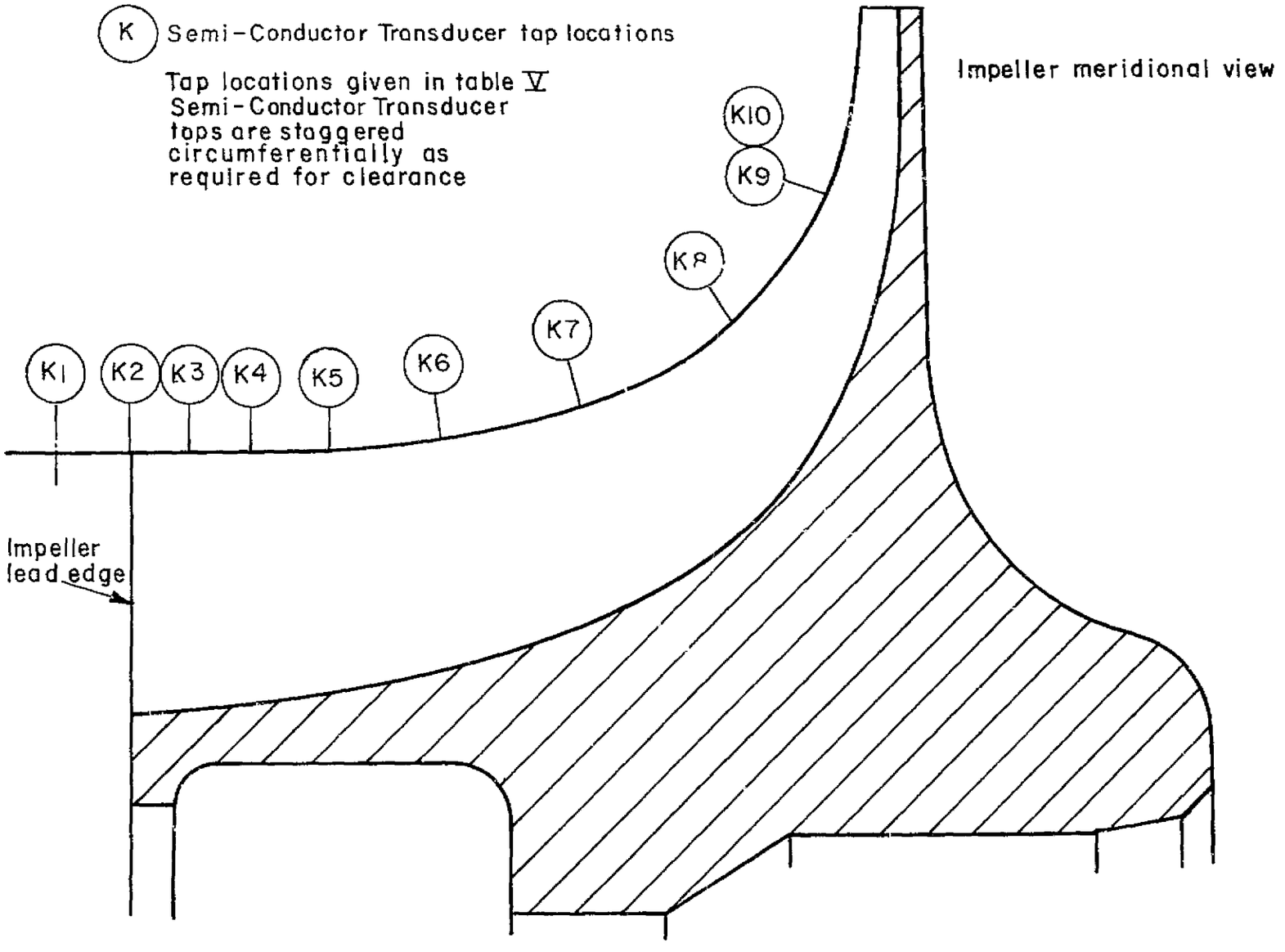

Figure 39–Inlet and Impeller Semi-Conductor Transducer Locations

and so as not to interfere with the time-averaged static taps. One probe is located 0.635 cms ahead of the inducer leading edge. The coordinates of these taps are indicated in Table XI. The optical trigger which indicates blade position is located at X = 3.284 cms, r = 4.556 cms, and θ = 52.9°.

TABLE XI - IMPELLER AND INLET TRANSDUCER LOCATIONS

Number	Axial Distance, X (cms)	Radial Distance, r (cms)	Angular Location, θ (degrees)
K1	-0.64	4.40	88.4
K2	0	4.40	67.2
K3	0.51	4.40	78.9
K4	1.02	4.40	92.5
K5	1.65	4.40	64.9
K6	2.18	4.41	80.6
K7	3.28	4.56	74.1
K8	5.24	5.65	87.0
K9	5.66	6.31	63.6
K10	5.66	6.31	74.2

Optical trigger located at X = 3.28 cms, r = 4.56 cms, θ = 52.9°

b) Diffuser Locations - See Figure 38.

There are eight (8) semi-conductor transducers located in the front cover and spanning the diffuser entrance and vane tip region. Five (5) of the transducers lie approximately along the central streamline with another 1-1/2 throat width downstream of the diffuser throat. The remaining two (2) transducers are located near the vane tip. These taps are staggered circumferentially and located in several diffuser entry regions for clearance and so as not to interfere with the time-averaged static pressure probes. They are shown in one channel

in Figure 38 in order to show the region covered. The actual positions are given in Table XII.

TABLE XII - DIFFUSER INLET TRANSDUCER LOCATIONS

Tap Number	Radial Distance, r (cms)	Angular Location, θ (degrees)
K11	8.45	324.30
K12	8.61	284.50
K13	8.84	309.20
K14	8.99	291.15
K15	9.18	315.60
K16	8.51	336.00
K17	8.46	276.15
K18	9.98	324.30

Time-Averaged Total Pressure

a) Inlet Plenum

Two (2) wall static taps are used to obtain the plenum total pressure.

b) Collector

Five (5) wall static taps are spaced around the dump region of the collector. All of these taps should read the same pressure. A typical design of a static pressure tap is shown in Figure 40.

c) Channel Diffuser Throat Taps

Three (3) small total pressure probes are located in the front cover and approximately one throat width downstream of their respective throats. This is well downstream of the position (0.468 x throat width) at which the channel area minus probe blockage equals the throat area. Figure 41 shows the probe design.

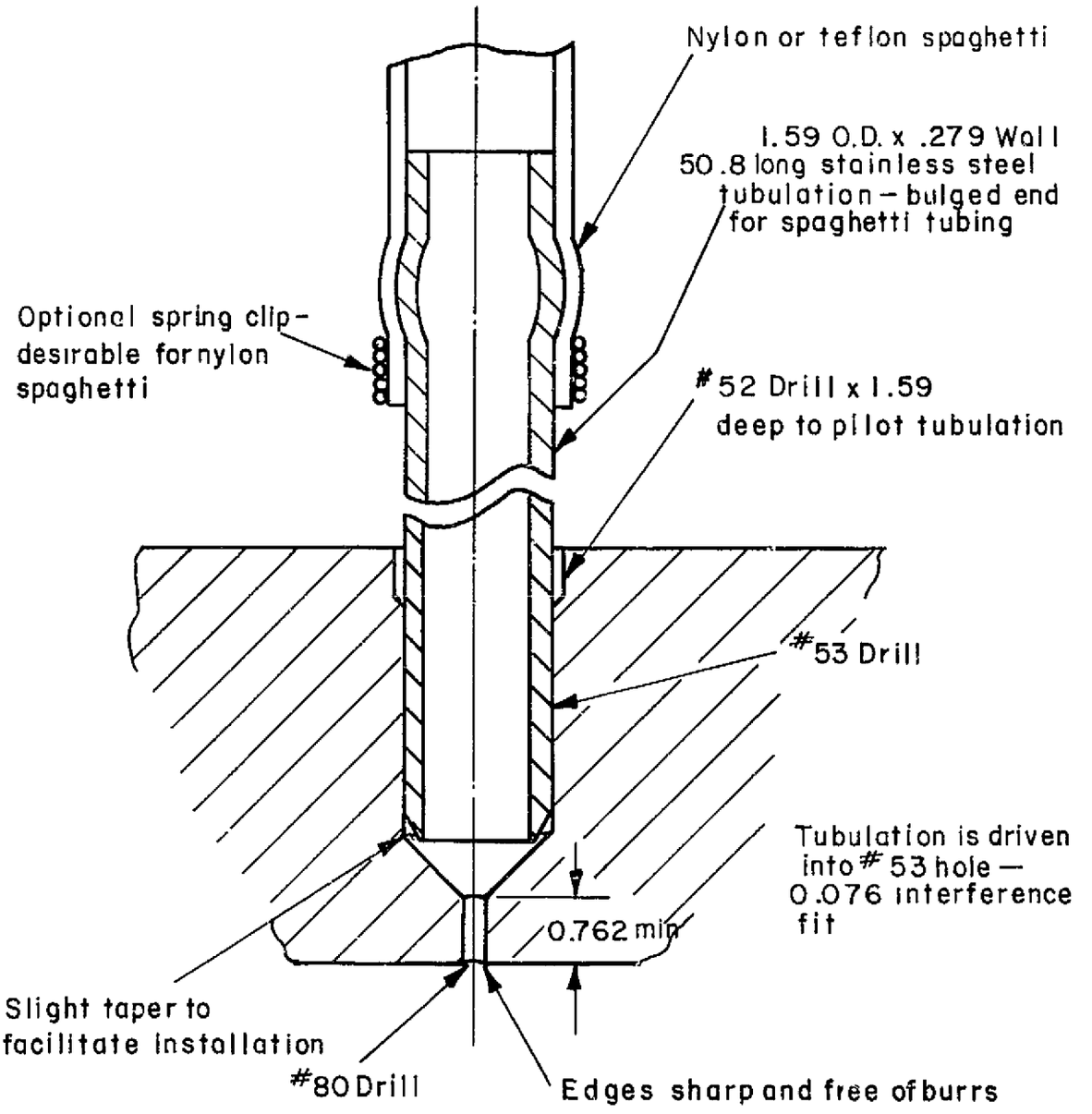

Figure 40—Typical Design of Static Pressure Tap and Connector

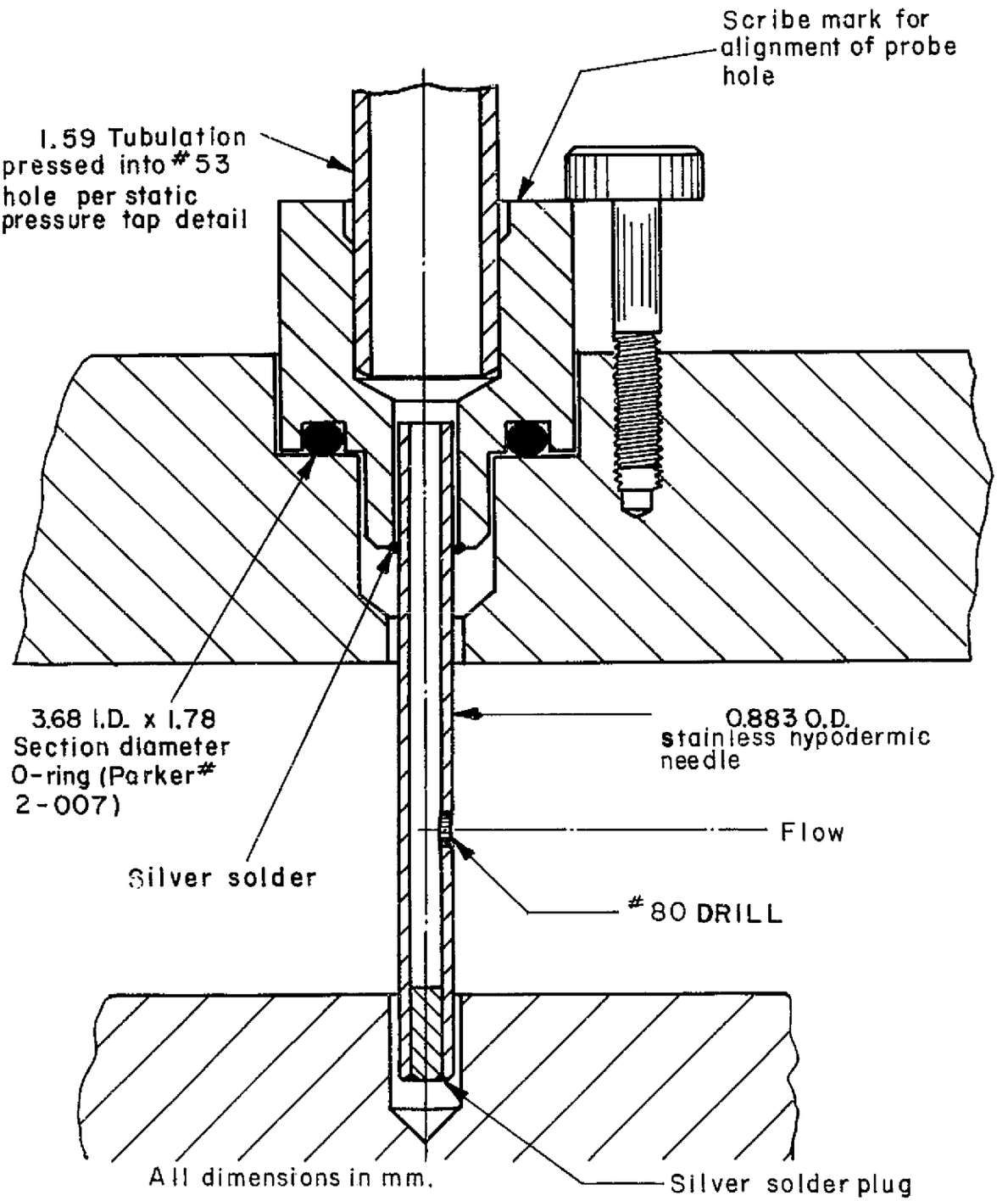

Figure 41 — P_{04} Total Pressure Probes and Installation

Temperature Measurements

a) Total (static) Temperature Inlet Plenum.

A setup of three (3) Fe-Con thermocouples is used to make these measurements.

b) Total (static) Temperature Collector.

Five (5) Fe-Con shielded thermocouples are located around the collector. All of these thermocouples should read the same.

Inlet Flow Survey

At the inlet to the inducer, a three-hole cobra probe is used to determine flow direction and static/total pressure. The cobra probe has a head width of 0.152 cm and is traversed manually in a radial line. Two axial locations at 0.625 cms and 2.54 cms ahead of the inducer lead edge will be used, with circumferential locations 345° and 300°, respectively.

Mechanical Instrumentation

The steady-state and fluctuating components of the impeller axial motion at the tip region will be measured. This measurement is useful for diagnosing the mechanical behavior of the impeller, and for monitoring running clearances during system transients.

A proximity type sensor has been found to be useful for this purpose. The sensor operates on the inductive proximity principle and therefore need not make electrical or mechanical contact with the rotating hardware. Measuring systems are available with operating ranges from about five (5) millimeters to about half a centimeter, and with a gain (output) or about 200 mv per 0.0025 cms.

Because the probe is sensitive to any electrically conductive material in its vicinity, it should be calibrated (output vs. displacement) with the same hardware in which it will ultimately be used. If this is not feasible, the calibration may be performed in a test fixture which replicates the materials and geometry in the area surrounding the probe at the anticipated installation point.

This proximity sensing system is also sensitive to the temperature of the probe - a change of 11.30°C being approximately equivalent in output to a displacement change of 0.0025 cms. Thus, the probe should also be calibrated over the expected temperature range. During actual use, a thermocouple or thermistor placed adjacent to the probe is used for accurate temperature indication. (See Figure 42.)

Readout instrumentation for this instrument consists of a digital DC voltmeter for the steady state displacement and an oscilloscope for monitoring the fluctuating or transient behavior.

The proximity measuring system consists of the probe, its signal conditioner and an 18 volt DC power supply.

Readout Instrumentation

All time-averaged static pressures will be read on Creare's pressure transducer system which includes pneumatic switches, diaphragm-resistance bridge transducers with power supplies and a digital millivoltmeter.

The dynamic component of the static pressures will be recorded with oscilloscope and oscillograph traces, depending on the frequency of the signal of interest.

In addition to the dynamic pressure traces, a simultaneous recording of the impeller position will be made. The impeller position measurement can be made using an optical pickup placed to look at the inducer blades. This will require prior calibration to correlate the blade position relative to the pickup with the output signal.

Temperature measurements will be read out on a digital millivoltmeter through an electrical switching system.

The flow direction survey will use a water manometer for nulling the cobra probe. Total pressure will be measured with the time-averaging transducers. Flow angle and radial position are measured with conventional apparatus available in-house.

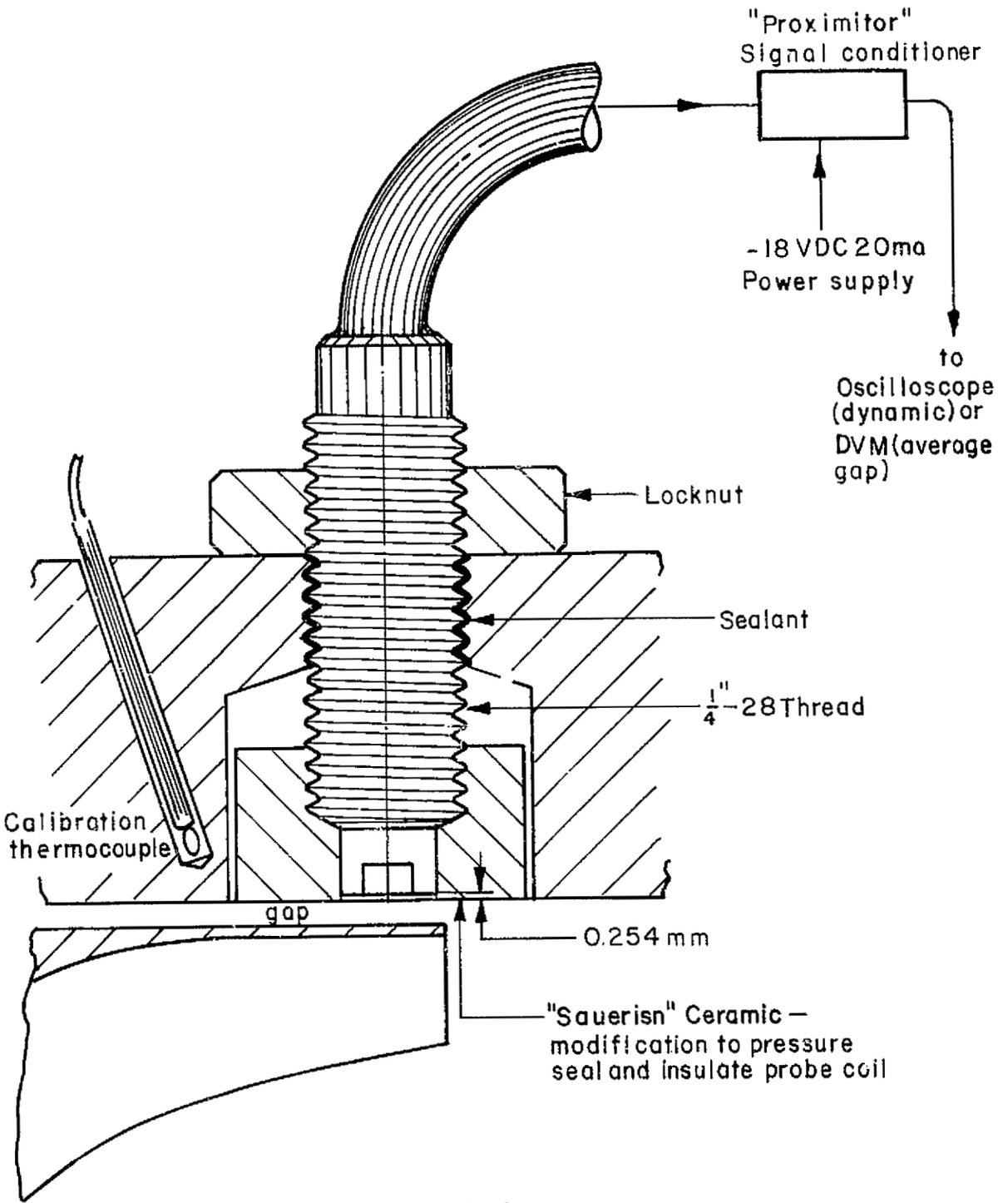

Figure 42—Proximity Probe

ORIGINAL PAGE IS
OF POOR QUALITY

MECHANICAL DESIGN

Mechanical, material and stress analyses were carried out for the several compressor components in order to assure adequate operation of the compressor stage during low speed model testing in Creare's facilities and to meet contract specifications for possible future testing of the compressor hardware at NASA's facilities.

Creare will conduct all testing on this compressor using the Low Speed Modeling facility located in Creare's laboratories. Thus, although the compressor aerodynamic and mechanical design has been carried out for 100% N_D (100% of design speed) = 75,000 RPM, testing of this compressor at equivalent 100% N_D will occur at an actual rotational speed of approximately 52,500 RPM. While the mechanical rotational stress analysis has been conducted for speeds up to 120% of 75,000 RPM (120% of design speed in air), the blade vibrational analyses and shaft critical speed analyses were carried out for the lower LSM operating speeds.

Basic LSM Rig Description

A diagramatic view of the LSM rig showing the principal loop components is given in Figure 43.

The compressor impeller is designed to mount on Creare's high speed gear box. The high speed rotating assembly is of overhung design. The entire compressor assembly is supported from a massive inlet plenum; the basic support structure of the assembly is a large back plate which carries the gear box and from which the diffuser and cover components are supported. The inlet is compliantly coupled to the plenum.

This configuration has been used in past compressor testing at Creare with no mechanical difficulties encountered. The entire non-rotating assembly, diffuser, impeller back plate and covers, has been designed to maintain critical dimensional tolerances, especially diffuser dimensions and impeller-to-cover running clearances at all speeds. This has been proved in compressor testing.

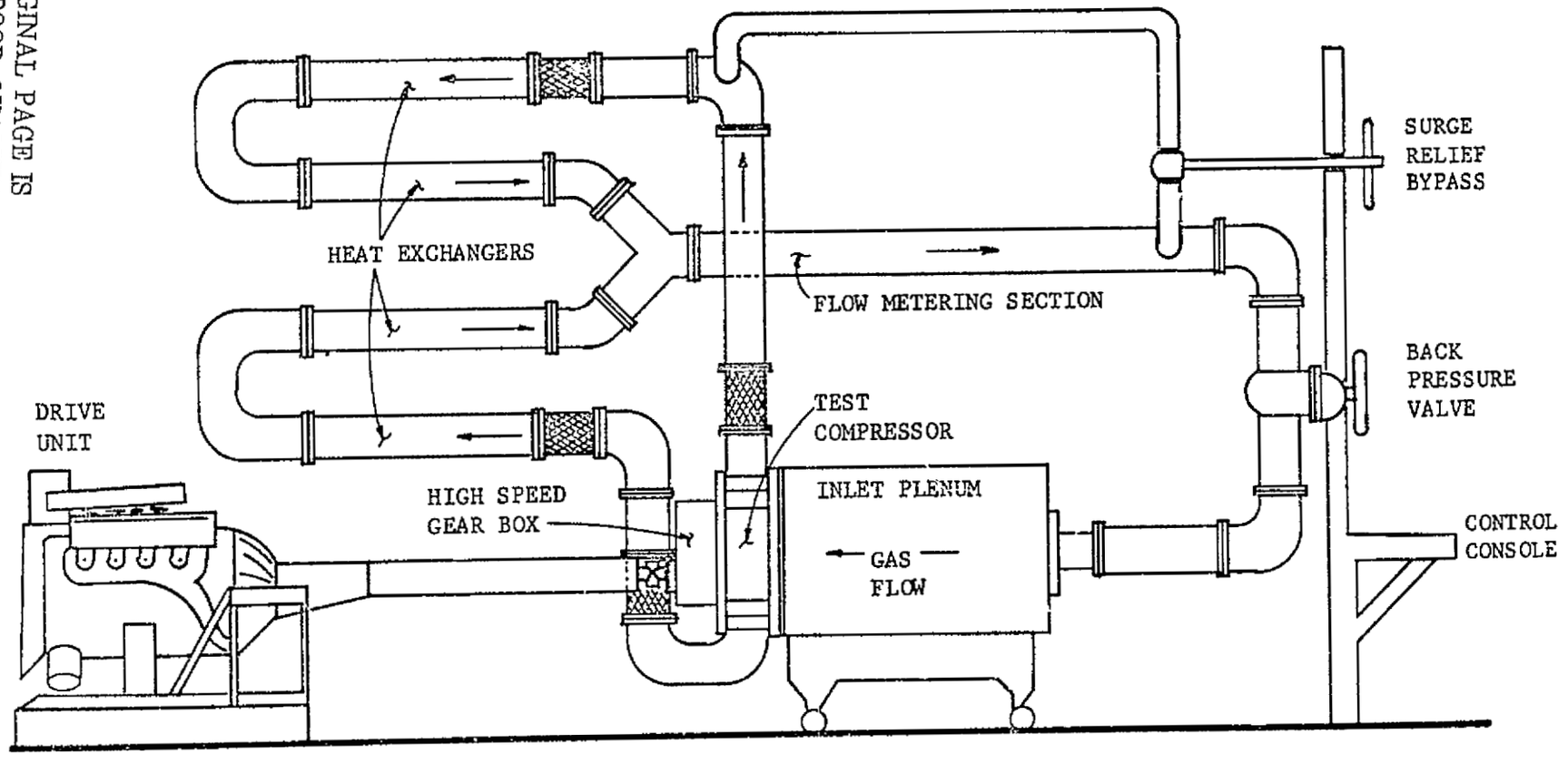

Figure 43 - Low Speed Modeling Test Facility

The components of the compressor assembly are:

- high speed rotating components (shaft, bearings, impeller, and impeller mounting hardware),
- inlet, inlet centerbody and inlet-to-plenum hardware,
- impeller cover (shroud),
- impeller back plate and seals,
- diffuser components (diffuser front plate, diffuser back plate, diffuser vanes), and
- miscellaneous hardware (bolts, nuts, O-rings, etc.).

The major components of the compressor unit are displayed (in a meridional view layout) in Figure 44 The components designed and fabricated on this program are indicated by the cross hatched parts of the figure.

High Speed Rotating Components

The principal analyses performed on the rotating hardware were:

- impeller material selection,
- impeller stress and vibration analyses, and
- impeller/shaft/bearing critical speed analyses.

Material selection - Annealed titanium alloy (Ti-6Al-4V) forging was selected as the material for the impeller. The primary consideration in selecting titanium was the maintanence of high strength/weight ratio at elevated temperatures. While several heat treated steels have superior absolute strength characteristics and several aluminum alloys are preferable on a low temperature strength/weight basis, titanium alloys are preferable for high strength application between 204°C and 538°C.

The applicable material specification for selecting Ti-6Al-4V material is S.A.E. Specification AMS4928G. This specification defines minimum strength and ductility

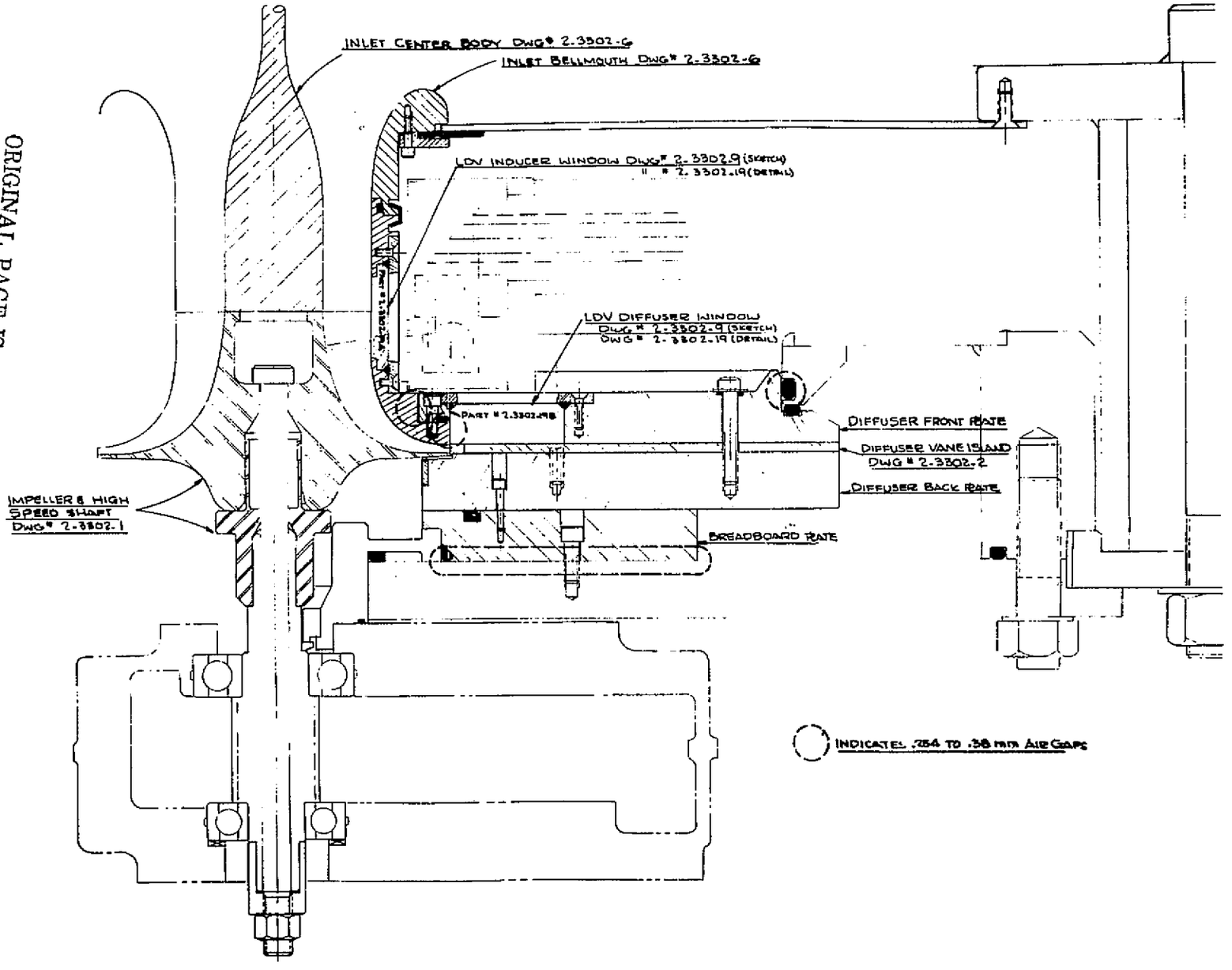

Figure 44. Compressor Stage - Meridional View

(elongation and reduction in area) and exceeds the requirements of the comparable military specification MIL-T-9047E.

Impeller stress - The blade stresses (blade root) were calculated using simplified approximate calculation methods intended to be basically conservative and to verify that the final aerodynamic design would pass detailed mechanical analyses. Blade vibration modes and frequencies and disc stresses were calculated by the Boeing Company using NASTRAN and WASP finite element programs.

Creare's BLSTRS program calculates centrifugal forces arising from the rotating blade mass. The root blade force $F \propto \int_{r_t}^{r_h} r\omega^2 \rho d(Vol/dr)$ is computed over an incremental axial length. dVol/dr depends upon blade taper ratio and blade section profile. Output is force per unit axial length exerted by the blade on the disc. The program also uses blade root area to obtain the blade root stress. In the essentially radial portion of the impeller (i.e., near the exit), a subroutine resolves the centrifugal force into components parallel and normal to the backward leaning blade and uses the normal component to compute the root bending stress. Bending stress is based upon a simple cantilevered beam idealization. Figure 45 shows the blade root tensile, bending, and combined stresses for 90,000 RPM (120% design air speed) operation with the design blade contour. Table XIII displays the calculated blade root stresses.

Wheel mass, moment of inertia, and estimated burst speed were calculated by Boeing. These values are displayed in Table XIV. Burst speed was calculated at 110,740 RPM for the disc at room temperature. A 107,000 RPM (142.7% N_D air) burst speed at an average disc temperature of 149°C was calculated.

Blade vibration frequencies were calculated via NASTRAN finite element program. The resulting Campbell diagram is shown in Figure 46. All blade frequencies within the anticipated operating speed range are inducer blade modes. The impeller tip modes are so high as to not be excited in the operating range.

TABLE XIII - IMPELLER BLADE ROOT STRESSES (90,000 RPM)

Calculation Station*	Radial Stress ($\frac{Newt}{m^2} \times 10^{8}$)	Bending Stress ($\frac{Newt}{m^2} \times 10^{8}$)	MH**Stress ($\frac{Newt}{m^2} \times 10^{8}$)
1	2.34	1.35	
2	2.83	0.87	
3	3.30	0.86	2.87
4	3.54	0.94	3.40
5	3.92	1.22	4.03
6	4.05	1.60	4.56
7	3.22	1.84	5.09
8	2.68	2.42	5.65
9	2.11		
10	1.96		
11	1.84		
12	1.72		
13	1.65		
14	1.54		
15	1.50		
16	1.48		
17	1.48		
18	1.50		
19	1.54		
20	1.60		

* See Figure 45.
** Mises-Hencky Stress.

TABLE XIV - PHYSICAL CHARACTERISTICS OF IMPELLER

	Weight (kg)	Polar Moment of Inertia, I_{zz} ($kg.m^2$)
Blade	0.0118	2.60×10^{-5}
Total for 19 Blades	0.2240	4.95×10^{-4}
Disc	1.2250	1.53×10^{-3}
Total Impeller	1.4490	2.02×10^{-3}

Minimum burst speed at 149°C metal temperature is 107,000 RPM.

Maximum allowable speed for prolonged operation at 149°C metal temperature is 80,000 RPM.

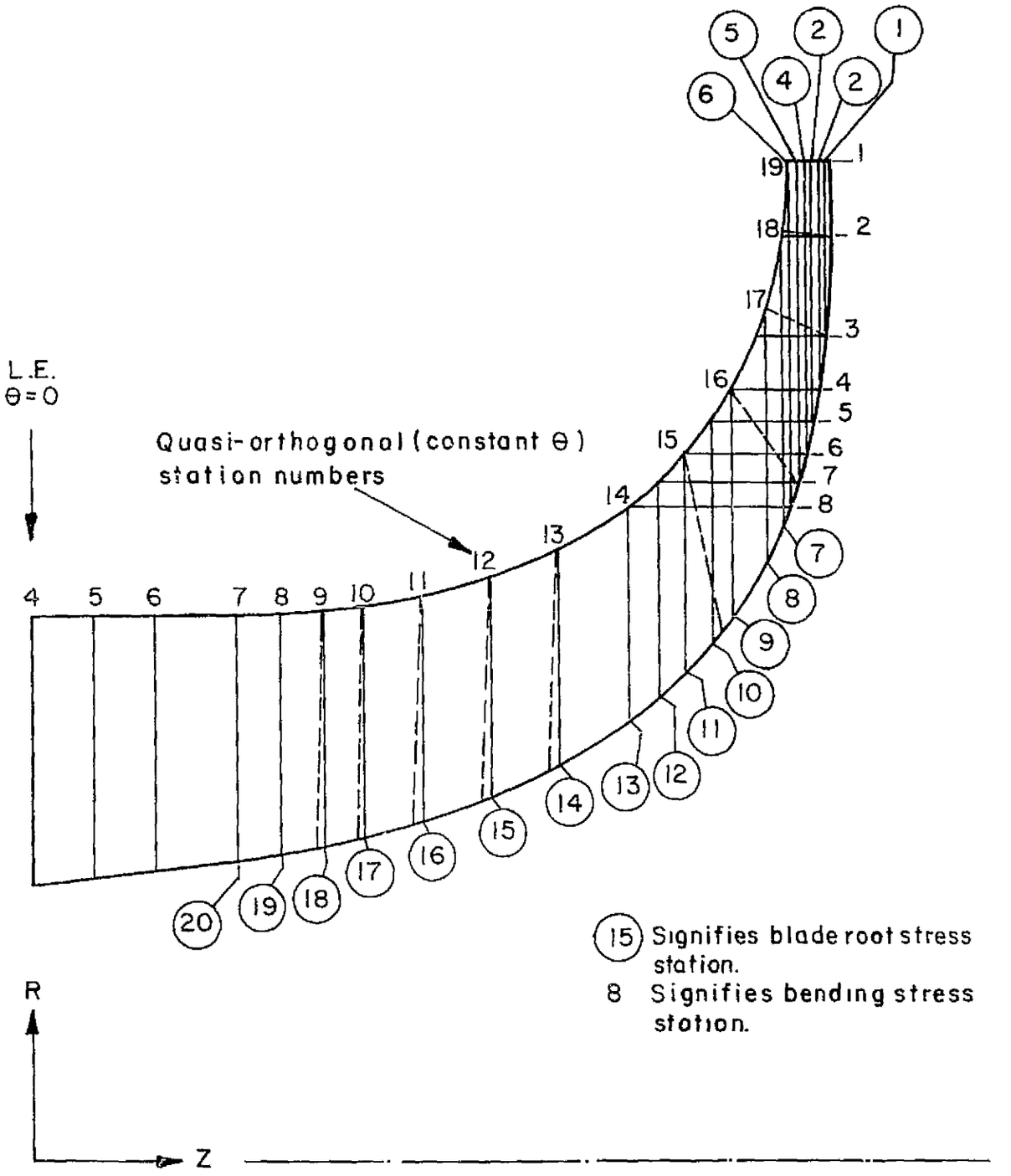

Figure 45—Definition of Impeller Stress Calculation Stations

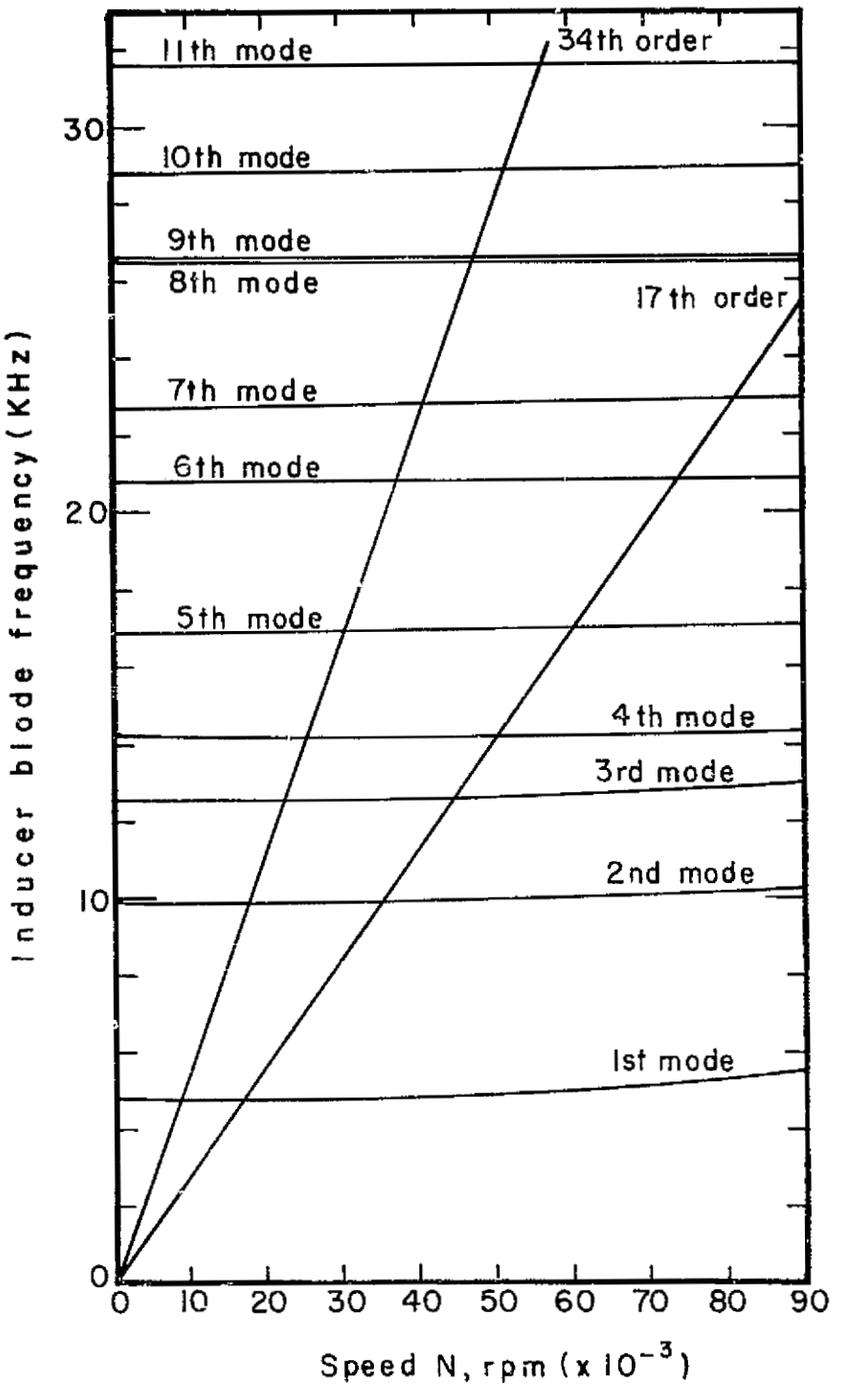

Figure 46—Impeller Campbell Diagram

The Boeing Program WASP calculates disc stress, radial deflections, and axial deflections of the impeller. The principal results are listed in Table XV. Stresses and deflections scale as the square of the speed. Thus the peak centrifugal disc bore stress is 5.26×10^8 Newton/m^2 at air design speed (75,000 RPM) and 2.56×10^8 Newton/m^2 at LSM design speed (52,300 RPM). Impeller tip deflections at impeller design speed are 8.64×10^{-5} m rearward and 1.397×10^{-4} m radially. Blade stiffening of the disc, which may be significant in reducing axial deflections, is not handled by the Boeing WASP analysis.

The maximum speed for long term operation with elastic (no creep) behavior is 80,000 RPM (107.7% air design speed, 153% LSM design speed). A number of cautionary points must be noted with respect to disc stress and deflection. Bore diametric growth from centrifugal effects is 1.016×10^{-4} m at design speed in air (75,000 RPM) and 1.524×10^{-4} m at 120% air design speed. Therefore, considerable care must be taken in mounting this impeller on its shaft if this design is to be spun in air at 75,000 RPM and over. Also, as implied by the 7.58×10^8 Newton/m peak bore stress at 90,000 RPM, the bore will yield locally and stress relieve at 90,000 RPM (120% air design speed). A residual compressive stress will then remain in the bore at rest. 120% air design speed operation should certainly be initially attempted only in a suitable spin pit facility with the bore to shaft fit suitably remade after spin. If significant long term service is contemplated for this wheel beyond the Creare experimental work, then low cycle fatigue analyses should also be performed.

Critical speed analysis - The high speed rotating component assembly is shown in Figure 47. The critical speed analysis of this "overhung" assembly showed that the shaft first bending mode critical speed occurs at approximately 12,000 RPM. Two more critical speeds occur at 29,500 RPM and 30,700 RPM and these are the bearing bounce and rock modes, respectively. A critical also occurs at 33,500 RPM and is a system critical and not the shaft second bending mode. No other criticals were encountered up to 90,000 RPM.

The first predicted critical occurs just below the speed where the first critical has been experimentally observed using a compressor rotating assembly with about

TABLE XV - MAXIMUM DISC STRESS AND RADIAL AND AXIAL TIP DEFLECTIONS

	90,000 RPM (120% $N_{D\ air}$)	75,000 RPM ($N_{D\ air}$)	52,000 RPM ($N_{D\ LSM}$)
Maximum Disc Stress ($\frac{Newton}{m^2} \times 10^{-8}$)	7.580	5.270	2.530
Radial Impeller Tip Deflection (mm)	0.203	0.142	0.069
Axial Impeller Tip Deflection (Rearward - (mm))	0.122	0.084	0.041

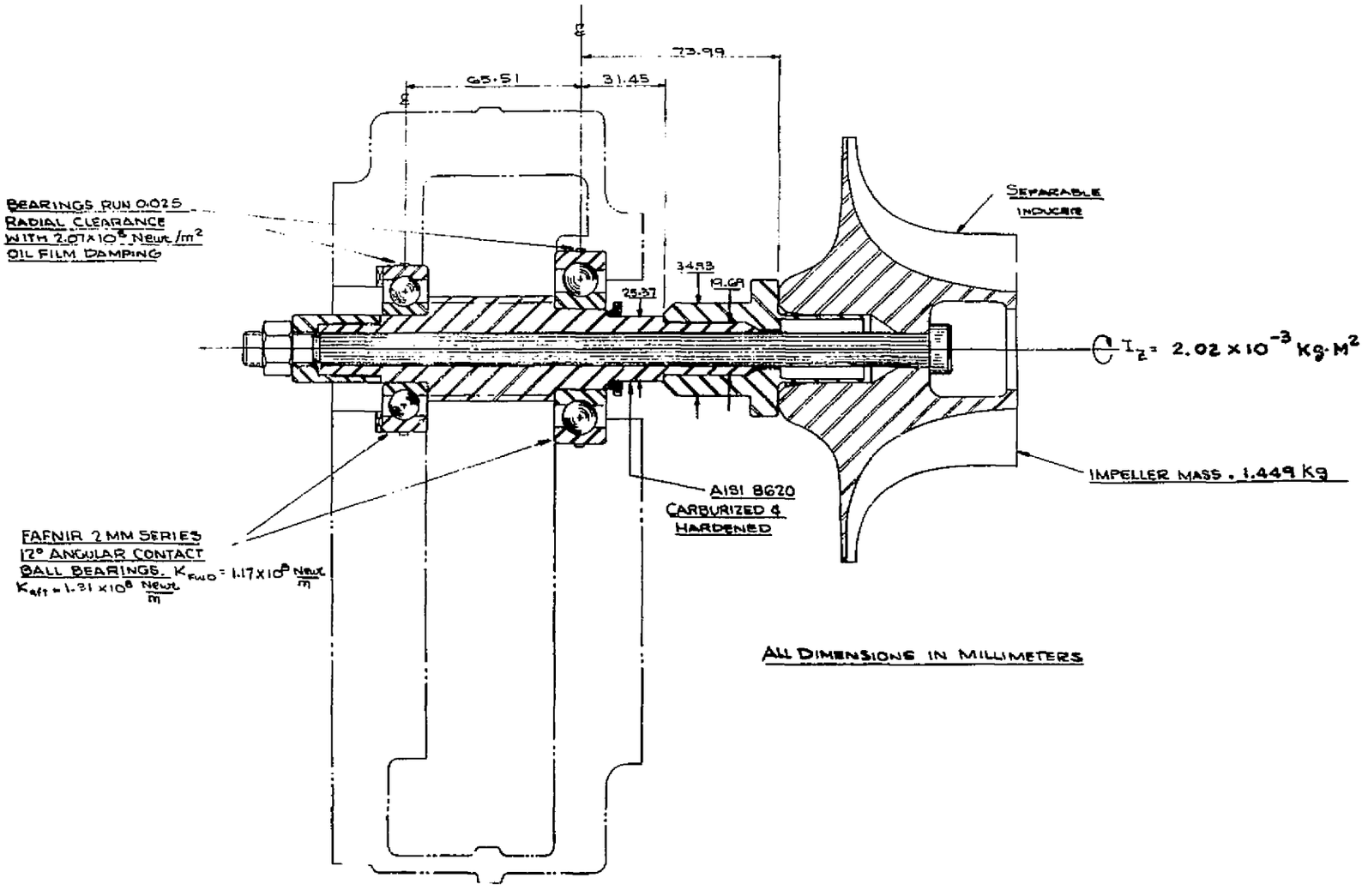

Figure 47 - High Speed Impeller Assembly

the same rotating parameters as this present design. The "swell" in vibration levels predicted between 29,500 and 33,500 RPM have also been observed in past tests.

The first critical represents no problem as the rig is run quickly through this critical speed at start-up and shut-down. The "swells" at 29,500 to 33,500 RPM also pose no problems since past experience has shown that these are relatively low amplitude, rotational vibrations and the rig can be run through these speeds (and even held at these speeds for some time) without appreciable impeller deflection.

Inlet Hardware

The inlet hardware is of standard design which has been used on previous testing of compressor hardware of similar pressure ratio and flow rate on the LSM rig. Since the inlet hardware is not subjected to severe thermal gradients during test, the only substantial causes of deflections and stresses in the inlet hardware are pressure differntials between the impeller, plenum and ambient. In the inlet region, the magnitude of forces from these pressure differentials are small and the design has proceeded by making the inlet hardware axisymmetric and sufficiently robust (thick sections of aluminum) to withstand these small forces with very small deflection.

Impeller Cover

The primary cause of impeller cover deflections are pressure loadings resulting from pressure differentials between inside and ambient pressures. The calculation of the loading caused by aerodynamic forces during rig operation at design conditions shows that the cover may be expected to deflect (move) axially forward less than 2.54×10^{-5} m. During LSM rig evacuation, the axial deflection will be less than 1.016×10^{-5} m. These deflections are inconsequential to the maintenance of compressor unit critical tolerances during rig operation. Stress levels created by these aerodynamic loadings are very small. The cover hardware is made from aluminum.

Diffuser Components

The diffuser assembly is a "sandwich" design wherein the diffuser vanes are clamped in place and mechanically

sealed between the diffuser front and back covers. The diffuser vane and diffuser front and back clamping (mating) surfaces are ground and polished to provide the proper clamping force load distribution over the vane surfaces and to provide mechanical sealing between vane suction and pressure sides. The diffuser clamping bolts pass through clearance holes provided in the diffuser vanes. The diffuser vanes are positioned in their proper locations using aligning pins. Stress levels imposed upon the diffuser components are extremely small. This includes stresses created by pressure differentials and differences in the thermal expansion coefficients of materials used in the diffuser. All diffuser components are made from aluminum except the diffuser vanes (also bolts and aligning pins) which are steel.

The front diffuser plate has a cut-out section at the impeller exit radius for the LDV viewing window. The LDV window is made from quartz, ground and polished to provide a high quality optical surface for the LDV optical studies. This window spans several diffuser vane tips and mechanically supports and aerodynamically seals across the diffuser vanes. Analyses and experimental bench tests have been made of this window configuration to ensure that any problems associated with thermal mechanical stresses, differential thermal expansion and resultant leakage between window quartz and diffuser cover metal, and mechanical clamping of the diffuser vanes with the quartz window can be successfully handled in compressor test operation. Check-out testing of the compressor hardware under design speed conditions on a companion program has demonstrated the efficacy of this window design.

HARDWARE FABRICATION AND INSPECTION

All of the compressor hardware was subcontracted to and manufactured by outside vendors.

Impeller

Two impellers were manufactured by pantograph machining techniques. Inspection of the impeller hardware compared to Creare supplied specifications was conducted by the vendor. A check inspection of some of the critical impeller dimensions (impeller inducer radius, impeller exit radius, blade thickness, etc.) was carried out by Creare. Figure 48 shows the finished impeller.

Impeller Cover

The impeller cover was manufactured to the specified inside meridional contour and inspected by the vendor. Overall dimensional specifications were checked by Creare. Figure 49 shows the finished impeller cover. The two photographs display (i) the LDV inducer window port and (ii) the cover static pressure tap locations and unsteady, dynamic pressure transducer location holes.

Diffuser

Figure 50 shows the diffuser front and rear cover plates; each is shown with several of the diffuser vanes in place. The aluminum covers were machined with standard machining techniques and inspected by Creare. The diffuser vanes (17 to a set) were machined using tape controlled techniques to ensure accurate replication of the vane dimensions, particularly the vane suction surface. The vanes were inspected by Creare. Visible on the front cover photograph is the LDV window opening. In the vaneless/semi-vaneless region of the cover are the static pressure taps and the several dynamic pressure transducer locations. Figure 51 shows a close-up photograph of a portion of the static pressure tap field in the vicinity of the vane lead edge.

Dynamic Balance of Impeller Assembly

The rotating impeller assembly (impeller, pre-stress hub, impeller shaft and bearings and tie bolt and locknut) was dynamically balanced. Final balance of this assembly was achieved to less than 1.037×10^{-6} kg/m.

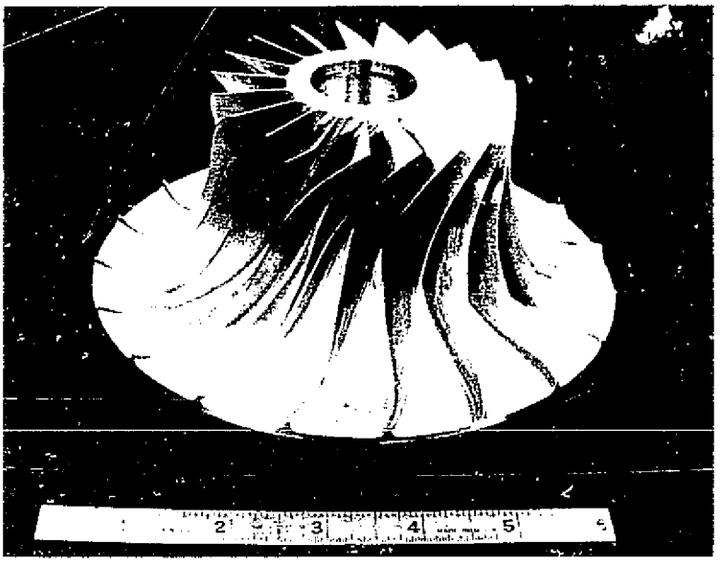

Figure 48 - Compressor Impeller

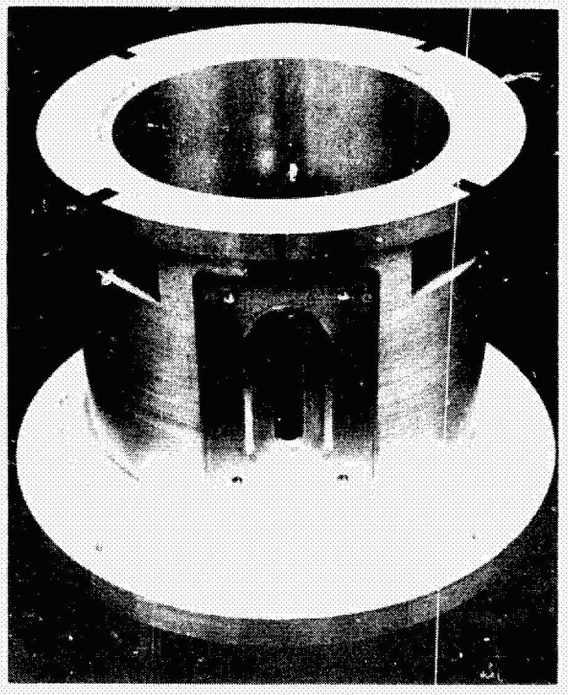

(a)

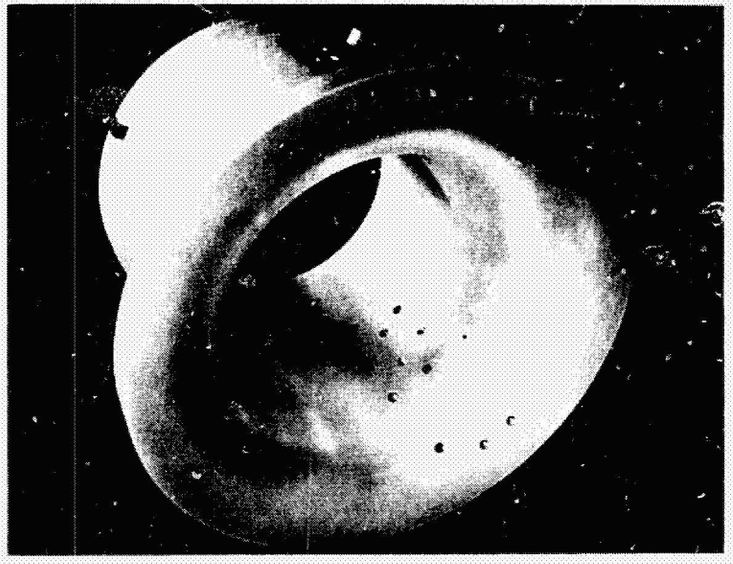

(b)

Figure 49 - Impeller Cover

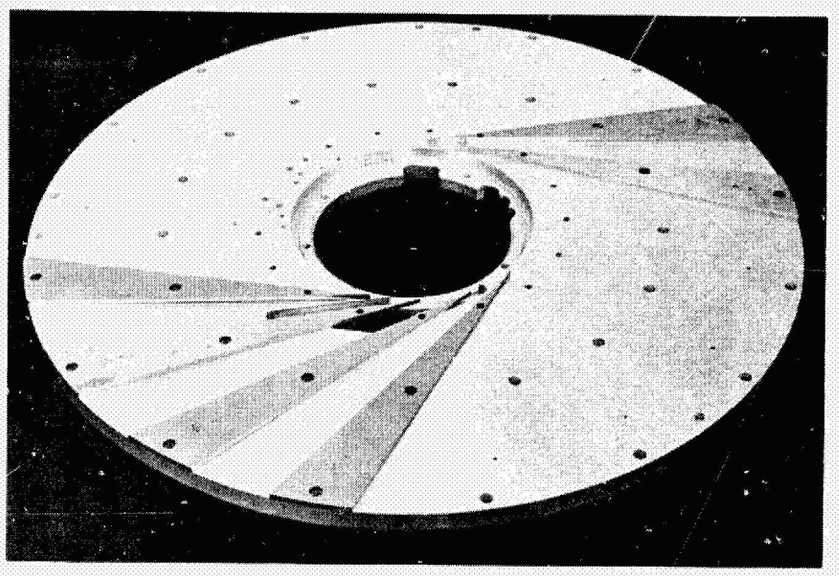

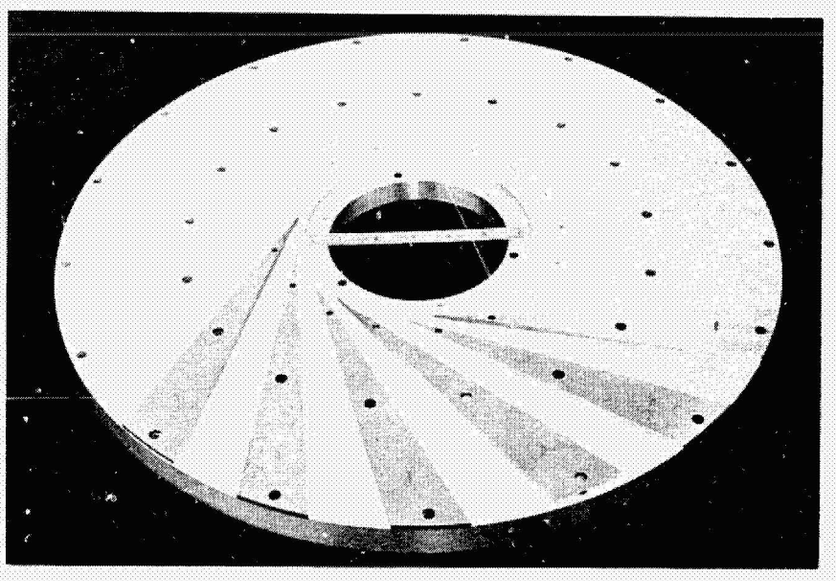

(b)

Figure 50 - Diffuser Assembly

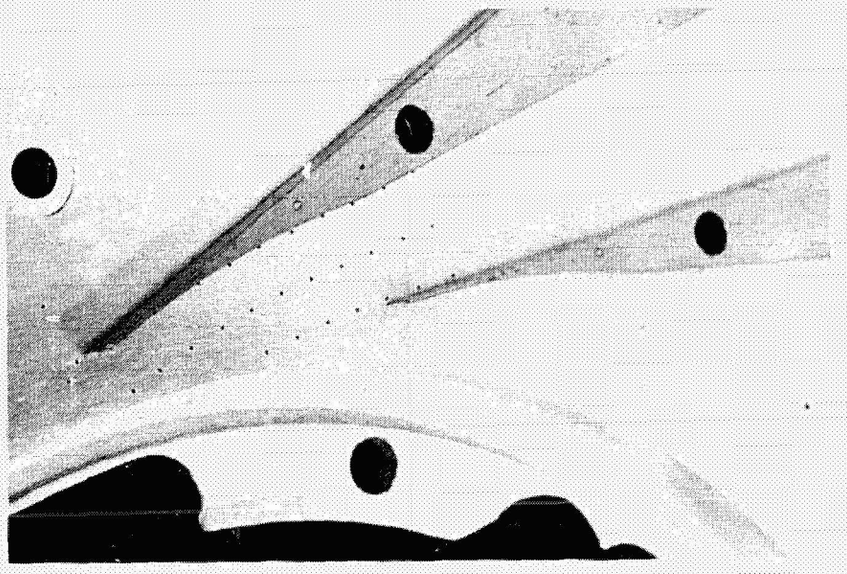

ORIGINAL PAGE IS
OF POOR QUALITY

Figure 51 - Diffuser Vaneless/Semi-Vaneless Region Pressure Taps

Figure 52 shows the assembled compressor hardware prior to installation into the LSM test loop.

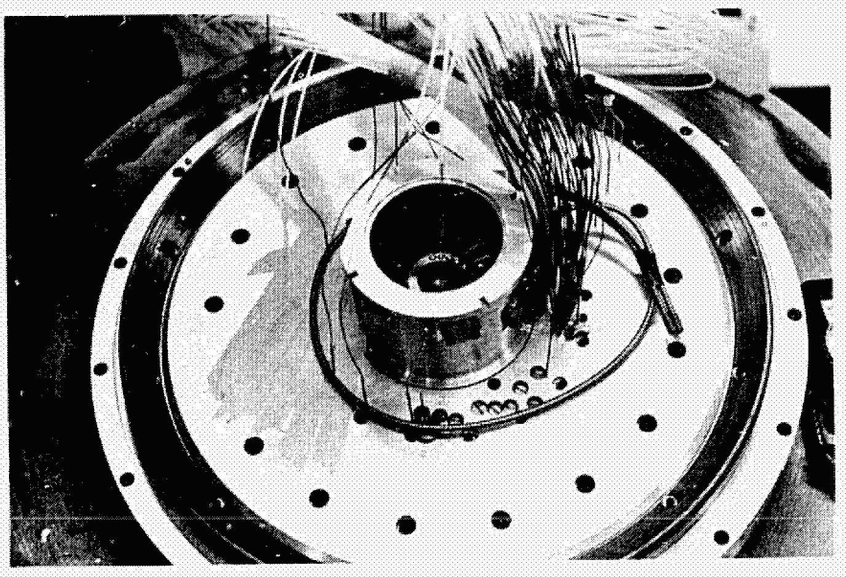

Figure 52 - Assembled Compressor Hardware

CONCLUSIONS

A "state-of-the-art", high pressure ratio (pr = 8), small mass flow (0.907 kg/s), centrifugal compressor stage has been designed, fabricated and mechanically checked out. This stage has been specifically configured to serve as a workhorse compressor for laser Doppler velocimeter (LDV) studies of flow in the impeller inducer and diffuser (and eventually in the impeller). The requirement of making LDV measurements in the compressor impacted the design in two ways: (1) it was desirable to maintain a constant inducer tip radius and (2) it was desirable to have a large blade spacing at exit in order to minimize the time to acquire data with the LDV and yet still sample particle velocities over a small percentage of the blade-to-blade spacing. The impeller has no splitters and thus a higher blade loading within the radial portion of the impeller than would otherwise be desired. An axial inducer configuration with constant inducer tip radius is used. The high blade loading analyzed for the impeller may result in a lower than predicted efficiency although this is not anticipated.

The predicted efficiency, total-to-static, at the design point is 77%. A 12% choke-to-surge flow range is anticipated. The material and stress analyses show adequate strength characteristics for all components of the stage up to 120% of design speed in air (90,000 RPM). The impeller hub bore stresses are expected to exceed the the material yield stress causing local yielding of the bore material at 120% design speed. Appropriate spin testing of the impeller is therefore called for at this speed if the impeller is eventually operated in air. The present use of the impeller is under low speed modeling (LSM) conditions where design speed will be approximately 52,500 RPM.

A mechanical checkout of the entire stage up to 52,500 RPM in the LSM test loop has verified the mechanical critical speed analysis of the high speed, rotating impeller/shaft/bearing assembly. Checkout at design speed has also verified the efficacy of the LDV inducer and diffuser window mechanical designs. No problems have been encountered with sealing or thermal or mechanical stresses.

The compressor hardware, including spare cover, impeller and diffuser hardware is presently available for the conduct of basic centrifugal compressor research studied of the rotating impeller inducer and impeller exit/diffuser entry aerodynamics using LDV technology developed under a companion program.

APPENDIX A

CREARE CENTRIFUGAL COMPRESSOR MODEL NOMENCLATURE AND CREDAS INPUT/OUTPUT NOMENCLATURE

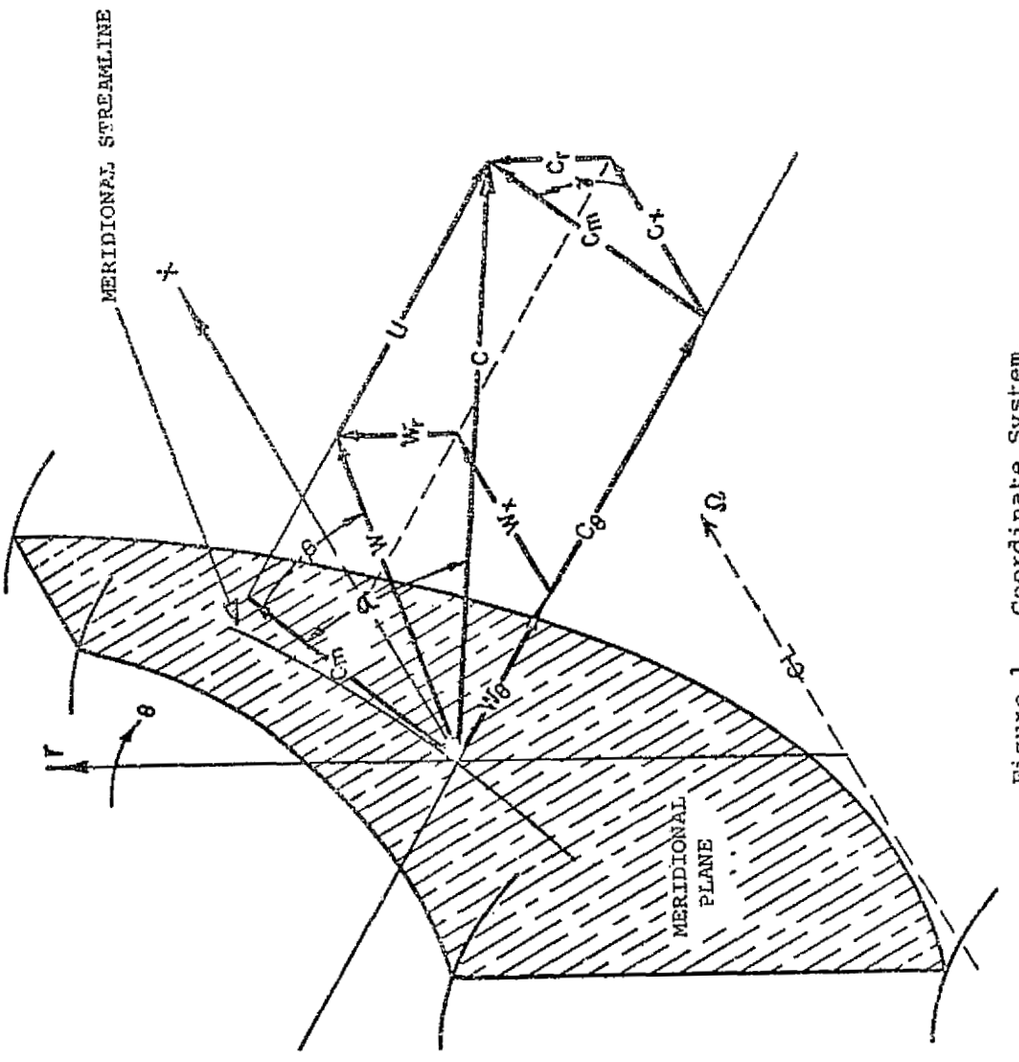

Figure 1. Coordinate System.

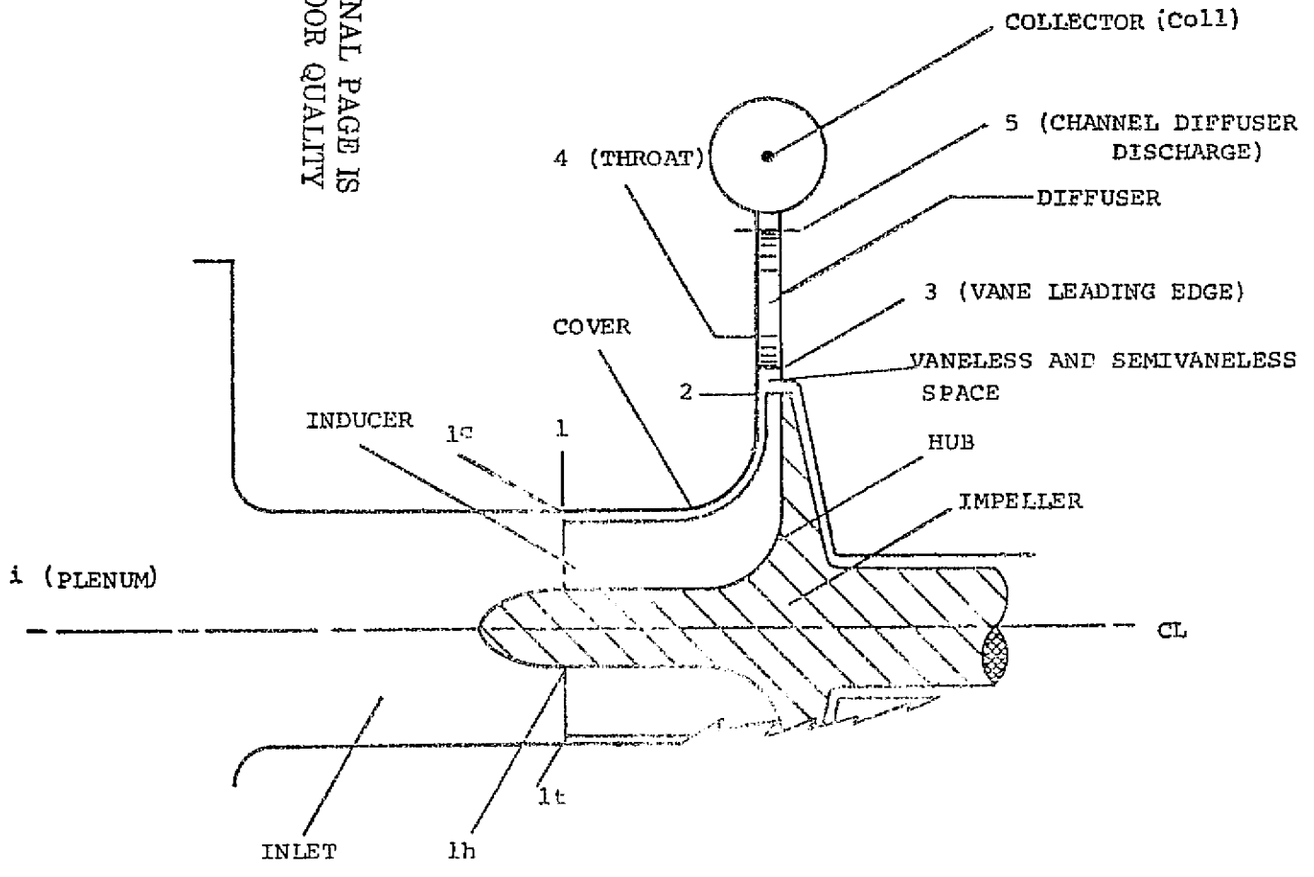

Figure 2. Station Convention and Stage Terminology.

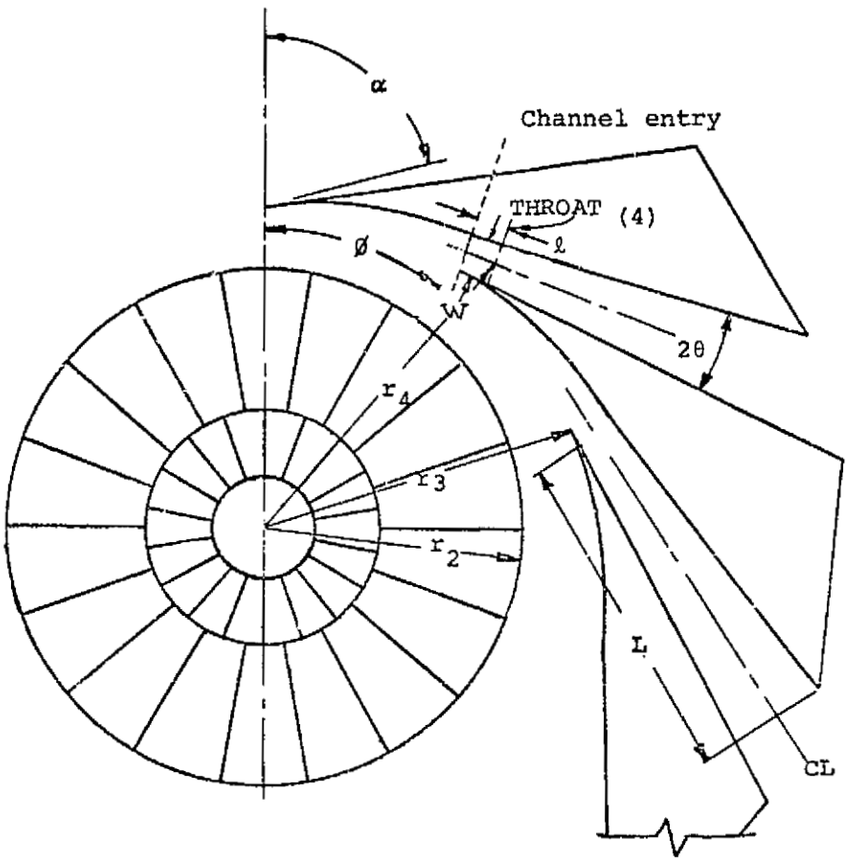

WHERE α = DIFFUSER ANGLE - FROM RADIAL TO "CENTER LINE" DIRECTION

$\emptyset$ = DIFFUSER VANE SPACING (ANGULAR)

2θ = CHANNEL DIVERGENCE ANGLE

W = THROAT WIDTH

L = DIFFUSER LENGTH (OF BOUNDED REGION)

r_2 = IMPELLER TIP RADIUS

r_3 = DIFFUSER VANE LEADING EDGE RADIUS

r_4 = DIFFUSER THROAT RADIUS

ℓ = LENGTH OF CONSTANT AREA SECTION AHEAD OF THE THROAT

Figure 3. Vane-Island Diffuser Geometry.

NOMENCLATURE

A	flow area (normal to mean velocity vector, specifically defined)
A_{eff}	effective area = "one dimensional" cross-sectional flow area
A_{geom}	geometrical cross-sectional area
AR_i	impeller passage geometrical area ratio (inlet to outlet)
AR_{equiv}	equivalent impeller one dimensional flow area ratio
AS_4	channel diffuser throat aspect ratio (b/W for radial-plane divergence; W/b for meridional-plane divergence)
a	acceleration
a	speed of sound
B	boundary layer blockage: $$B \equiv 1 - \frac{A_{effective}}{A_{geometrical}}$$
b	meridional depth of passage (normal to mean meridional velocity component)
BF	blockage factor: $$BF \equiv \frac{A_{effective}}{A_{geometrical}}$$
C	absolute velocity (relative to a Newtonian frame, e.g. compressor casing)
c_f	wall friction coefficient: $$c_f \equiv \frac{\tau}{\rho W^2/2g_o}$$ where: W is measured relative to subject wall

C_p pressure recovery coefficient:

$$C_p = \frac{p - p_{ref}}{(p_o - p)_{ref}}$$

where:
measuring and reference states and stations must be specifically defined.

c_p specific heat at constant pressure

C_T torque coefficient, friction

DR diffusion ratio:

$$DR = (W_1/W_{sep})_t$$

E energy

E_L impeller effectiveness: MR_2/MR_{2i}

F force

g_o proportionality constant in Newton's Second Law

$$F = Ma/g_o$$

H boundary layer shape factor = δ^*/θ

H_i boundary layer shape factor for incompressible flow before transformation to compressible flow

h static enthalpy/unit mass

h_o stagnation enthalpy/unit mass

h_T total enthalpy/unit mass (in a coordinate system rotating in Newtonian space in absence of electricity, magnetism, gravity and capillarity):

$$h_T \equiv h + \frac{W^2 - u^2}{2g_o J}$$

i incidence angle of flow onto blades:

$$(i = \beta_b - \beta)$$

J constant = 1: (778 ft-lb_f/Btu)

k ratio of specific heats

L diffuser centerline length (from throat to exit plane)

LP impeller load parameter:

$$LP = r_2\Omega/W_2Z_i$$

ℓ length of channel diffuser throat, see Figure 3

M Mach number

M mass

m distance along specified meridional trajectory (often streamline of potential solution)

$\dot{m}$ mass flow rate

MR_2 Mach number ratio = $M_{rel\ lt}/M_{rel\ 2j}$

MR_{2i} = $M_{rel\ lt}/M_{rel\ 2i}$

$M_{rel\ 2i}$ = ideal impeller discharge relative Mach number for a given impeller geometry, $\dot{m}$ and N and for isentropic internal flow; discharge blockage B_2 = only blade metal blockage, uniform discharge state and $\beta_2 = \beta_{b2}$ mean line

N shaft speed

N_s specific speed:

$$N_s = \frac{N\sqrt{Q_o}}{(\Delta h_o)^{3/4}}$$

where:

N = Radians/sec: (rpm)

Q_o = inlet flow = $\dot{m}\rho_{oo}$ in m^3/sec: (ft^3/sec)

Δh_o = ideal stage enthalpy rise in Joules/Kg: ($ft\text{-}lb_f/lb_m$)

p static pressure

p_o stagnation pressure

pr pressure ratio

$$pr = p/p_{oo}$$

p_T total pressure; a rotating coordinate property defined by (for perfect gas):

$$\frac{p_T}{p_{oo}} = \left(\frac{T_T}{T_{oo}}\right)^{\frac{k}{k-1}}$$

q dynamic pressure:

$$q = \frac{1}{2g_o} \rho C^2$$

Q heat

R radius ratio, r/r_2

R gas constant

°C,°K degrees

r radius

r radial coordinate (see Figure 1)

S distance between impeller blades:

$$S = 2\pi r/Z$$

S distance along streamline

SP stability parameter: $SP = (\partial pr/\partial m)/pr$

s entropy/unit mass

T static temperature

T_o stagnation temperature

T_T total temperature (defined by h_T and c_p for a perfect gas)

t blade thickness (in direction specified)

t_b blade (metal) thickness

u impeller (metal) velocity

W diffuser throat width (in radial plane)

W relative velocity (in coordinate system rotating steadily in Newtonian space)

W_x total shaft work per unit mass of fluid

W_{xi} work input to impeller per unit mass of fluid

V_s slip velocity:

$$V_s = C_{m2} \tan \beta_{b2} - W_{\theta 2}$$

x axial coordinate (see Figure 1)

Z number of blades

α absolute flow angle (see Figure 1)

β relative flow angle (see Figure 1)

γ pitch angle in meridional plane (see Figure 1)

δ^* boundary layer displacement thickness

ε wake width

ε effectiveness (for impeller $\varepsilon_i = MR/MR_i$)

η efficiency:

$$\eta = \frac{h_{os} - h_{oo}}{W_x}$$

(measuring stations must be specifically defined)

θ boundary layer momentum thickness

θ tangential angular coordinate (see Figure 1)

2θ diffuser divergence angle

λ swirl parameter:

$$\lambda \equiv C_\theta / C_r$$

μ_i work input coefficient:

$$\mu_i \equiv \frac{W_x}{u^2/g_o}$$

ξ_{WL} Welliver Loss Coefficient=$(P_{o2*}-P_{o4})/(P_{o2*}-P_{2*})$

ξ vorticity or loss coefficient:

$$\xi_{IGV} = \frac{\Delta p_o}{(p_o - p)_1}$$

πMi impeller-tip Mach number:

$$\pi Mi \equiv u_2/a_{oo}$$

ρ density

ρ_o stagnation density

σ slip factor:

$$\sigma = 1 - V_s/u_2$$

τ fluid shear stress

τ torque

ψ yaw angle (between velocity vector and null direction of flow angle measuring probe)

Ω impeller angular velocity

Subscripts

0,1,2,3, --	stations in the stage (see Figure 2)
b	blade property
bf	back flow
CL	centerline
c	cover
coll	collector station (receiving volume after diffuser)
crit	critical value (must be specifically defined)
D	diffuser
dm	(impeller) discharge mixing
eff	effective
f	friction
geom	geometrical
h	hub
i	inlet or impeller

i	ideal
IW	internal wake (loss)
IGV	inlet guide vane property
j	jet
le	leading edge
m	mean
o	stagnation
n	normal thickness
p	pressure surface of blade
p	polytropic
r	radial component (see Figure 1)
rd	rear disc (friction)
ref	reference state or station (must be specifically defined)
rel	relative to impeller coordinates
s	indicates that process follows an isentropic path
s	suction surface
sep	flow separation value
surf	surface property
T	total (see definitions of h_T, T_T, and p_T)
t	tip or throat
TS	total to static (efficiency)
TT	total to total (efficiency)
WL	Welliver loss
w	wake

x	upstream of shock (e.g. M_x) or axial component (see Figure 1)
y	downstream of shock (e.g. M_y)
θ	tangential component (see Figure 1)

Superscripts

*	mixed out state (must be specifically defined)
**	impeller discharge state including all work input from fluid angular momentum, cover and rear disc friction and back flow
'	time-varying property
^	instrument-indicated property
∿	mass-flow-averaged property
-	time-averaged property
=	area-averaged property
→	vector quantity

Miscellaneous

ln	natural logarithm
log	base 10 logarithm
exp	exp a ≡ e^a
e	base of the natural logarithms (e = 2.71828...)
f()	function of ( )
$\tan^{-1}()$	inverse operator: $\alpha = \tan^{-1}\lambda$ mean $\tan\alpha = \lambda$
Δ	incremental (but finite) change
d	incremental (but infinitesimal) change, total derivative
∂	incremental (but infinitesimal) change, partial derivative
π	3.1416..

REFERENCES

1. Dean, R. C., Jr.; THE FLUID DYNAMIC DESIGN OF ADVANCED CENTRIFUGAL COMPRESSORS; Creare Technical Note, TN-185, 1974.

2. Monsarrat, N. T., Keenan, M. J. and Tramm, P. C.; HIGH-LOADING, LOW-SPEED FAN STUDY, VOLUME 1, DESIGN; NASA CR-72536, July 1969.

3. Harley, K. G. and Burdsall, E. A.; HIGH-LOADING, LOW-SPEED FAN STUDY II: DATA AND PERFORMANCE UNSLOTTED BLADES AND VANES; NTIS N70-27228, NASA CR-72567, 1971.

4. Harley, K. G., Odegard, P. A. and Burdsall, E. A.; HIGH-LOADING, LOW-SPEED FAN STUDY IV: DATA AND PERFORMANCE WITH REDESIGN STATOR AND INCLUDING A ROTOR TIP CASING TREATMENT; NASA CR-120866, 1972.

5. Eckardt, D.; INSTANTANEOUS MEASUREMENTS IN THE JET-WAKE DISCHARGE FLOW OF A CENTRIFUGAL COMPRESSOR IMPELLER; ASME Paper No. 74-GT-90, May 1972.

6. Runstadler, P. W., Jr.; PRESSURE RECOVERY PERFORMANCE OF STRAIGHT-CHANNEL, SINGLE-PLANE DIVERGENCE DIFFUSERS AT HIGH MACH NUMBERS; USAAVLABS Technical Report 69-56, October 1969.

7. Runstadler, P. W., Jr. and Dolan, F. X.; FURTHER DATA ON THE PRESSURE RECOVERY PERFORMANCE OF STRAIGHT-CHANNEL, PLANE-DIVERGENCE DIFFUSERS AT HIGH SUBSONIC MACH NUMBERS; ASME Paper No. 73-FE-5, 1973.

8. Vanco, M.; FORTRAN PROGRAM FOR CALCULATING VELOCITIES IN THE MERIDIONAL PLANE OF A TURBOMACHINE; NASA TN D-6701, March 1972.

9. Katsanis, T.; USE OF ARBITRARY QUASI-ORTHOGONAL FOR CALCULATING FLOW DISTRIBUTION IN THE MERIDIONAL PLANE OF A TURBOMACHINE; NASA TN D-2546, December 1964.

10. Stanitz, J. D. and Prian, V. D.; A RAPID APPROXIMATE METHOD FOR DETERMINING VELOCITY ON IMPELLER BLADES OF CENTRIFUGAL COMPRESSORS; NACA TN-2421, 1951.

11. Englert, G.; ESTIMATION OF COMPRESSIBLE BOUNDARY LAYER GROWTH OVER INSULATED SURFACES WITH PRESSURE GRADIENT; NACA TN-4022, June 1957.

REFERENCES - Continued

12. Runstadler, P. W., Jr. and Dolan, F. X.; DESIGN, DEVELOPMENT, AND TEST OF A LASER VELOCIMETER FOR HIGH SPEED TURBOMACHINERY; NASA CR 134781, in publication.

13. Rothe, P. H. and Johnston, J. P.; THE EFFECTS OF SYSTEM ROTATION ON SEPARATION REATTACHMENT AND PERFORMANCE IN TWO-DIMENSIONAL DIFFUSERS; Report PD-17, Mechanical Engineering Dept., Stanford University, May 1975

14. Abbott, D. E. and Kline, S. J.; THEORETICAL AND EXPERIMENTAL INVESTIGATION OF FLOW OVER SINGLE-DOUBLE BACKWARD FACING STEPS; Report MD-5 Dept. of Mechanical Engineering, Stanford University, June 1961.

15. Speaker, W. V. and Ailman, C. M.; STATIC AND FLUCTUATING PRESSURES IN REGIONS OF SEPARATED FLOW; AIAA Bulletin, Vol. 3, No. 5., p. 121, May 1966.